Coherent femtosecond pulse shaping towards the short wavelength regime

Dissertation
zur Erlangung des Doktorgrades an der Fakultät für
Mathematik, Informatik und Naturwissenschaften
Fachbereich Physik
der Universität Hamburg

Vorgelegt von
Samuel David Hartwell
aus
Wimborne Minster, England

Hamburg
2021

Universität Hamburg
DER FORSCHUNG | DER LEHRE | DER BILDUNG

Gutachter der Dissertation:	Priv.-Doz. Dr. Tim Laarmann Prof. Dr. Markus Drescher
Zusammensetzung der Prüfungskommission:	Prof. Dr. Daniela Pfannkuche Priv.-Doz. Dr. Tim Laarmann Prof. Dr. Markus Drescher Prof. Dr. Ulrike Frühling Prof. Dr. Franz X. Kärtner
Vorsitzender der Prüfungskommission:	Prof. Dr. Daniela Pfannkuche
Datum der Disputation:	22.12.2021
Vorsitzender des Fach-Promotionsausschusses PHYSIK:	Prof. Dr. Wolfgang Hansen
Leiter des Fachbereichs PHYSIK:	Prof. Dr. Günter HW Sigl
Dekan der Fakultät MIN:	Prof. Dr. Heinrich Graener

Eidesstattliche Versicherung
Declaration on oath

Hiermit versichere ich an Eides statt, dass ich die vorliegende Dissertationsschrift selbst verfasst und keine anderen als die angegebenen Hilfsmittel und Quellen benutzt habe. Die eingereichte schriftliche Fassung entspricht der auf dem elektronischen Speichermedium. Die Dissertation wurde in der vorgelegten oder einer ähnlichen Form nicht schon einmal in einem früheren Promotionsverfahren angenommen oder als ungenügend beurteilt.

I hereby declare, on oath, that I have written the present dissertation by my own and have not used any resources and aids other than those acknowledged. The written version submitted corresponds to the one stored electronically. The dissertation presented in this form, has not already been accepted in an earlier doctoral procedure or assessed as unsatisfactory.

Hamburg: 01.11.2021

Samuel David Hartwell

Abstract

Since the advent of the first camera, flashes of light have been an integral tool in observing the world around us. Following the creation of the laser, these flashes of light have been getting temporally shorter and shorter, allowing faster and faster phenomena to be observed. Now these pulses can be as short as femtoseconds, or even a few attoseconds. Control over these short pulses also can allow observation and enable control over dynamics in matter.

In the present thesis the complete characterisation of an all-reflective 4f pulse shaper is presented. A periodic spectral amplitude modulation is applied to a femtosecond **D**eep-**U**ltra**V**iolet (DUV) pulse within an open-loop shaping control scheme. The DUV pulse is produced via nonlinear frequency up-conversion from a fundamental infrared pulse. The pulses before and after this device are fully characterised in time, frequency and chirp. Transmission of the device in the DUV is also measured and data is given. Due to the all-reflective nature of the device it is capable of operating with coherent pulses at short wavelengths, such as pulses produced from a seeded free-electron laser via **H**igh-**G**ain **H**armonic **G**eneration (HGHG). The coherent pulses produced this way via seeding use the same DUV laser as is used to operate the pulse shaper and are generated as harmonics of the seed. The diffraction gratings in the shaper are designed such that harmonics of the seed laser follow the beampath of the DUV pulse through the pulse shaper, minimising the need for realignment.

The coherent extreme-ultraviolet pulses produced from the seeded free-electron laser operating in HGHG are characterised in time and frequency by terahertz streaking. Chirp is applied to the ultraviolet seed pulse and the effect upon the output seeded free-electron laser pulse is explored with temporal pulse characterisation methods.

Control over pulse shaping in the DUV and towards soft x-rays is interesting for applications such as coherent control, where dynamical processes in matter are controlled by coherent light fields.

Seit Erfindung der ersten Kamera sind Lichtblitze ein unverzichtbares Werkzeug um die Welt um uns herum zu beobachten. Mit der Entwcklung des Lasers wurden diese Lichtblitze zeitlich immer kürzer, sodass immer schnellere Phänomene beobachtet werden konnten. Inzwischen können diese Pulse Femtosekunden oder sogar einige Attosekunden kurz sein. Solche Pulse ermöglichen die Beobachtung und die Kontrolle von dynamischen Prozessen in Materie.

In der vorliegenden Arbeit wird die komplett Charakterisierung eines reinreflektiven 4f-Pulsformers vorgestellt. Eine periodische spektrale Amplitudenmodulation wird auf einen tief-ultravioletten (Englisch: **D**eep-**U**ltra**V**iolet (DUV)) Femtosekunden-Puls innerhalb eines offenen angewendet und mit einem offenen Regelkreises gesteuert. Der DUV-Puls wird durch nichtlineare Frequenzaufwärtskonvertierung aus einem fundamentalen Infrarotpuls erzeugt. Die Pulse vor und nach diesem Gerät werden vollständig in Zeit, Frequenz und Chirp charakterisiert. Auch die Transmission des Gerätes für Strahlung im DUV-Bereich wird gemessen und die Ergebnisse werden präsentiert. Aufgrund der rein reflektierenden Natur des Geräts kann es mit kohärenten Pulsen bei kurzen Wellenlängen arbeiten, wie beispielsweise Pulse von geseedeten, auf **H**igh-**G**ain **H**armonic **G**eneration (HGHG) basierenden Freie-Elektronen-Lasern. Die so durch Seeding erzeugten kohärenten Pulse verwenden den gleichen DUV-Laser, der auch zum Betrieb des Pulsformers verwendet wird und werden als Oberwellen des Seeds erzeugt. Die Beugungsgitter im Pulsformer sind so ausgelegt, dass Oberwellen des Seed-Lasers dem Strahlengang des DUV-Pulses durch den Pulsformer folgen, wodurch die Notwendigkeit einer Neuausrichtung minimiert wird.

Die kohärenten extrem-ultravioletten Pulse, die von dem geseedeten Freie-Elektronen-Laser erzeugt werden, der in HGHG arbeitet, werden in Zeit und Frequenz durch Terahertz-Streaking charakterisiert. Ein Chirp wird auf den ultravioletten Seed-Puls aufgeprägt und und die Wirkung auf den ausgegebenen geseedeten Freie-Elektronen-Laserpuls wird mit einer zeitlichen Pulscharakterisierung Methode untersucht.

Die Steuerung der Pulsformung im DUV und hin zu weichen Röntgenstrahlen ist interessant für Anwendungen wie die Kohärente Kontrolle, bei der dynamische Prozesse in Materie durch kohärenten Lichtfelden gesteuert werden.

Contents

Abstract v

1 Introduction 1

2 Theoretical Background 5
- 2.1 Defining Pulsed Laser Light . . . 5
- 2.2 Femtosecond Pulse Generation . . . 10
  - 2.2.1 General Considerations . . . 10
  - 2.2.2 Optical Laser Cavity . . . 10
  - 2.2.3 Pulse Rate and Pulse Width . . . 13
  - 2.2.4 Chirped Pulse Amplification . . . 14
- 2.3 XUV Sources . . . 16
  - 2.3.1 Free-electron Laser Physics in a Nutshell . . . 17
  - 2.3.2 Self-amplified Spontaneous Emission Radiation . . . 20
  - 2.3.3 Seeded Free-electron Lasers . . . 21
- 2.4 High-harmonic Generation in a Nutshell . . . 23
- 2.5 Theory of Nonlinear Frequency Conversion . . . 23
  - 2.5.1 Sum-frequency and Difference-frequency Generation 26
  - 2.5.2 Phase Matching . . . 27
  - 2.5.3 Birefringent Crystals . . . 29
  - 2.5.4 Bandwidth Phase Matching . . . 30
- 2.6 A 4-f Pulse Shaper . . . 31
  - 2.6.1 Spatio-temporal Coupling . . . 34
- 2.7 DUV Pulse Characterisation . . . 34
  - 2.7.1 Frequency-resolved Optical Gating Algorithm . . . 37
- 2.8 XUV Pulse Characterisation . . . 38
  - 2.8.1 THz Streaking . . . 39
  - 2.8.2 Light-field Streaking . . . 40
  - 2.8.3 Classical Picture . . . 41
  - 2.8.4 Quantum Mechanical Picture . . . 42
  - 2.8.5 Reconstruction of Linearly Chirped Pulses . . . 43

3 Design **47**
3.1 Overview . . . 47
3.2 Pulse Shaper . . . 47
3.2.1 Gratings and Focusing Optics . . . 49
3.2.2 Lamellar Mirror Mask . . . 52
3.2.3 Spectral Resolution . . . 55
3.2.4 Spatial Diagnostics for Beam Positioning . . . 56
3.3 DUV Source . . . 56
3.3.1 Generation and Properties of 810 nm Pulses . . . 56
3.3.2 Pulse Compression . . . 57
3.3.3 Third-harmonic Generation (THG) at 266 nm . . . 57
3.4 XUV Source . . . 60
3.4.1 Seeded FLASH . . . 60
3.4.2 Seeded FLASH Properties . . . 60
3.4.3 Timing and Synchronisation . . . 62
3.5 Optical Characterisation Methods . . . 62
3.5.1 Cross-correlation FROG . . . 63
3.5.2 GRENOUILLE . . . 66
3.5.3 Alternative Pulse Characterisation Methods . . . 66
3.6 XUV Characterisation - THz Streaking . . . 68

4 Results **71**
4.1 Overview . . . 71
4.2 Characterisation of the 810 nm Fundamental . . . 72
4.3 Third Harmonic Generation . . . 73
4.3.1 DUV Pulse Optimisation . . . 74
4.3.2 Spatial Chirp and Pulse-front Tilt . . . 76
4.4 Transmission Efficiency . . . 78
4.5 DUV Pulse Shaping . . . 79
4.5.1 Periodic Spectral Amplitude Modulation . . . 79
4.5.2 Spectrograms, Spectra and Phases . . . 80
4.5.3 Simulation of a Shaped Double Pulse . . . 85
4.5.4 Open-loop Control . . . 85
4.5.5 Towards Closed-loop Control . . . 88
4.6 XUV Pulse Generation from Seeded FLASH . . . 90
4.7 XUV Pulse Shaping . . . 96
4.7.1 Chirping the Seed Laser Pulses . . . 96
4.7.2 Chirping the Seeded XUV Pulses . . . 97
4.8 Future Plans for X-Seed . . . 99

5 Conclusion and Outlook **101**

Chapter 1

Introduction

Light **A**mplification by **S**timulated **E**mission of **R**adiation, or LASER light, was initially theorised by Einstein in 1905 [1, 2] and first experimentally shown in 1960 by Maiman *et al.* [3]. Emitting initially at 694 nm this new light source produced both highly spatially and temporally coherent light, which enabled previously unattainable experiments and material processing to be considered. Initially termed "a solution looking for a problem" by Maiman it wasn't long before practical and profitable applications began to show themselves. Examples of such being the first display of laser light used in welding by Houldcroft in 1967 [4], used by NASA in 1969 to accurately measure the distance to the moon [5], the first trapping of an atom by laser light in 1970 by Ashkin *et al.* [6] and recently towards modern commercial mass use applications such as laser pointers, media players and self driving cars. Quickly realising the monumental impact and versatility of such a light source to science, industry and communications, researchers and engineers around the globe began to devote themselves to furthering the variety of light emitted from these sources. Results and developments precipitated themselves in decades following the first laser operation. Examples again being the operation of the first mode-locked pulsed laser system in 1963 by Hargrove *et al.* [7], the introduction of optical fibers in 1966 by Kao *et al.* [8] and (of great importance to this project) the first display of a **F**ree-**E**lectron **L**aser (FEL) in 1971 by Madey *et al.* [9]. Some other examples of important developments within laser technology can be found in [10–13].

One particular property of interest in the development of novel laser systems was the temporal pulse length, typically measured as the time between half of the maximum intensity at the fore and aft of the pulse, or the **F**ull **W**idth **H**alf **M**aximum (FWHM). Specifically of interest was reducing this pulse duration. The innovation of mode-locking allowed pulse durations to decrease down from the microsecond (10^{-3} s) timescale to most recently in 2001 the attosecond (10^{-18} s) regime [14]. Here mode-locking is important as mechanical and electrical tech-

niques are unable to produce, let alone able to measure, such temporally short events. Leaving the only feasible method of such short pulse generation to mode-locking. The principle of mode-locking will be discussed in subsection 2.2.1.

Such temporally short pulses would enable the observation of proportionally shorter and shorter temporal events. A popular example being the motion of electrons within an atomic system [15, 16]. This field of short pulses led to a branch of laser science coined "Ultrafast Science".

Despite these advances within the temporal regime, efforts were still made to have even more control over these optical pulses. More specifically control over the spectral phase of the short pulses and the temporal shape. Here the phase refers to the fact that a laser pulse is comprised of a set range of individual discrete frequencies, contained within the bandwidth of the pulse, and each frequency component may "arrive" at some time relative to that of the others within the bandwidth. This difference in temporal arrival time of frequency components is what we call the phase of the pulse. Control over the phase can lead to some interesting experiments, or conceptual experiments, such as coherent control. Coherent control is the process of controlling quantum mechanical time-dependent processes by application of light [17–19]. This research field contains many exciting applications such as quantum information processing, laser cooling, ultracold physics and quantum communications [19–25]. Coherent control also opens the door to experimentation with various nonlinear processes such as four-wave mixing and transient interactions with molecules [26, 27] and biological imaging to name a few [28, 29].

Many optical setups can be used to enable phase control for such experiments, examples being Michelson interferometers [30], grating compressors [31] and chirped mirrors [32]. However each of these units only provides limited control over the output phase of the pulse, and either limited or no control over the frequency spectrum and the resulting pulse duration. A both popular and successful device to control pulse properties was designed by Froehly *et al.* in 1983 [33]. Called a 4-f pulse shaper it allows bespoke control over full pulse properties, giving the ability to tailor pulses to their required usages. The design and basic physics behind such a device are discussed in section 2.6.

4-f pulse shaping has been widely explored in the optical range [34], but remain largely untested in both extremely short and extremely long wavelength regimes due to difficulty either generating suitable pulses or lack of suitable optical materials to perform the shaping. Examples of pulse shaping using an **A**cousto-**O**ptic **M**odulator (AOM) in the wavelength range of 8 - 15 µm have been shown in [35]. This thesis discusses the design and initial testing of a custom 4-f pulse shaper, designed and optimised for use in range of 15 - 266 nm relying solely on reflective optics operating in grazing incidence.

Work towards pulse shaping in the soft X-ray spectral range has faced two

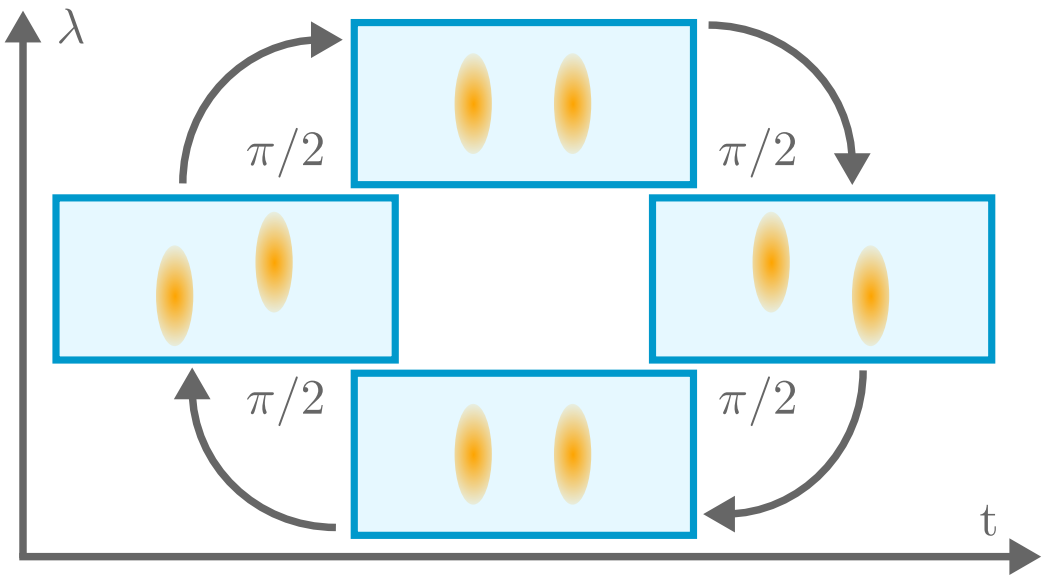

Figure 1.1: Stylised representation of the center-of-mass wavelength oscillations of the pre- and post-pulse as the amplitude modulation mask moves over the spectra for a 2π range in steps of $\pi/2$. The figure represents an open-loop shaping control of the relative spectral phase between the pre- and post-pulse induced by spectral amplitude modulation of the pulse, which is discussed in more detail in section 2.6 and subsection 4.5.4.

primary hurdles; difficulty in use of transmissive optics below 250 nm and difficulty in obtaining sufficiently brilliant spatially (transverse) and temporally (longitudinal) coherent photon sources. The first hurdle is overcome by the use of only reflective optics in the setup, and the second by the advent of seeded FELs [36, 37]. The first FEL was brought into operation in 1971 emitting in the infrared [38]. Further developments extended this range down to the angstrom regime [39]. The development of the **T**esla **T**est **F**acility (TTF) at DESY in Hamburg in 2002 was an important milestone for facilities operating in the **V**acuum **U**ltra**V**iolet (VUV) range [40]. Operating at 100 nm, this device then became the template for future short wavelength FEL designs, such as the European X-FEL and FLASH, both also operating at Hamburg, FERMI at ELETTRA in Trieste and SLAC at Stanford. FELs are able to produce incredibly brilliant laser light, with respect to other short wavelength sources such as **H**igh **H**armonic **G**eneration (HHG) [41], and emit with short pulse durations and broad spectral bandwidths.

The availability of such sources allows detailed study in regions of great interest, especially within organic compounds, many of which have transmissible "windows" in the low wavelength limit. A popular example being that of the so-called water window, a region between the carbon K-edge and the oxygen K-edge to which water is transparent to wavelengths between and 2.23-4.40 nm

[42]. Tailored pulses in this region allow for spectroscopic studies with biological specimens in water, giving insight into real time dynamics of matter in native environment [43].

Within this work, the concepts, motivation and technical requirements to achieve these shaped pulses in the e**X**treme **U**ltra **V**iolet (XUV) range (15 - 40 nm) using the all-reflective 4-f geometry pulse shaping setup are explored [44, 45]. To this end, the operation of this shaper using a **D**eep **U**ltra **V**iolet (DUV) test beam (266 nm) is discussed, with notes on progression to future shorter wavelength operation. Results for spectral amplitude shaped output DUV pulses are presented and the pulses are fully characterised in both time, frequency and phase. The key result of the present thesis is the demonstration and full characterisation of an open-loop shaping control protocol realised at short wavelengths, which is sketched in Figure 1.1. It shows the relative phase control between a temporal pre- and post-pulse by means of selective amplitude modulation. The shaping device is designed such that 266 nm and all its harmonics travel the same beam path through the instrument, allowing multi-colour experiments to be considered in the future.

Chapter 2

Theoretical Background

In the following section the relevant theory behind the work in this thesis will be discussed and briefly delved into. The theory will consist of five contained major sections, each detailing compartmentalised subsections, listed in the order they appear during the experimental work. These sections are

- Definition of ultrashort electromagnetic pulses.
- Viable laser sources and their operation.
- Nonlinear frequency generation.
- 4-f pulse shaping.
- Pulse diagnostics and characterisation.

A general overview of important concepts will be given for each section. For deeper theoretical knowledge, literature is referenced in each section allowing the reader to gain further understanding if desired.

2.1 Defining Pulsed Laser Light

To understand the mechanics behind shaping ultrafast laser pulses, first the mathematical description of a laser pulse needs to be understood. Then how that expression can be transformed, which properties of the pulse are transformed and how this affects the physical representation of the pulse.

A laser pulse is defined entirely by it's electric field $E(t)$ and by its polarisation. $E(t)$ being a product of a time varying envelope $K(t)$ and a periodic function defined as $\cos(\omega_0 t + \phi(t))$. Throughout this work it will be assumed all

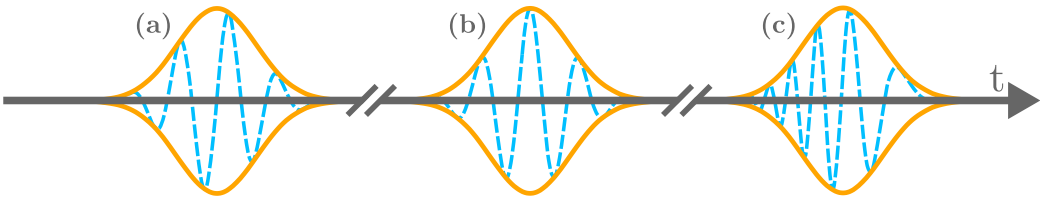

Figure 2.1: Displayed in (a) and (b) is the same time varying envelope, $K(t)$, (orange), with the same carrier wave, $\cos(\omega_0 t + \phi(t))$, displayed underneath (blue). A phase offset of π is present between the carrier waves in (a) and (b). Displayed in (c) is a representation of a chirped pulse, here the colour (or frequency) of the pulse changes as a function of time, in this case the pulse is linearly chirped.

light is linearly polarised, and circular and elliptical polarisations will be ignored. The electric field of a pulse can be mathematically defined as

$$E(t) = K(t)\cos(\omega_0 t + \phi(t)), \tag{2.1}$$

where ω_0 is defined as the carrier frequency (thus carrier wavelength λ_0 being equivalent to ω_0/c), and $\phi(t)$ is defined as the phase offset between the carrier wave and envelope function. These three properties $K(t)$, ω_0/c and $\phi(t)$ contain all the information of the pulse and are visualised in Figure 2.1. From Equation 2.1 and using Euler's formula the electric field can be written as

$$E(t) = \frac{1}{2}K(t)e^{i(\omega_0 t+\phi(t))} + c.c.\,, \tag{2.2}$$

this form is now convenient for further complex analysis and also for use in performing mathematical transformations. As such this form will be used for the remainder of this work. By performing a Fourier transform on the electric field in time, the electric field with respect to angular frequency ω can be retrieved, such that

$$E(\omega) = \int_{-\infty}^{\infty} E(t)e^{i\omega t}dt, \tag{2.3}$$

and naturally inversely such that

$$E(t) = \frac{1}{2\pi}\int_{-\infty}^{\infty} E(\omega)e^{-i\omega t}d\omega, \tag{2.4}$$

which defines $\mathrm{E}(\omega)$ and $\mathrm{E}(t)$ as a Fourier pair. This relation means a laser pulse can be completely defined by its electric field both in the time domain or in the spectral domain. The electric field $E(t)$ can be further broken down into a complex analytical form, with

$$E(t) = \frac{1}{2}(\tilde{E}(t) + \tilde{E}^*(-t)), \tag{2.5}$$

where $\tilde{E}$ is the real part of the electric field and $\tilde{E}^*$ being its complex conjugate. As $E(t)$ is real, it is inferred that $\tilde{E}$ is Hermitian, and thus obeys the relation

$$\tilde{E}(t) = \tilde{E}^*(-t). \tag{2.6}$$

From combining Equations 2.3, 2.4 and 2.6, it can be inferred that

$$\tilde{E}(\omega) = \tilde{E}^*(-\omega). \tag{2.7}$$

It is often practical to define the pulse mathematically such that

$$\tilde{E}(\omega) = A(\omega)e^{i\phi(\omega)}, \tag{2.8}$$

with $A(\omega)$ defined as the spectral amplitude and $\phi(\omega)$ defined as the spectral phase. As the pulse is fully defined by this equation, we can infer that for a particular spectral amplitude, the spectral phase $\phi(\omega)$ will define the shape and duration of the pulse. Physically $\phi(\omega)$ is the spectral phase and its derivative with respect to ω represent the offset between individual frequency components of the pulse. This is defined as the "group delay", T_g, where

$$T_g(\omega) = \frac{d\phi(\omega)}{d\omega}. \tag{2.9}$$

The spectral phase can be expanded using a Taylor expansion, to retrieve multiple terms, each having a specific physical meaning. Performing this expansion

$$\begin{aligned}\phi(\omega) = \phi(\omega)^{(0)}_{\omega_0} + \phi(\omega)^{(1)}_{\omega_0}(\omega-\omega_0)\ldots \\ + \frac{1}{2}\phi(\omega)^{(2)}_{\omega_0}(\omega-\omega_0)^2 + \frac{1}{6}\phi(\omega)^{(3)}_{\omega_0}(\omega-\omega_0)^3\ldots \\ + \frac{1}{24}\phi(\omega)^{(4)}_{\omega_0}(\omega-\omega_0)^4 + \ldots + \frac{1}{n!}\phi(\omega)^{(n)}_{\omega_0}(\omega-\omega_0)^n,\end{aligned} \tag{2.10}$$

where

$$\phi(\omega)^{(n)}_{\omega_0} = \frac{d^n\phi(\omega)_{\omega_0}}{d\omega^n_{\omega_0}}. \tag{2.11}$$

The first four components of this expansion are

- $\phi(\omega)^{(0)}_{\omega_0}$, which is the **C**arrier **E**nvelope **P**hase (CEP). It is the phase difference between the envelope of the electric field and the carrier pulse. This is of particular importance when dealing with few cycle pulses [46, 47]. A representation of how this phase may differ in two pulses with the same CEP can be seen in Figure 2.1(a) and Figure 2.1(b).

- $\phi(\omega)^{(1)}_{\omega_0}$, which is called the group delay, or the temporal delay between the pulse and some point in time.

- $\phi(\omega)^{(2)}_{\omega_0}$, which is the chirp of the pulse. It describes the distribution of the frequencies in the pulse as a function of time within the pulse. Naturally the shortest possible pulse has no chirp, and all the frequency components are distributed equally throughout the pulse. Introducing a chirp will elongate the pulse in time. Introducing a negative chirp to an already positively chirped pulse will shorten the pulse in time[1]. A representation of linear chirp can be seen in Figure 2.1(c).

- $\phi(\omega)^{(3)}_{\omega_0}$, which represents the cubic phase. This can create pre- or post-pulses in the time domain. To create the shortest possible pulses, the cubic phase has to be accounted for as well.

The shortest achievable pulse duration is obtained, when all terms of orders higher than $\phi(\omega)^{(1)}_{\omega_0}$ are zero. This is defined as "flat phase" and pulses with this shortest pulse duration are referred to as "Fourier-limited pulses". The **F**ull **W**idth **H**alf **M**aximum (FWHM) pulse duration of a Fourier-limited pulse Δt, and the FWHM spectral width of the same pulse $\Delta\omega$, have the following relation, called the **T**ime **B**andwidth **P**roduct (TBP).

$$\Delta t \, \Delta\omega = \text{TBP} \tag{2.12}$$

From which it is apparent that a Fourier-limited pulse has a pulse duration inversely proportional to the spectral width of the pulse[2]. Relating the value of Δt to $\Delta\omega$ for a real pulse gives knowledge of how close to the Fourier limit the pulse is, defined by how close the product is to a set minimum value. The minimum TBP depends on the shape of the pulse in frequency and time. Two common

[1] Assuming the negative chirp added does not fully compensate for the positive chirp.

[2] Note this applies only to the minimum possible pulse duration, a longer pulse with a given spectral bandwidth is possible with the presence of non zero values of $\phi(\omega)^{(2)}_{\omega_0}$ or higher. This is defined as a non flat phase. This minimum pulse duration also heavily relies upon the shape of the pulse in time and frequency domain, respectively.

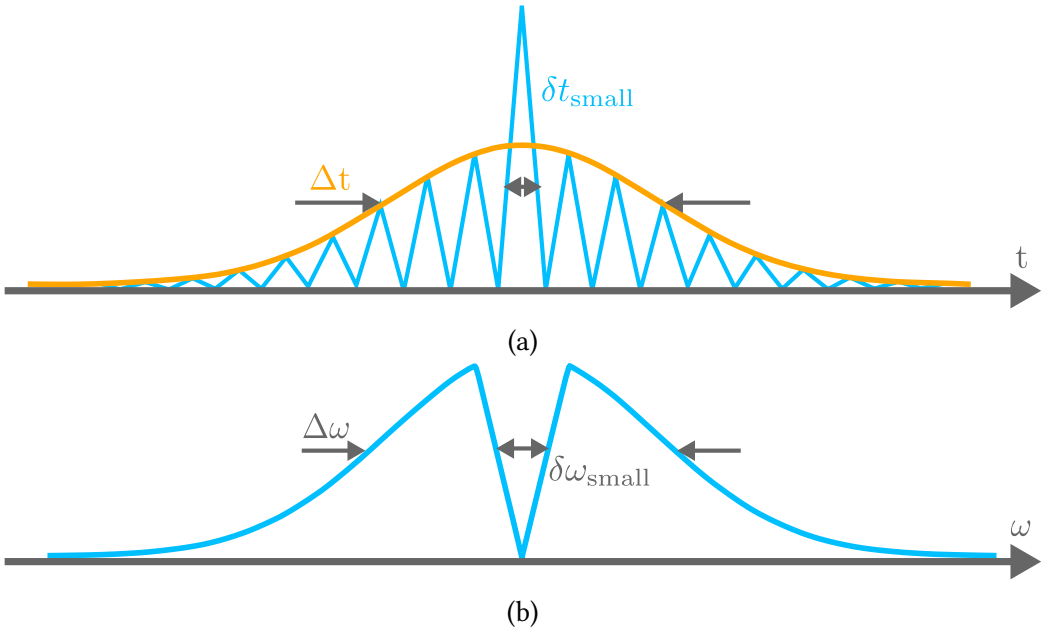

Figure 2.2: Visualisation of smallest (δt_{small}) and largest (Δt) structure size in time (a) for a set pulse. A Gaussian envelope (orange) displays the FWHM pulse duration. The intensity in arbitrary units is shown in blue. In (b) the spectrum is in blue, with the smallest ($\delta\omega_{\text{small}}$) and largest ($\Delta\omega$) structures in frequency also shown. All values are given as FWHM.

pulse shapes generated by ultrafast lasers are Gaussian and Hyperbolic Sechant (Sech), with TBP equalling 0.441 and 0.315, respectively. A diagram of various common pulse shapes can be seen in [48].

For the remainder of the work it will be assumed that all pulses are Gaussian in frequency and time. The TBP is also related to the complexity of the pulse, this being the ratio of the smallest to the largest features in the temporal and spectral domains. A representation of this being seen in Figure 2.2. Defining η as the complexity we find

$$\eta = \frac{\Delta t}{\delta t_{\text{small}}} = \frac{\Delta\omega}{\delta\omega_{\text{small}}}. \tag{2.13}$$

where δt_{small} and $\delta\omega_{\text{small}}$ are the smallest features in the pulses time and frequency domain respectively. For a Gaussian pulse one finds the relationship between TBP and complexity to be

$$\eta \approx \frac{\text{TBP}}{4\ln 2}. \tag{2.14}$$

This relation between complexity and TBP implies that the complexity is another

measure of how close to a Fourier limit the pulse is.

As such from these derivations, it is apparent that a pulse of light can be fully defined by three parameters, the pulse duration Δt, the spectrum $A(\omega)$ and the spectral phase $\phi(\omega)$. Any experimental retrieval of pulse information needs to obtain each of these three values to be able to be said to "fully" characterise the pulse. Details of such methods will be discussed in the design section of the thesis, specifically within section 2.7 and section 2.8. With regards to the duration of the light pulse, it has been shown that the minimum pulse duration limit of a pulse is defined by it's spectral width $\Delta\omega$, and pulse shape in time. The reality of how close a real pulse is to this limit can be mathematically defined by the TBP, or equally by looking at the complexity of the pulse.

2.2 Femtosecond Pulse Generation

2.2.1 General Considerations

The generation of tabletop ultrafast laser pulses typically relies on a technique called "mode-locking". Within this work all lasers used or that are planned to be used rely, at least in part, on this technique. The principle behind mode-locking stems from the concept of destructive and constructive interference in waves, such that at one point in time two or more frequencies will create a "beat", resulting in fluctuations in intensity, larger where the frequencies are in phase (constructive interference) and smaller where they are out of phase (destructive interference). A simple representation of this beating with 2, 5 and 100 frequencies separated by a difference $\delta\omega$, can be seen in Figure 2.3. The more individual frequency components present, the shorter in time this beat becomes. Thus it is apparent that by increasing the number N of individual frequency components, each separated by $\delta\omega$, results in a shorter temporal pulse duration[3]. This is the simplified idea behind mode-locking in laser systems.

2.2.2 Optical Laser Cavity

First the geometry of a standard laser cavity will be considered. A standard laser cavity consists of at least three elements, these being two mirrors, and an enclosed gain medium. Defining a distance L between the two mirrors and defining the speed of light inside the entire cavity as c, then the time for the light to perform one round trip inside the cavity mirror to mirror is

[3] As here with a set frequency difference $\delta\omega$ increasing N would increase the spectral bandwidth.

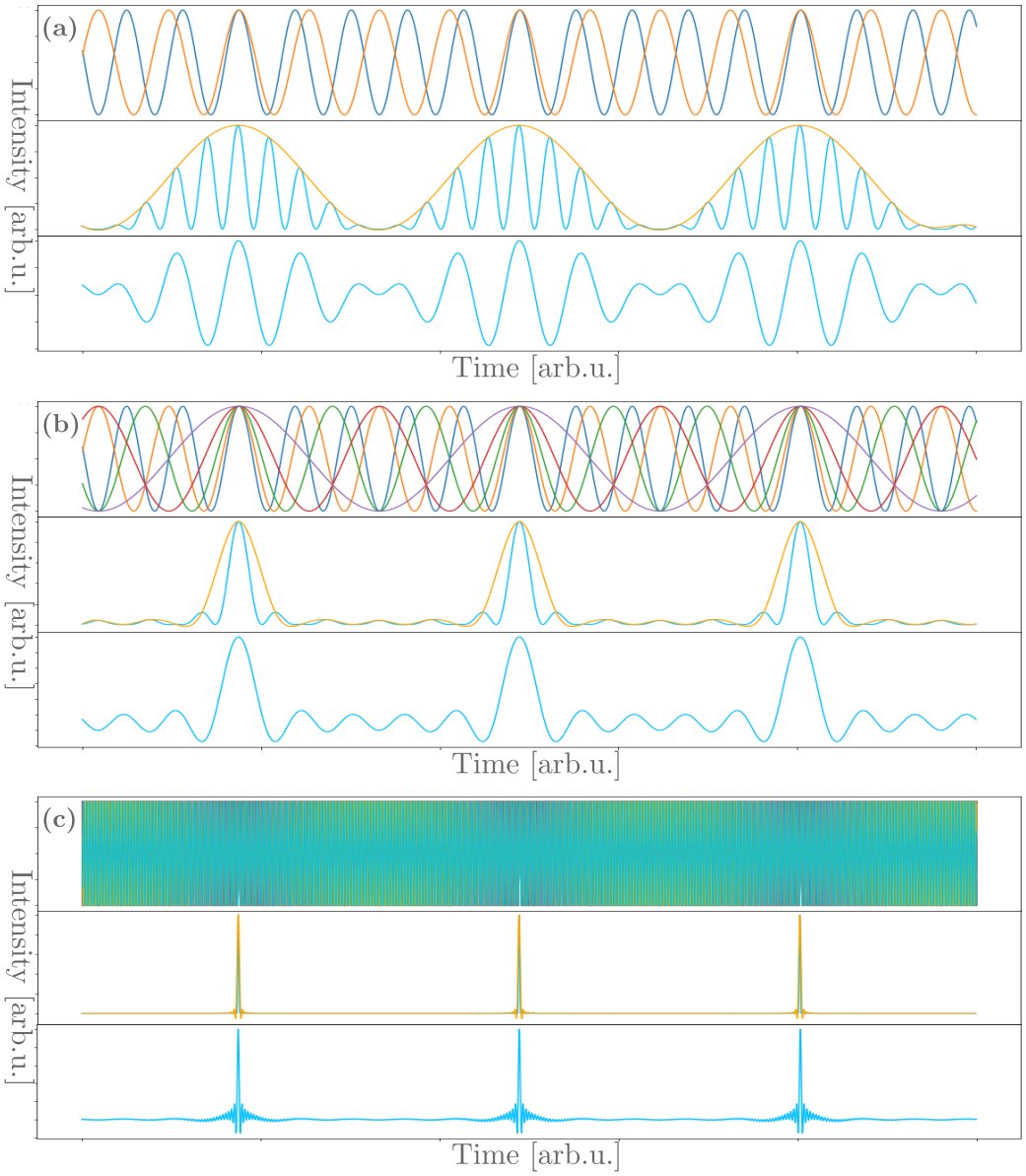

Figure 2.3: Principle of mode-locking. In sub-figure (a), top: two overlapping monochromatic waves with frequencies separated by $\delta\omega$. (a) middle: the intensity (blue) and the envelope (orange) of the waveform resulting from the sum of two waves in the top plot. (a) bottom: the waveform obtained from coherent superposition of the two waves. Sub-figures (b) and (c) follow the same principle but with 5 and 100 overlapping standing wave modes respectively.

$$T_{\text{RT}} = \frac{2L}{c}, \tag{2.15}$$

with each trip through the cavity, twice in one round trip, the beam will gain in energy with passes through the gain medium. Typically one mirror within the cavity is designed such that a set percent of the incidence beam is leaked out with each reflection. This leakage becomes the output beam. Inside this cavity with length L standing waves will appear when the round trip length $2L$ is an integer number of wavelengths. Such that the wavelength of the possible standing waves can be given by

$$\lambda = \frac{2L}{n} \qquad N \in \mathbf{N}. \tag{2.16}$$

These standing waves are called "longitudinal modes", each mode being separated by a frequency defined by the length of the cavity, such that

$$\delta\omega = \frac{2\pi c}{2L}. \tag{2.17}$$

The number of longitudinal waves present is proportional to the laser bandwidth $\delta\lambda$ over the round trip length $2L$. This can be modeled mathematically with the following assumptions

- Each mode is spaced equally from its neighbour by $\delta\omega$, with $\delta\omega = 2\pi c/2L$.
- Each mode has an equal amplitude.
- There are exactly *N* cavity modes.

The coherent electric field in time where all modes are in phase can be defined as

$$E_{\text{total}}(t) = \sum_{n=0}^{N-1} E_0(t) = E_0(t)\exp(i(\omega_0 + n\delta\omega)t), \tag{2.18}$$

where ω_0 is the lowest frequency. This can be further expanded as a geometric series such that

$$\begin{aligned} E_{\text{total}}(t) =& E_0 \exp(-i\omega_0 t)[1 + \exp(-i\delta\omega t) + \exp(-i\delta\omega t)^2) + ... \\ & \exp(-i\delta\omega t)^N - 1)]. \end{aligned} \tag{2.19}$$

The sum of a geometric series $1+x+x^2+...x^n$ can be written as $(1-x^N)/(1-x)$, in this case $x = \exp(-i\delta\omega t)$ so that the total field can now be written as

$$E_{\text{total}}(t) = E_0 \exp(-i\omega_0 t)\frac{1-\exp(-iN\delta\omega t)}{1-\exp(-i\delta\omega t)}, \tag{2.20}$$

the intensity of which is given by

$$I(t) = E_0^2 \frac{\sin^2(N\delta\omega t/2)}{\sin^2(\delta\omega t/2)}, \tag{2.21}$$

from the numerator it is apparent that the function has zero value for $N\Delta t/2 = n\pi$, and as such there will be no pulse at these points. However when $\Delta t/2 = n\pi$ both denominator and numerator become zero. This causes the intensity to tend to infinity. So to further examine this function L'Hôpital's limit rule will be employed with respect to t, the rule being

$$\lim_{x\to 0}\frac{f(x)}{g(x)} = \lim_{x\to 0}\frac{f'(x)}{g'(x)}. \tag{2.22}$$

Applying the rule to Equation 2.21 with respect to time the intensity can be expanded to

$$I(t) = E_0^2 N \frac{\cos(N\Delta\omega t/2)\sin(N\Delta\omega t/2)}{\cos(\Delta\omega t/2)\sin(N\Delta\omega t/2)}. \tag{2.23}$$

Which also tends to infinity as both numerator and denominator tend to zero. Applying the rule again however yields

$$I \propto N^2 E_0^2, \tag{2.24}$$

from which it is apparent that the intensity of the pulse generated from mode-locking within a defined cavity length is proportional to the square of the number of modes within the spectrum. Increasing the number of modes within this framework is equivalent to increasing the spectral bandwidth of the laser.

2.2.3 Pulse Rate and Pulse Width

In Figure 2.4 three points are labeled, corresponding to a point of zero intensity (a), the following intensity peak of a pulse (b) and the intensity peak of a neighbouring pulse (c). Using these three points the pulse repetition rate and pulse width will be obtained[4]. Point (a) is at a minimum, therefore $N\Delta\omega t_b/2 = (Nn+1)\pi$. Point (b) here is at a maximum, therefore $N\Delta\omega t_b/2 = Nn\pi$, The

[4]Note, the pulse width obtained here is useful for mathematical derivation, but is not easily measurable in reality, typically pulse widths are measured in FWHM, or $1/e^2$ values. The theoretical value obtained here will be as an upper limit to the FWHM or $1/e^2$ value for a real measurable pulse

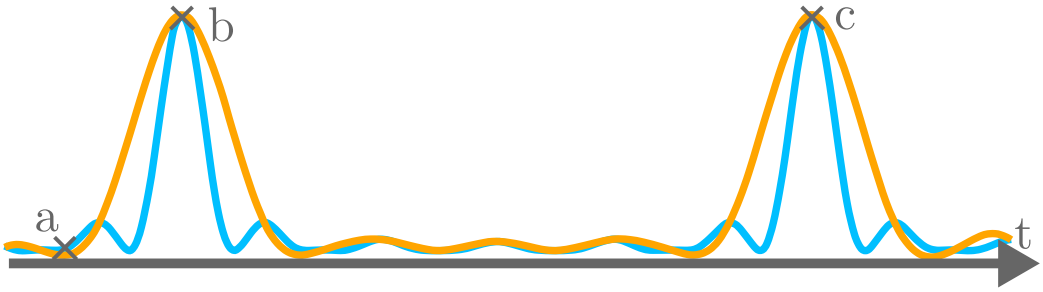

Figure 2.4: Representation of mode locked pulses. With three points labeled, *a* being a point of zero intensity, *b* being maximum intensity, and *c* being the maximum intensity for the following pulse. The intensity field is displayed in blue and the intensity envelope in orange.

pulse width can be defined as twice the distance between points (a) and (b), or $2|t_a - t_b|$ such that

$$|t_a - t_b| = \frac{4\pi}{N\Delta\omega}, \tag{2.25}$$

showing that the pulse duration is inversely proportional to the number of modes present in the cavity within the given bandwidth. The time between points (b) and (c) can be defined in a similar way as above, where point (c) is at a maximum also, resulting in

$$|t_b - t_c| = \frac{2\pi}{\Delta\omega} = \frac{2L}{c}, \tag{2.26}$$

which is the round trip time derived in Equation 2.15. Proving that the number of modes has no effect on the repetition rate of the cavity, which is solely dependent on the length of the cavity.

2.2.4 Chirped Pulse Amplification

Looking at Equations 2.24 and 2.25 it is apparent that as the duration of a pulse reduces by a factor k the peak intensity of the pulse increases by k^2. When considering ultrashort pulses this implies large potential peak intensities, many orders of magnitude higher than that of temporally longer laser pulses[5]. Table 2.1 displays some average powers and typical pulse durations for some common laser systems. It is important to note here, that the total energy of the pulse does

[5]The peak intensity also depends on the beam size and is dependent on which TEM mode the laser is operating in, but for sake of discussion here the spatial dependence of the electric field is ignored and all beams are assumed to be TEM_{00}.

Table 2.1: Example laser systems

System	Wavelength	Pulse duration	Average power
Optically pumped semiconductor	577 nm	10 - 1000 ms	30 - 2000 mW
Diode	810 nm	0.025 ms - ∞	0 - 2000 mW
Q-switched YAG	1064 nm	3 - 10 ns	

not change as the pulse becomes shorter. Simply the peak, or instantaneous intensity increases. Large peak intensities however can have a multitude of nonlinear light-matter interaction effects [49]. Some of the most common being listed below

- Damage to optics [50].
- Self phase modulation [51].
- White light generation [52].

In many applications, both in research and in industry, it is desirable to have high peak power, ultrashort pulses, for

- Material processing, especially in biological or brittle material [53, 54].
- Inducing of high intensity nonlinear interactions [55, 56].
- Micro-fabrication of photonic devices and bio-chips [57, 58].
- Triggering and probing dynamic processes in matter on ultrashort timescales [19, 59].

Large pulse energies are also useful, where the relative transmission of a system is so low that a large initial energy is needed. However trying to amplify ultrashort pulses in traditional ways, such as regenerative or multi-pass amplification can lead to damages in optics due to high peak intensities, effectively limiting the achievable output peak intensity. When a pulse with a high peak intensity passes through optical media nonlinear optical effects occur, which can alter the bandwidth, shape, focusing or duration of a pulse. High intensity pulses can also cause damages in material caused by heating, electron showers or ablation of surface material to name a few. A solution to this issue is the **C**hirped **P**ulse **A**mplification (CPA) technique, which was pioneered by Strickland *et al.* in 1988 [60] and subsequently in 2018 won the Nobel prize. The concept of CPA

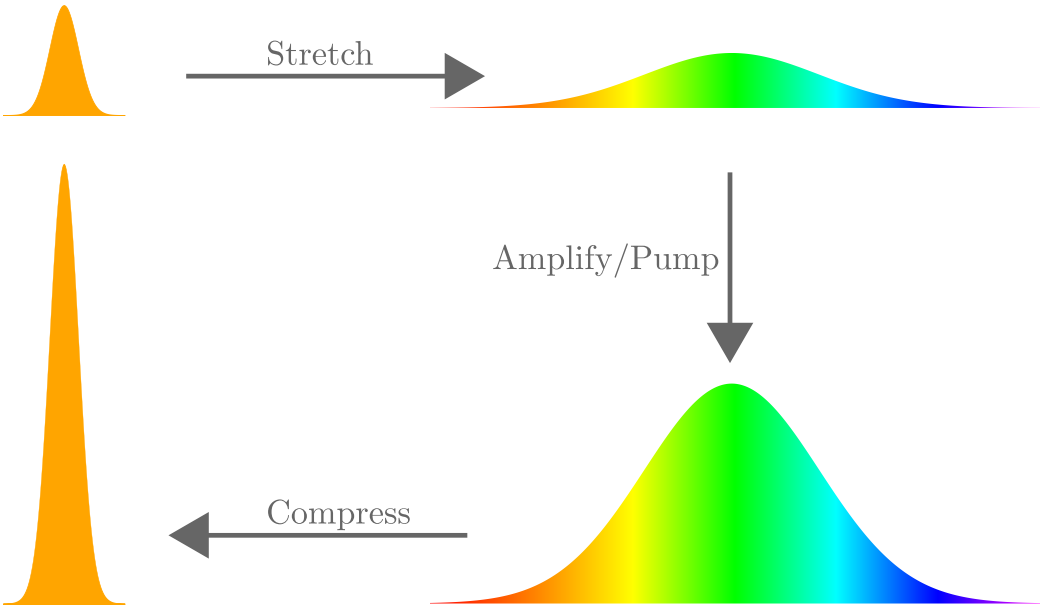

Figure 2.5: Representation of the fundamentals of chirped-pulse amplification. The initial ultrafast pulse is stretched by inducing chirp, this chirped pulse is amplified, and then re-compressed back to it's initial pulse duration, with a larger peak intensity.

consists of three conceptually simple steps, which can be visualised in Figure 2.5. First an ultrashort pulse is stretched using two dispersive elements, such as gratings or prisms. This chirped pulse has a longer pulse duration, and therefore a lower peak intensity, this pulse can then be safely amplified, typically by regenerative or multi-pass amplification, to high energies while retaining a relatively low peak intensity. This prevents damages being induced in the amplification crystal. After the pulse has finished being amplified, it is recompressed back to its original pulse duration, using another grating or prism pair. This process allows high energy, large peak intensity short pulses to be achieved in a large range of frequencies without causing damage to optics within the gain medium [61].

2.3 XUV Sources

In the XUV range a method to generate high-power pulses is to forgo the optics as far as possible, generating the pulse in a single-pass amplifier. This is also especially useful within the short-wavelength regime where transmissive optics are inefficient. Two principle sources of short pulses in XUV photon range in this way are FELs and HHG sources. These sources can provide brilliant, short-wavelength pulses with short pulse durations. FELs however do not typically

produce longitudinally coherent light and specific seeding schemes are required to achieve this. The concepts behind these sources and schemes will be covered in this section.

2.3.1 Free-electron Laser Physics in a Nutshell

FELs can provide peak power up to the GW regime with tunable wavelengths ranging from sub-nm up to the cm wavelengths, dependent upon the machine setup and the electron beam parameters that are possible in the FEL [62–64]. FELs typically generate what is called **S**elf-**A**mplified **S**pontaneous **E**mission radiation (SASE). For high-gain FELs, the most well-established method to generate FEL light is SASE. Albeit having the potential of high brilliances and short pulse durations, SASE pulses do not typically have good longitudinal coherence, because different longitudinal modes[6] can start independently from each other from noise and therefore have no defined phase relation. Longitudinal (or temporal) coherence is defined as a correlation between the electric fields at one location but different times, or as the development of the electric field with respect to time. Referring to Figure 2.1 is a visual representation of two pulses that vary longitudinally as seen by the carrier wave underneath the electric field envelope. To generate fully coherent, high-brilliance, broadband pulses from an FEL, a seeding scheme is needed. Brilliance here being defined as the number of photons of a given wavelength (within a percentage bandwidth of the central wavelength) and direction which are concentrated on a spot per unit time, or as

$$\text{Brilliance} = \frac{\text{Number of photons}}{\text{Second} \cdot \text{mrad}^2 \cdot \text{mm}^2 \cdot 0.1\,\% \text{ Bandwidth}}. \tag{2.27}$$

A seeding scheme is where an external coherent seed laser is introduced into the FEL, modulating the space-charge distribution of the electrons in the electron bunches at the seed lasers frequency, imparting its longitudinal coherence onto the electron bunch, which then further imparts this coherence onto the amplified radiation emitted as the electrons travel through the FEL [65]. Although self-seeding schemes also exist where the "external" laser is generated by an upstream undulator, providing a self contained seed laser [66–68]. Self-seeding is still dependent on the SASE process, ending up with shot-to-shot fluctuations in the intensity. So even though a single spike spectrum is achieved, the stability that seeding offers isn't gained.

[6] The equivalence to the longitudinal modes of "normal" lasers does not hold perfectly. The modes don't have a fixed spacing as there is no cavity, which means the frequency of the modes is essentially random. Usually these "modes" have a significant width by themselves, again because of the lack of a cavity.

FELs work on the principle of synchrotron radiation (magnetobremsstrahlung) [9]. A brief overview of FEL physics will be given here, for a more complete understanding the reader is referred to literature [69]. In an FEL electrons are repeatedly radially accelerated in reverse directions along a linear undulator, which is comprised of an alternating magnetic structure, a representation of a planar undulator can be seen in Figure 2.6. The electrons move on sinusoidal trajectories driven by the Lorentz forces. Depending on the characteristics of the oscillation, different radiation frequencies can be emitted. The instantaneous power of a charged particle accelerated radially through a vacuum is given by,

$$P = \frac{cq^2\gamma^4}{6\pi\epsilon_0 R^2}, \tag{2.28}$$

where c is defined as the speed of light, q is the particles given charge, γ is the Lorentz factor of the particle, ϵ_0 is the permittivity of the vacuum, and R is the bending radius travelled. At the FEL facility in Hamburg FLASH, located on the DESY campus, all the undulators are planar, with the undulators consisting of alternating magnetic dipoles.

As the electrons travel along a sinusoidal path through the undulator, the radiation emitted traverses a cone centered along the direction of the electrons instantaneous trajectory. Due to the movement of the electrons down the undulator with a set periodicity, the photons emitted along the direction of electron propagation experience strong constructive interference within a band around the central resonance wavelength, which is given by

$$\lambda_{\text{rad}} = \frac{\lambda_\mu}{2\gamma^2}(1 + \frac{K_\mu^2}{2}), \tag{2.29}$$

where K_μ is given by

$$K_\mu = \frac{\lambda_\mu B_0}{2\pi m_{\text{e}}}, \tag{2.30}$$

and B_0 is defined as the on axis magnetic field, e is the charge of an electron, and m_{e} is the mass of an electron. The synchrotron radiation emitted from electrons in an FEL is polarised parallel with respect to the plane of oscillation of the electrons. The spectral bandwidth of such radiation is given by

$$\Delta\omega \approx \frac{\omega_{\text{rad}}}{N_\mu}, \tag{2.31}$$

where ω_{rad} is the central emitted frequency, or resonant wavelength and N_μ is the number of periods before saturation kicks in. According to Equations 2.29 and 2.31 the emitted wavelength on resonance is determined by the gap of the undulator and the kinetic energy of the electrons passing the undulator, as the

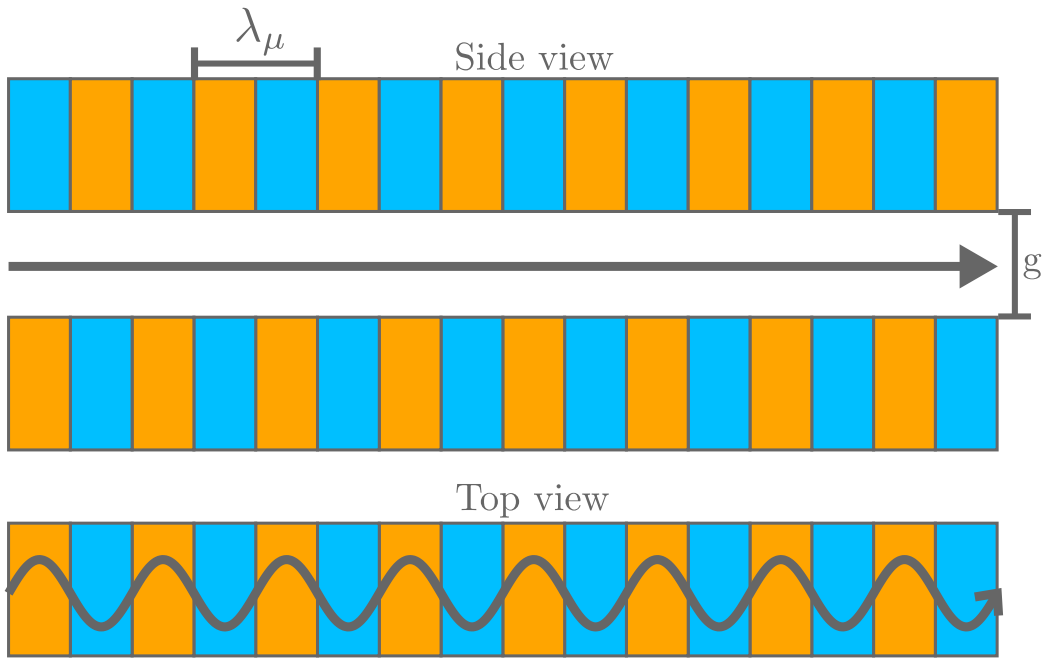

Figure 2.6: Top and side view of a planar FEL undulator. Alternating magnetic polarities represented by blue and orange. The electrons travel along the grey path. The distance between alternating dipoles of the same polarity is defined as the undulator period λ_μ. The distance between the dipoles is defined as the undulator gap g. This gap can be varied, increasing or decreasing the magnetic field strength thereby changing the frequency of radiation emitted from the FEL.

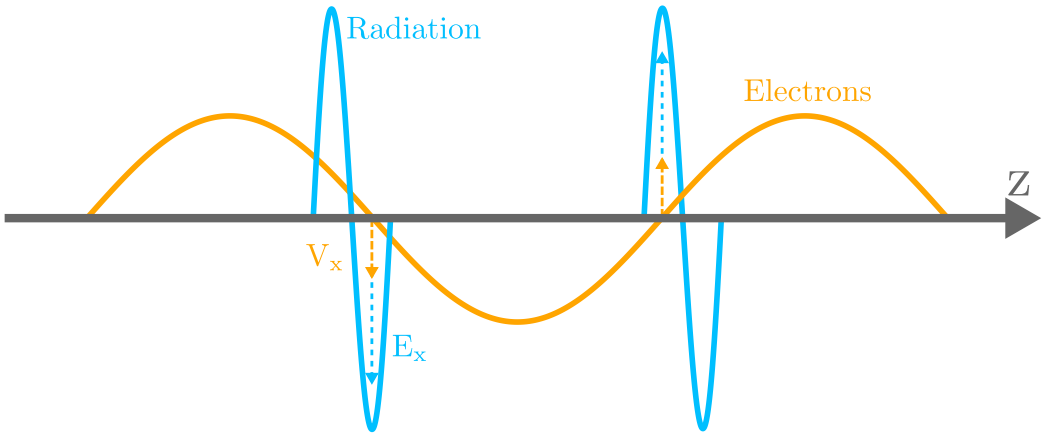

Figure 2.7: Electron-radiation coupling in an undulator. Coupling takes place in the electron oscillation plane, between the electrons (orange) and the light electric field (blue).

magnetic field strength experienced by the electrons increases as the undulator gap decreases.

2.3.2 Self-amplified Spontaneous Emission Radiation

Conventional FELs radiate in SASE mode, where the bremsstrahlung emitted from changing electron trajectories causes a disparity in energy between individual electrons in the bunch. Electrons with a lower energy travel on a sinusoid with higher amplitude compared to electrons that have higher energy, due to their lower momentum and the nearly identical magnetic force because of their ultra-relativistic speed. This causes a retardation of the lower energy electrons within the bunch compared to the higher energy electrons, bunching them together in space. Then later electrons are accelerated by the light field to fly slightly shorter paths so as to catch up to the ones before, which fly on a longer path, the coupling of the acceleration can be seen in Figure 2.7. The radiation emitted from these bunches separated in space by the undulator resonant wavelength, will constructively interfere (see Equation 2.29). Multiple bunches occur separated at the undulator resonant wavelength, this process is called *microbunching*. From the definition of *superradiance*, the intensity of the emitted radiation grows with the square of the number of electrons in these microbunches [70]. An example of microbunching can be seen in Figure 2.8. The microbunch density is eventually limited by Coulomb repulsion. Amplification in a SASE FEL starts from the shot noise present in the electron beam meaning the SASE FEL radiation itself is of stochastic nature, limiting the temporal coherence of the pulses emitted [71].

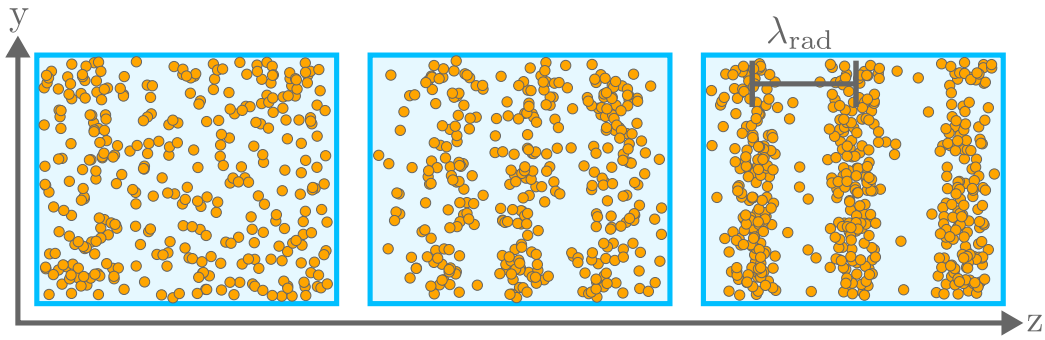

Figure 2.8: Microbunching in an FEL. From left to right the process of microbunching is shown. Electrons in the undulator initially start unhomogeneously spread out in phase space, then begin to bunch as lower energy electrons are retarded compared to higher energy electrons. Eventually microbunches form, separated by the undulator resonant wavelength λ_{rad}.

2.3.3 Seeded Free-electron Lasers

As mentioned due to the stochastic nature of the charge density distribution in the generated electron bunch in SASE FELs, pulses emitted have a limited longitudinal coherence. One solution to this is the concept of a seeded FEL [65]. An intense seed laser is propagated through the FEL such that it travels along the same path as the electron bunch. The electrons, moving on the sinusoidal trajectory, react to the presence of the strong electric field caused by the laser, which induces a kinetic energy modulation on the electrons. Subsequently microbunches are formed in the following magnetic chicane. By initiating microbunching this way, the electron bunch can inherit properties of the seed laser. This can allow radiation emitted by the seeded FEL to be *seeded* with properties of the laser e.g. longitudinal coherence. Seeded FELs emit amplified radiation at a harmonic of the seed laser. Which harmonic depends on factors like the radiator gap. Temporal coherence provided by seeded FELs allows for a new class of light-phase sensitive experiments in the short-wavelength limit, such as nonlinear four-wave mixing and attosecond coherent control [26, 72–76]. Compared to SASE FELs, the longitudinal coherence offered by seeded FELs is exemplary [77]. Seeded FELs are characterised by great stability and shot-to-shot reproducibility. In a SASE FEL the spectral distribution fluctuates shot-to-shot and is comprised of a series of uncorrelated coherent spikes within the amplification bandwidth of the SASE FEL. In SASE mode it is very important to have high peak current on the order of kA and this is achieved by compressing the entire electron bunch with

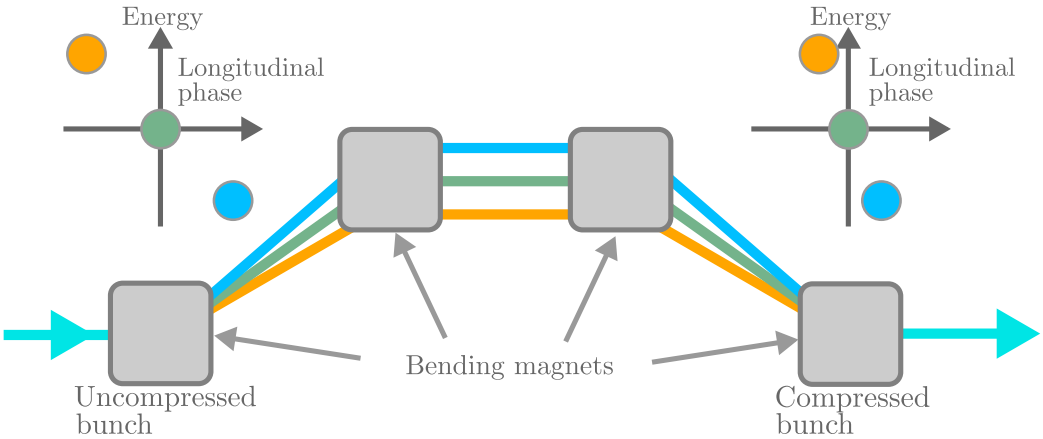

Figure 2.9: Close up of magnetic chicane in FEL. Usually before compression high-energy electrons travel in the head of the bunch (blue) and low-energy in the end of it (orange). This leads to a compression of the longitudinal-energy distribution of the bunch. The strength of the chicane magnets can be adjusted to allow control over the bunch properties, such as the electron bunch peak current and bunch length.

bunch compressors, which are in most cases 4 dipole chicanes. These bunching chicanes use external magnets to change the electron trajectories, inducing a longer path length for lower energy electrons and a shorter for higher energy electrons. An example of such a bunching chicane can be seen in Figure 2.9.

Two primary methods of seeding currently used are **H**igh **G**ain **H**armonic **G**eneration (HGHG) and **E**cho **E**nabled **H**armonic **G**eneration (EEHG) [78]. A typical HGHG setup can be seen and is described in Figure 2.10(a) and an EEHG setup in Figure 2.10(b). Within both seeding schemes, only part of the longitudinal electron bunch is *seeded*. The rest of the bunch emits SASE radiation and as such care needs to be taken that the HGHG or EEHG radiation is orders of magnitude more intense than the SASE, in order to distinguish it. EEHG provides the potential to reach shorter operational wavelengths than HGHG, at the cost of a more complex setup. A detailed discussion on the design and operation of HGHG and EEHG FELs can be found in [36, 79]. Seeded FELs such as those at FERMI in Trieste Italy, and X-Seed at DESY in Hamburg have shown promising results within the HGHG seeding scheme [65, 80] and within the EEHG seeding scheme at FERMI [81].

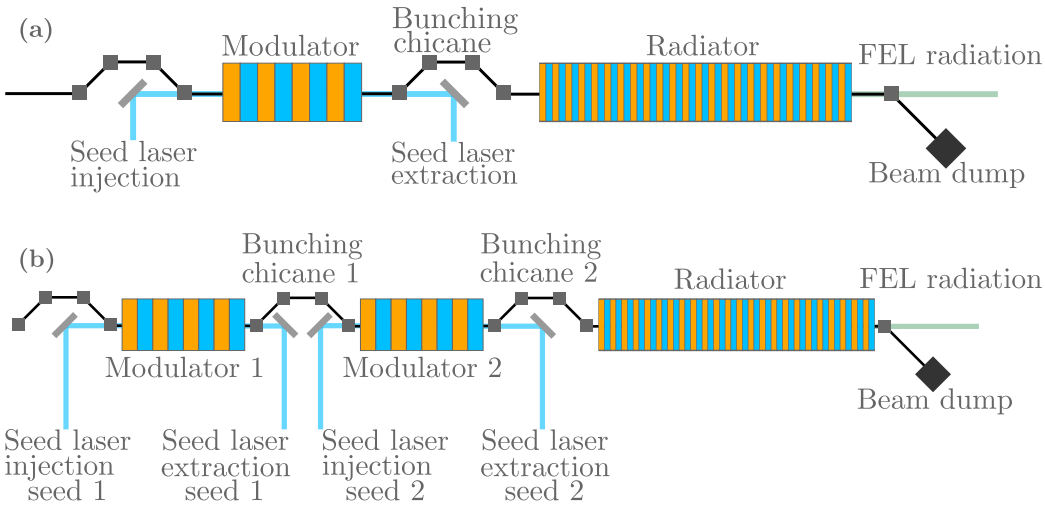

Figure 2.10: (a) Example setup of High Gain Harmonic Generation. A seed laser modulates the kinetic energy distribution of the electrons within the microbunches in the modulator. The bunching chicane turns the energy modulation into a density modulation. Subsequent microbunches (slices) of high electron density are separated by the seed laser wavelength due to the interaction of the intense electric field with the electrons. (b) Example setup of Echo Enabled Harmonic Generation. A seed laser modulates the electron bunch in a similar way to HGHG as in (a) in modulator 1, a second seed pulse, delayed in time with respect to the first, then modulates the already modulated bunch in a modulator 2. This allows higher harmonics to be achieved.

2.4 High-harmonic Generation in a Nutshell

Another source of coherent short-wavelength pulses is **H**igh **H**armonic **G**eneration (HHG) where an intense driving laser (typically in the NIR) stimulates a gas (or sometimes solid) target causing ionisation, acceleration and subsequent recombination of electrons with a target [82]. The recombination of the electron with the ion nucleus causes energy to be released in the form of a high energy photon, which then comprises the generated HHG pulse. Due to the involvement of a 'seed' laser, the HHG pulses exhibit high spatial and temporal coherence, inherited from the long-wavelength drive laser. A representation of these processes along the lines of the 3-step model pioneered by Corkum *et al.* [83, 84] can be seen in Figure 2.11 and in Figure 2.12. The emitted HHG photons are typically odd harmonics of the pump pulse[7], therefore introducing a tunable pump also allows tunability over the HHG photons [86]. The energy acquired by the electron in the driving light field, and thus the energy of the emitted photon, corresponds to the ponderomotive energy of the electron[8]. In comparison to traditional SASE FEL sources, which have limited temporal coherence, HHG sources can be used for experiments where temporal coherence is a necessity. FELs provide peak brilliances much higher than HHG sources. In comparison to seeded FELs, which can emit at temporally coherent high brilliances, they can be viewed as superior in regards to both reduced setup space and generation of coherent attosecond pulses [88, 89]. A detailed description of the underlying physics of HHG sources are beyond the scope of this work, and can be found for instance in [47, 90].

2.5 Theory of Nonlinear Frequency Conversion

Within this work nonlinear frequency conversion is used to both generate the femtosecond pulses in the **D**eep **U**ltra**v**iolet (DUV) spectral range and to subsequently characterise them, as such the theory behind the processes used to perform these operations will be considered and discussed. Nonlinear frequency conversion is based on the idea of converting photons of one or more frequencies, into those of another. This process is performed using some material to help facilitate the conversion, generally called a nonlinear medium, often crystals. These effects are described as nonlinear because, to quote Boyd, 'Nonlinear optical phenomena are "nonlinear" in the sense that they occur when the response of a material system to an applied optical field depends in a nonlinear manner on the strength of the optical field' [49]. This effect was first shown ex-

[7] This is true only for an anisotropic medium, see e.g. [85].

[8] In strong-field laser physics, ponderomotive energy of a free electron in an electromagnetic field is the cycle-averaged quiver energy, for more information the reader is referred to [87] P.339.

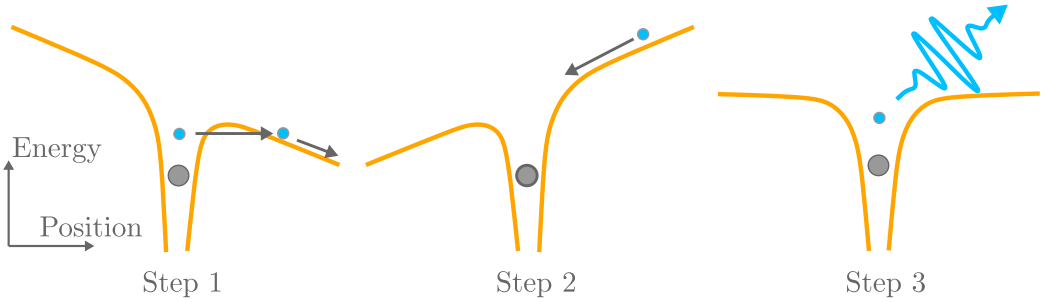

Figure 2.11: Three-step process of High Harmonic Generation. Step 1: the Coulomb potential of the atom (orange) is distorted by an applied external electric field. This allows tunnel ionisation of an electron (blue). Step 2: the free electron is accelerated towards the parent ion (grey) in the next cycle of the lasers electric field. Step 3: the electron recombines with the ion and releases the energy as a high-energy photon.

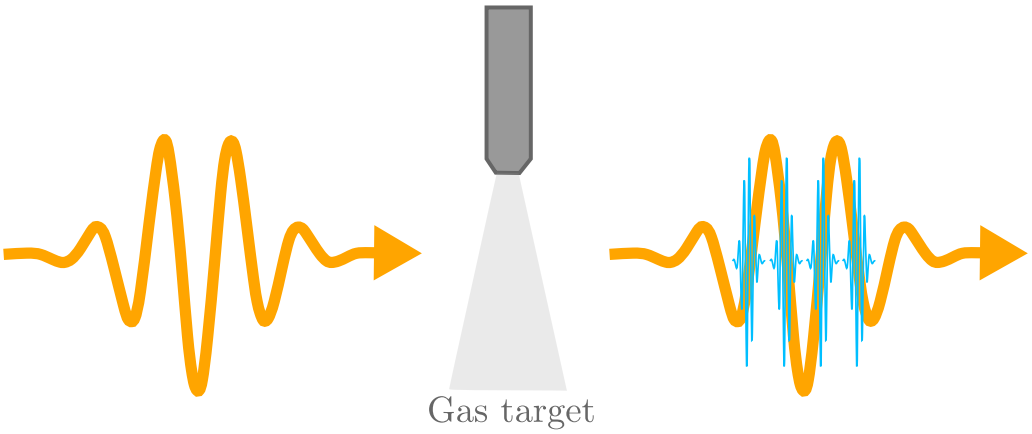

Figure 2.12: Representation of the High Harmonic Generation process. A pump pulse (orange) interacts with a gas target in a vacuum chamber. This stimulates the HHG process, resulting in an out-coming depleted pump pulse and HHG photons (blue) emitted as a pulse containing multiple high harmonics of the pump pulse carrier frequency.

perimentally by Franken *et al.* in 1961 [82]. There is a large variety of nonlinear optical interactions, conversions and effects possible, however within this work only two will be looked at in detail. These are **S**um **F**requency **G**eneration (SFG), and **D**ifference **F**requency **G**eneration (DFG).

To begin with, the linear polarisation of an optical material in response to an applied optical electric field is described as

$$\tilde{P}^1(t) = \epsilon_0 \chi^{(1)} \tilde{E}(t), \tag{2.32}$$

where $\chi^{(1)}$ is defined as the linear susceptibility of the material, ϵ_0 is the permittivity of free space in a vacuum and E(t) is the time-varying electric field as described previously in Equation 2.1. This susceptibility is physically represented in the material as an induced electric polarisation $\tilde{P}$, due to creation of electric dipoles caused by the external field as a function of time. $\tilde{P}$ can be expanded as a power series, such that it can be written as:

$$\begin{aligned} \tilde{P}(t) =& \epsilon_0(\chi^{(1)}\tilde{E}(t) + \chi^{(2)}\tilde{E}^2(t) + \chi^{(3)}\tilde{E}^3(t) + \chi^{(4)}\tilde{E}^4(t) + \\ & ...\chi^{(n)}\tilde{E}^n(t)), \end{aligned} \tag{2.33}$$

where $\chi^{(1)}$ is defined as the first order susceptibility, $\chi^{(2)}$ as the second order susceptibility, $\chi^{(3)}$ as the third-order susceptibility, ad infinitum. These enumerated terms describe the response of the material to the respective power term of the applied electric field. E.g. $\chi^{(n)}$ represents the response of the material to the electric field to the n^{th} power. The susceptibilities correlate to specific groupings of optical nonlinear effects, $\chi^{(2)}$ being defined as the second order nonlinear susceptibility, $\chi^{(3)}$ as the third-order nonlinear susceptibility and so forth. Typically values of $\chi^{(n)}$ for ascending orders of power decrease quite significantly, for example values for $\chi^{(2)}$ are orders of magnitude smaller than those of $\chi^{(1)}$. The physical repercussions of this are that in most materials the second or higher order coefficients are vanishing. Different materials have differing values of $\chi^{(n)}$ and as the n^{th} order polarisation is a function of the electric field to the n^{th} power, the effect of nonlinear response can be increased by using a material with large $\chi^{(n)}$ values, or by using an intense electric field.

The two processes being examined in detail in this work are both second order nonlinear effects dependent on the value of $\chi^{(2)}$. Such that we can now define

$$\tilde{P}^{(2)}(t) = \epsilon_0 \chi^{(2)} \tilde{E}^2(t), \tag{2.34}$$

as the second order nonlinear optical polarisation of the material. For completeness it is noted that

$$\tilde{P}^{(n)}(t) = \epsilon_0 \chi^{(n)} \tilde{E}^n(t), \tag{2.35}$$

represents the *n*th order nonlinear polarisation of the material. The effects higher than the second order will be ignored in this work. For more details and in depth discussion please see [49].

2.5.1 Sum-frequency and Difference-frequency Generation

Here two distinct electric fields will be considered, defined as $\tilde{E}_1(t)$ and $\tilde{E}_2(t)$. From Equation 2.4 these can be written as

$$\tilde{E}_1(t) = E_1 \exp(-i\omega_1 t), \tag{2.36}$$

$$\tilde{E}_2(t) = E_2 \exp(-i\omega_2 t). \tag{2.37}$$

Assuming that at time t, these electric fields are incident on the same spatial position within an optical medium, creating a single electric field, defined simply as $\tilde{E} = \tilde{E}_1 + \tilde{E}_2$, then the second nonlinear polarisation written in Equation 2.34 can be expanded to the following

$$\begin{aligned} \tilde{P}^{(2)}(t) =& \epsilon_0 \chi^{(2)} [E_1^2 \exp(-2i\omega_1 t) + E_2^2 \exp(-2i\omega_2 t) + \\ & 2E_1 E_2 \exp(-i(\omega_1 + \omega_2)t) + \\ & 2E_1 E_2^* \exp(-i(\omega_1 - \omega_2)t) + 2(E_1 E_1^* + E_2 E_2^*)]. \end{aligned} \tag{2.38}$$

The five components present in this expansion each represent a frequency component of the nonlinear polarisation, each of which also represents one of three (four[9]) second order nonlinear effects. The last being largely used in optical parametric amplification to provide lasers with highly tunable wavelength ranges. For more information please see [91–93]. The amplitudes for the effect of SFG are

$$\begin{aligned} P(2\omega_1) &= \epsilon_0 \chi^{(2)} E_1^2. \\ P(2\omega_2) &= \epsilon_0 \chi^{(2)} E_2^2. \\ P(\omega_1 + \omega_2) &= 2\epsilon_0 \chi^{(2)} E_1 E_2. \end{aligned} \tag{2.39}$$

[9] Three distinct effects are present, although second harmonic generation is often labeled separately from sum frequency generation, albeit being the same simply with two of the same frequency laser field.

For DFG being

$$P(\omega_1 - \omega_2) = 2\epsilon_0 \chi^{(2)} E_1 E_2^*, \tag{2.40}$$

and lastly, for completeness, optical rectification being

$$P(0) = 2\epsilon_0 \chi^{(2)} (E_1 E_1^* + E_2 E_2^*). \tag{2.41}$$

From here, only SFG and DFG will be considered.

2.5.2 Phase Matching

The physical representation of the nonlinear polarisation given in Equation 2.34 can be imagined as an induced dipole moment, oscillating at the frequency of the incident electric field ω, within a single atom of the optical media. In the presence of two distinct electric fields, this induced dipole oscillates at a frequency of $\omega_3 = \omega_1 + \omega_2$. However due to the fact that optical media are typically larger than a single atom, a lattice of neighbouring atoms all oscillating at this induced dipole frequency needs to be considered. The field induced by each dipole will interfere with that of its neighbours, either constructively or destructively, thus enhancing or reducing the total field emitted by the whole ensemble of atoms. A constructive interference between these neighbouring fields (when they are in phase with each other) leads to emittance of an electric field with frequency ω_3. Within this convention the field with the highest frequency is called *pump*, the one with the lowest as *idler* and the one in the middle as *signal*. This matching of phases between oscillating atoms within the lattice is given the name phase matching, and is a requirement for successful nonlinear optical conversion. A useful parameter to help quantify this phase matching is the wave vector $\vec{k}_\mathrm{n}$. Which within an optical material has frequency ω_n, and corresponding refractive index n_n, so that

$$|\vec{k}_\mathrm{n}| = \frac{n_\mathrm{n}\omega_\mathrm{n}}{c}. \tag{2.42}$$

The wave vector defines a direction of propagation of the electric field, as well as defining a number of cycles of the wave per unit space. In the perfect case of SFG (where each induced dipole is always in phase with it's neighbours) for each atom in the optical lattice that the sum of two input electric fields with k-vectors $\vec{k}_1$ and $\vec{k}_2$ will produce an output electric field with k-vector $\vec{k}_3$,

$$\vec{k}_3 = \vec{k}_1 + \vec{k}_2. \tag{2.43}$$

For the non perfect case there will be some mismatch between input and output k-vectors, such that we define this k-vector mismatch as

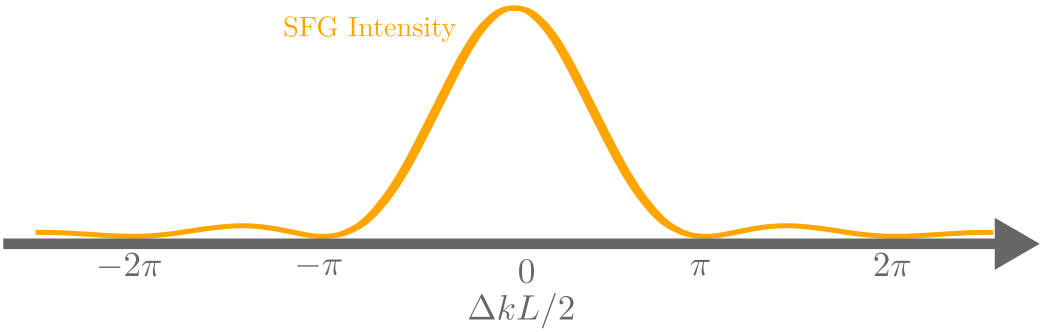

Figure 2.13: Maximum sum-frequency generation (SFG) intensity as the k-vector mismatch moves away from the optimal value of 0. Clearly visible is the large central peak surrounded by small satellite peaks between the integer values of π.

$$\Delta k = |\vec{k}_1| + |\vec{k}_2| - |\vec{k}_3|. \tag{2.44}$$

By defining a length, L, that the incident electric fields travel through in an optical crystal, the intensity of the electric field produced by SFG can be written proportional to

$$I_{\text{SFG}} \propto \text{sinc}^2(\Delta kL/2), \tag{2.45}$$

showing that the intensity of the output field is maximum when the k-vector phase mismatch is 0, and rapidly decreases to 0 as the value of Δk moves away from this optimal value. This can be seen in Figure 2.13. From Equations 2.42 and 2.43 it is clear that for perfect phase matching and for two incident fields propagating in the same direction,

$$n_3\omega_3 = n_1\omega_1 + n_2\omega_2, \tag{2.46}$$

with

$$\omega_3 = \omega_1 + \omega_2, \tag{2.47}$$

the relation in Equation 2.46 cannot be reached, as it requires the refractive index for each frequency within the optical media to be the same, such that $n_1 = n_2 = n_3$. Considering Cauchy's equation[10]

$$n(\omega_{\text{n}}) = A + B\frac{\omega_{\text{n}}^2}{c^2} + C\frac{\omega_{\text{n}}^4}{c^4} + ... \tag{2.48}$$

this is not possible for values $\omega_1 < \omega_2 < \omega_3$.

[10]The coefficients A, B, and C... in Cauchy's equation vary for each optical medium.

2.5.3 Birefringent Crystals

One common solution to fulfill the phase-matching condition in Equation 2.46 is to use birefringent optical media. Media are called birefringent if their refractive index varies as a function of an angle between the polarisation of the incoming light and a certain direction inside the crystal called optical axis. The refractive index for ordinary polarised light is defined as n_o and for extraordinary light as n_e. Ordinary polarised light oscillates perpendicular to the plane formed by the optical axis and $\vec{k}$ whereas extraordinary polarised light oscillates parallel to the plane of the optical axis and vector $\vec{k}$. By exploiting this polarisation dependence it is possible to vary the refractive index of typically the higher frequency input field so that the equality in Equation 2.46 can be reached. This can be visualised in Figure 2.14.

The type of phase matching described in Figure 2.14 is termed Type II phase matching, defined where the ordinary field is a lower frequency and takes advantage of the larger refractive index, and the extraordinary field is at a larger frequency and takes advantage of the lower refractive index provided by the birefringent media. This type of phase matching is typically employed when there is a relatively large frequency difference between ω_1 and ω_2, thus a large difference between n_o and n_e, allowing phase matching to be achieved. Type I phase matching is defined as where the two incident fields ω_1 and ω_2 have the same polarisation, this is commonly used for SFG where the refractive index for each field does not vary much. In Type I phase matching, the output field has an orthogonal polarisation to the two input fields. It is possible to have some limited control over the phase matching within birefringent crystals by both angular or

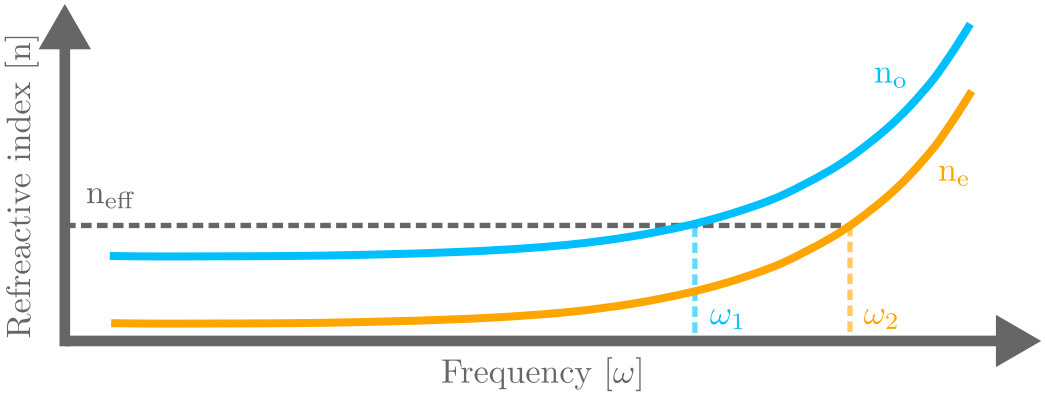

Figure 2.14: Visualisation of birefringent refractive indexes n_o and n_e for increasing frequency. Labeled on the graph is refractive index n_{eff}, defined as the point where frequencies ω_1 and ω_2 have the same refractive index, when ω_1 has an ordinary and ω_2 and extraordinary polarisation. Where $\omega_2 > \omega_1$.

temperature control. The angular control is due to the relative angle between the polarisation of the input fields, and the optical axis of the crystal. We define an effective refractive index of a birefringent media as n_{eff} and define the angle between $\vec{k}$ and the optical axis as θ. The refractive index can be written in the form

$$\frac{1}{n_{\text{eff}}(\theta)^2} = \frac{\sin^2\theta}{{n_{\text{e}}}^2} + \frac{\cos^2\theta}{{n_{\text{o}}}^2}, \tag{2.49}$$

where n_{e} and n_{o} are the refractive indexes for the ordinary and extraordinary polarisation of the input field. By varying angle θ between the optical axis and $\vec{k}$ it is possible to adjust the phase matching condition to produce the optimal output intensity[11]. Temperature tuning of phase matching works on the principle that refractive index varies with temperature. This is not used within this work and is mentioned for completeness, but will not be discussed further.

2.5.4 Bandwidth Phase Matching

It is worth noting, that for the theory discussed within this chapter so far only monochromatic electric fields have been considered. In real world applications, typically laser beams have a certain bandwidth containing many frequency components. From Equation 2.48 it is clear that the refractive index of a material varies with wavelength, therefore for a beam with bandwidth $\Delta\lambda$ is natural to assume there is also a range of refractive indexes present. Considering this, it is apparent that perfect phase matching can only exist for a single frequency within this bandwidth, and the rest of the bandwidth must lie in some state of imperfect phase matching. This by itself is not inherently fatal, judging from Figure 2.13 it is clear that high output intensities also lie slightly to the side of the perfect center. Defining the FWHM limits of the bandwidth as λ_+ and λ_- the phase mismatch of the lower and upper limit can be defined as Δk_+ and Δk_-. Considering Equation 2.45 and Figure 2.13 it is clear that, for a defined crystal length, as the bandwidth broadens, the phase matched part of the bandwidth reaches a limit when $\Delta k_+ = \pi$ and $\Delta k_- = -\pi$, halting any further substantial phase matching. The consequence of this is simply that for large input bandwidths the crystal length L needs to be reduced to match the entire bandwidth.

2.6 A 4-f Pulse Shaper

A brief discussion of the fundamentals behind femtosecond pulse shaping by means of a 4-f line will be presented here. For a more complete theoretical description see [33]. The general concept of a 4-f shaper can be imagined as a five step process.

- **Step 1:** An input collimated beam is diffracted by a grating or prism.
- **Step 2:** The diffracted beam travels a length f after which it is focused by a focusing optic with focal length also f.
- **Step 3:** Travelling once again a length of f the focused dispersed beam reaches the **F**ourier **P**lane (FP), such that each frequency component is spatially separate. If a shaping operation is performed, it is done here.
- **Step 4:** The beam travels once again a length f and reaches an identical focusing optic to the first.
- **Step 5:** Travelling the last length f, the beam reaches an identical dispersing optic to the first, and exits the device once more collimated.

[11] This is especially helpful as often in the real world there is a slight disparity between specified crystal cut angles and the actual value.

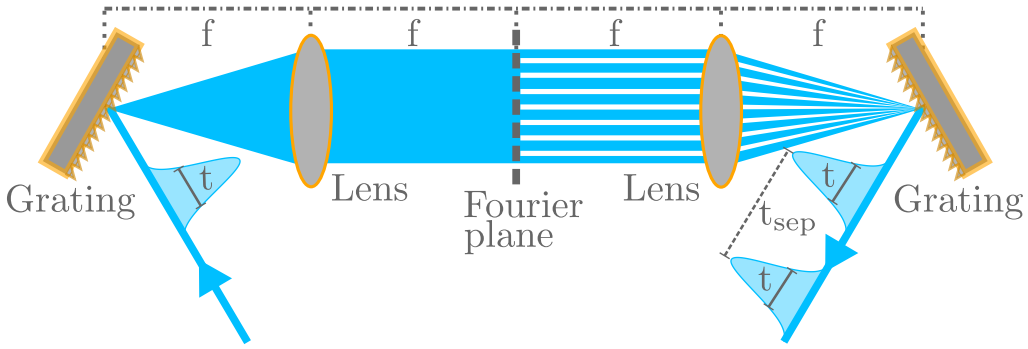

Figure 2.15: Typical 4-f pulse shaper setup. A grating diffracts the incoming pulse that is subsequently focused by a focusing optic with focal length f onto the Fourier plane such that each frequency component is present at a different spatial point. This process is then reversed with an identical focusing optic and grating. The temporal profile of the output pulse depends on phase or/and amplitude changes that were made to individual frequencies in the Fourier plane, if any. Here a simple amplitude-shaped pulse is shown as an example: a single pulse with duration t enters the device, the amplitude mask blocks a range of frequencies in a periodic manner, and that produces a pulse pair, also with pulse durations t, separated by a time t_{sep} at the exit of the device.

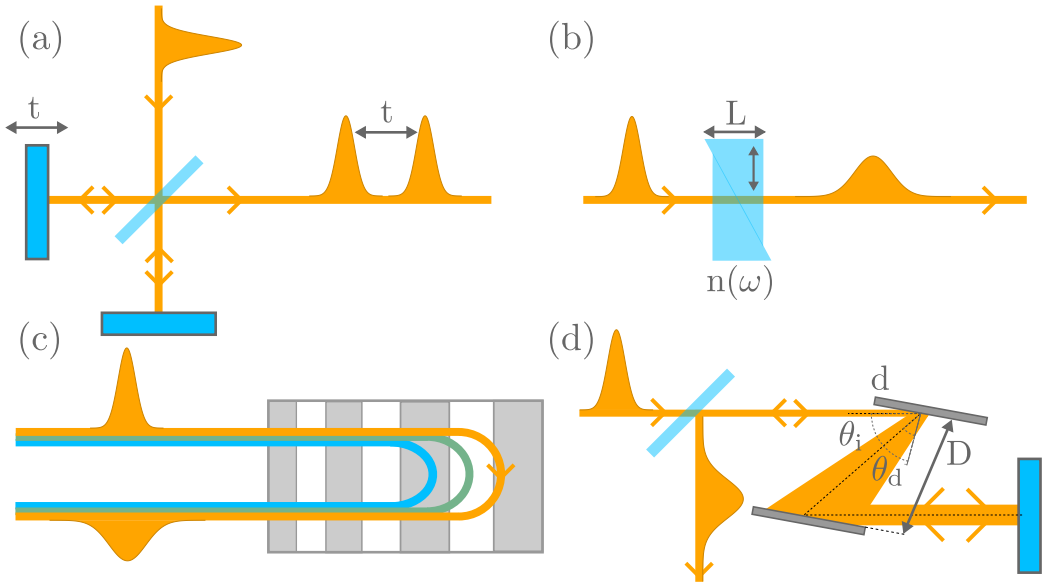

Figure 2.16: Four examples of some basic shaping devices. A Michelson interferomter (a) acting as a split and delay unit, a variable glass wedge pair inducing a variable chirp (b), a chirped mirror introducing a set chirp (c) and a grating stretcher introducing a variable chirp (d).

Each optic in this setup is separated by the focal distance of the identical focusing optics, such that the length between the first and last optic is four times the focal length f, hence the name 4-f. An example of the typical 4-f setup can be seen in Figure 2.15. By placing no optical element in the FP the beam undergoes no changes, hence the output beam will be identical to the input. Such a setup is called a zero dispersion line. However by placing a special mask in the Fourier plane, such that one can alter the path or amplitude of certain frequencies as one wishes, arbitrary pulse profiles at the output can be generated. Some simpler devices designs are shown in Figure 2.16 which can also be used to shape pulses, however these are capable of shaping in limited ways.

To mathematically describe the effect of a 4-f pulse shaper on a pulse we assume that the input beam is Gaussian in time, frequency and space. We also define the central frequency of our pulse as ω_0 and take the FWHM values of the spectral width $\Delta\omega_{\mathrm{L}}$, the pulse duration Δt and the beam waist Δx_{in}. The input pulse is diffracted by the first grating and each spectral component will diffract at a slightly different angle. Defining the input beam angle of incidence as θ_{i} and central wavelength λ_0, it is initially diffracted at an angle θ_{d} by the first grating dependent on the grating period d. Defining f as the focal length of the following focusing optics, and assuming diffraction-limited focusing, the spatial width of each spectral component in the Fourier plane can be written as

$$\Delta x_0 = 2\ln(2)\frac{\sin(\theta_\mathrm{i})f\lambda_0}{\sin(\theta_\mathrm{d})\pi\Delta x_\mathrm{in}}, \tag{2.50}$$

where Δx_in is defined as the input FWHM beam diameter. The spatial position, X_k, of each angular frequency component, ω_k, can also be defined for a 4-f shaper as,

$$X_\mathrm{k} = \omega_\mathrm{k}\frac{\lambda_0^2 f}{2\pi c d\sin(\theta_\mathrm{d})}, \tag{2.51}$$

where c is the speed of light. From Equation 2.51 it is clear that each spectral component is separated at a different spatial position in the Fourier plane, allowing amplitude and phase transformations to be performed on chosen parts of the dispersed spectrum. It can be assumed that an arbitrary frequency ω would lie at a spatial position X in the Fourier plane, such that

$$X = \alpha\omega, \tag{2.52}$$

where α is a constant set by the 4-f geometry such that

$$\alpha = \frac{\lambda_0^2 f}{2\pi c d\sin(\theta_d)}. \tag{2.53}$$

For spectral resolution one derives

$$\frac{\delta\omega}{X_\mathrm{k}} = \Delta x_0\frac{2\pi c d\sin\theta_\mathrm{d}}{\lambda_0^2 f}. \tag{2.54}$$

Using this constant we can also obtain the frequency resolution $\delta\omega$ which is such that

$$\delta\omega = \frac{\Delta x_0}{\alpha}X_\mathrm{k}, \tag{2.55}$$

which by a Fourier transform corresponds to a time window T.

$$T = \frac{4\ln 2}{\delta\omega} = \Delta x_\mathrm{in}\left|\frac{\lambda_0}{cd\sin(\theta_i)}\right| = \Delta x_\mathrm{in}/|v|. \tag{2.56}$$

This link between the time window for shaping and the input beam waist Δx_in is a manifestation of spatio-temporal coupling. The value T defines an upper bound for temporal pulse shaping achievable with a 4-f line, and as such the pulse duration of the input pulse should remain below T, else strong distortions in the output pulse will occur. By placing a mask in the Fourier plane with a defined complex spectral transformation and by defining two operators M_x and

M_ω as the spatial effect and spectral effect of the mask on the pulse, the effect of the mask upon the electric field of the pulse can be written as

$$\tilde{E}_{\text{Output}}(\omega, X) = \tilde{E}_{\text{Input}}(\omega).g(X - \alpha\omega)M_{\text{X}}(X), \tag{2.57}$$

where $g(X)$ is defined as

$$g(X) = \exp\Big[-2\ln 2\Big(\frac{X}{\Delta x_0}\Big)^2\Big]. \tag{2.58}$$

By defining the entire shaping transformation as S(ω), the output pulse can be written as

$$\tilde{E}_{\text{Output}}(\omega) = S(\omega)\tilde{E}_{\text{Input}}(\omega). \tag{2.59}$$

This derivation takes two assumptions, being that

- The beam propagates fully according to Gaussian propagation.
- There is no effect of the phase mask upon the spatial profile of the beam.

In practicality neither of these hold, and must be considered in real world applications. Some common phase and amplitude shaping examples can be seen in Figure 2.17.

2.6.1 Spatio-temporal Coupling

Laser pulses are often temporally described by the variation of their electric field with time, i.e. the intensity and phase. Spatial coordinates are commonly seen as independent to temporal ones. However in ultrafast pulses, due to the large bandwidth required to produce them, this case is not true. This is generally caused by angular dispersion, a broader bandwidth means a pulse will experience more angular spatial distortions after an angularly dispersive element. This effect can limit the effectiveness of a pulse shaper in reaching the desired output, such as by introducing unwanted temporal dispersion, and as such needs to be taken into consideration when designing a 4-f pulse shaper [95].

2.7 DUV Pulse Characterisation

One consideration to take in working with ultrashort optical laser pulses, i.e. how to measure them. How to accurately define the pulse in space, frequency and time? The spatial aspect is easy to determine, using conventional observation methods, such as laser cards or more accurately camera based beam profilers. The

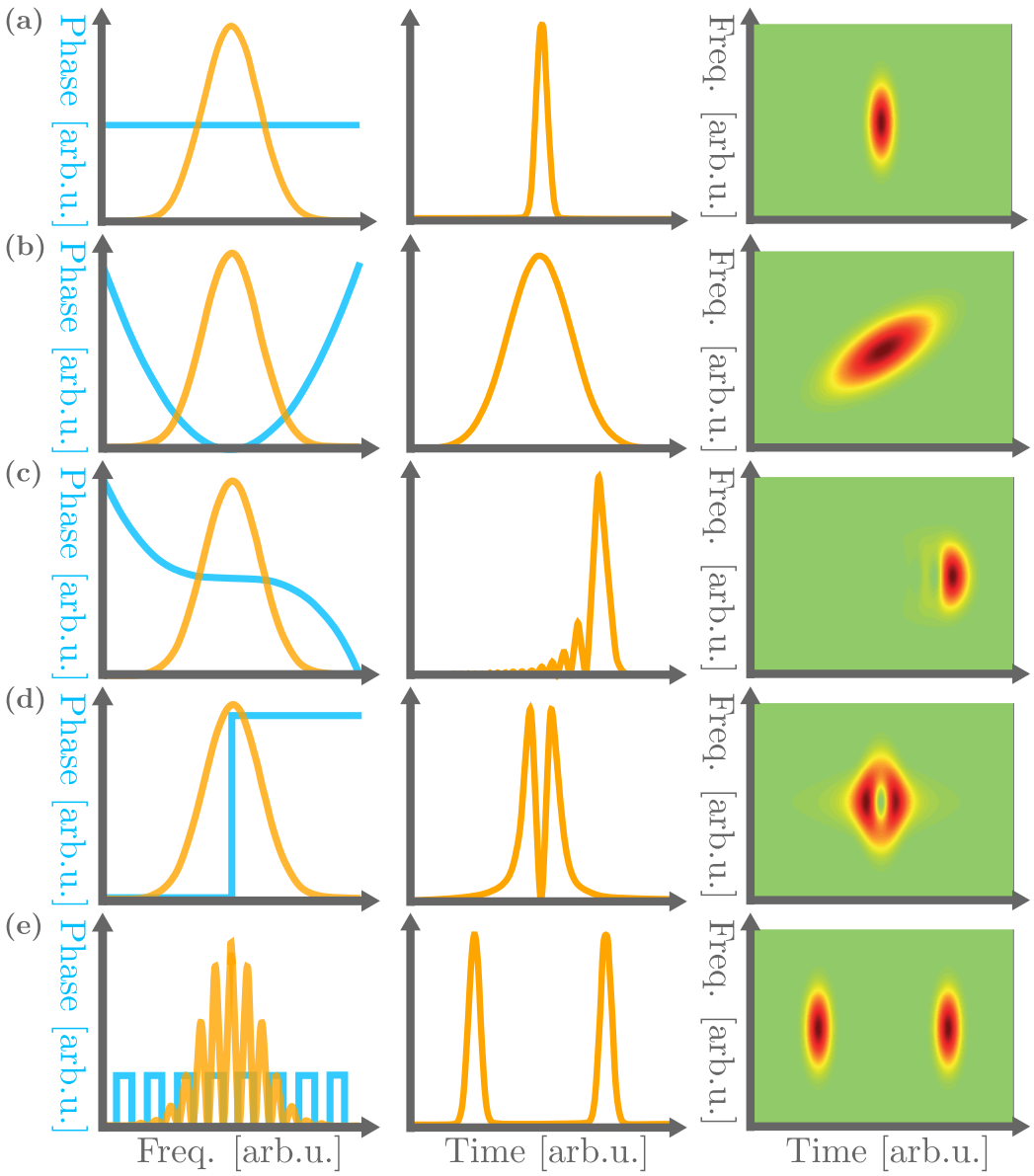

Figure 2.17: From left to right are example spectra and phase, temporal pulse shape and spectrograms for five common phase transformations each with the same initial spectrum (intensity in orange is arbitrary). (a) is a flat phase Fourier limited pulse, (b) is a positively linearly chirped pulse, (c) shows a cubic phase, (d) a spectral π phase jump and (e) a double pulse sequence. Figure adapted from [94].

frequency is also relatively easily retrieved using traditional grating spectrometers[12]. These methods however cannot measure the spectral phase of the pulse and this then leaves the last remaining variable to be the temporal structure of the pulse, comprising the intensity envelope as a function of time and the relative arrival of different constituent frequencies within the pulse, defined as the spectral phase of the pulse. Unfortunately typical electronic and solid state devices lack sufficient temporal resolution to characterise ultrashort pulses. This leaves the question of how to measure such short pulses in a laboratory environment. One such method, and the one employed in this work is the **F**requency **R**esolved **O**ptical **G**ating (FROG) technique. Pioneered by Trebino *et al.* in 1991 [96], the FROG technique is a standard method widely used in ultrashort pulse metrology. It was designed around the principle of, "to measure a temporally short event, one needs to use another equally, if not shorter, event". The short event to be measured here is the pulse itself, and so the FROG technique revolves around the idea of using the pulse to measure itself.

The concept of the FROG technique is based on the principle of optical autocorrelation. The physical principal behind which consists of observing the nonlinear sum-frequency generation caused by the pulse as it overlaps with a copy of itself, the copy being scanned in time over the original. This overlap happening typically, but not always, within a nonlinear medium[13]. In this sense, the resulting second harmonic can be said to correlate to the overlap of the two identical input pulses. However a limit to this method is that there is no detailed information about the constituent frequencies time arrival (sign of the frequency chirp), or more precisely, no spectral phase information is obtained. This is then where the FROG technique comes into play. By looking at the spectrum of the resulting second harmonic using a simple spectrometer, a spectrogram of the generated second harmonic can be built up. This can then be run together with specific algorithms, to retrieve the full time-frequency distribution of the input pulses, i.e. fully characterised in time, spectrum and phase[14].

The limit to be considered within this work is however, that the pulse to be measured has a central wavelength of 266 nm, meaning therefore that the second harmonic would have a central wavelength of 133 nm. This second harmonic has a large absorption cross-section in air, and as such would not be easily measurable and there are simply no suitable nonlinear media available for SFG in

[12]This is not always the case depending on the laser wavelength, however for the 800 nm, 400 nm and 266 nm lasers used in this work this assumption holds.

[13]All permeable matter has nonlinear coefficients, such that nonlinear generation is also possible i.e. in air. The nonlinear response in these media are generally extremely low so are not often used for nonlinear generation.

[14]If one has two identical pulses the time direction cannot be reconstructed. As the retrieved trace is perfectly symmetric in time.

this wavelength range. A simple solution to this comes in the form of a variant to the two aforementioned pulse measurement techniques, second-order auto-correlation and FROG, these being named cross-correlation and subsequently X-FROG. This technique operates in a similar fashion to the previously mentioned two, with the difference being that instead of two identical pulses being measured against each other, instead one unknown pulse is measured against one well known pulse. In this case the 266 nm unknown pulse is cross-correlated with the well-known 810 nm fundamental, using a DFG process to obtain a 405 nm signal. The measured time-dependent spectrum of which can then be used to form a spectrogram, similar to as discussed above. And using an altered retrieval algorithm which takes the properties of the well-known input pulse into account, allows retrieval of the full pulse information of the unknown pulse.

2.7.1 Frequency-resolved Optical Gating Algorithm

In the following section the mathematical description behind X-FROG will be briefly discussed. For derivations of second-order auto-correlation and the FROG algorithm please see [97].

A FROG measurement is a spectrogram of the pulse in time and frequency, created using a gate pulse (or gate function) to generate a measurable signal intensity. A representation can be seen in Figure 2.18. The spectrogram of a pulse is defined as

$$Sp_{\mathrm{E}} \equiv \left| \int_{\infty}^{\infty} E(t)g(t-\tau)\exp(-i\omega t)\mathrm{d}t \right|^2, \tag{2.60}$$

where $g(t-\tau)$ is a variable-delay gate function and τ is the delay. Each time step τ creates a spectral slice, all of which together create the spectrogram. However, of real interest is $E(t)$ of the pulse, not the measured spectrogram, as such algorithms exist to retrieve $E(t)$ from Sp_{E}. To retrieve $E(t)$ the gate function needs

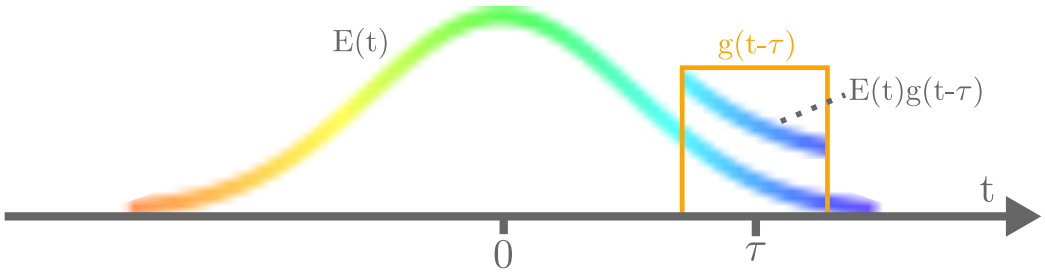

Figure 2.18: Representation of a spectrally chirped pulse in time. With a gate function g (orange) at time τ contributing intensity to a slice of the electric envelope $E(t)$, resulting in a signal electric field $E(t)g(t-\tau)$

to be well-known. The two frequency-resolved optical gating methods used in this work, and thus described here, are SHG FROG and DFG cross-correlation FROG.

- **SHG FROG:** Where the gate pulse is the same as the pulse being measured. Pulses measured in this way give no information to the sign of the chirp.
- **Cross-correlation FROG:** Where the gate pulse is some well-known separate pulse used to characterise the unknown pulse.

Now considering the spectrogram of the signal electric field generated by the nonlinear interaction of the input pulse, and the gate function $E_{\text{signal}}(t,\tau)$ as

$$E_{\text{signal}}(t,\tau) \propto E(t)|E_{\text{gate}}(t-\tau)|^2 \propto E(t)I_{\text{gate}}(t-\tau), \tag{2.61}$$

where $I_{\text{gate}}(t-\tau) = g_{\text{gate}}(t-\tau)$. So by measuring the nonlinear spectrogram, and either by knowing the gate function, or by using the same pulse to measure itself it is possible to fully reconstruct $E(t)$ for time, frequency and phase. The mathematical concepts behind the retrieval are rather complex and are discussed further in [96–98].

2.8 XUV Pulse Characterisation

Previously discussed methods of ultrafast pulse characterisation, such as FROG techniques, work well for table top photon sources, however their usefulness breaks down towards the low wavelength limit. Each of the ultrafast pulse characterisation techniques discussed so far rely on nonlinear interactions within optical media, which is not feasible for wavelengths emitted from sources such as XUV and soft x-ray FELs, due to limited transmissive media available in this wavelength range.

To overcome this limit, other techniques to characterise short-wavelength pulses are required. One such technique is THz streaking. The basis of which is to overlap the short-wavelength pulse with a THz frequency wave (hence the THz in THz streaking) and focus both onto a gas target, typically argon or xenon. The higher photon energy ionises some atoms in the gas target and causing electrons with an energy corresponding to the energy of the incident photon, reduced by the ionisation potential of the atom, to be released. Thus, the energy spectrum of photo-electrons represents a replica of the photon spectrum of the XUV pulse offset by the ionisation potential of the target. The energy of these electrons can be measured using, for example, a **T**ime-**O**f-**F**light spectrometer (ToF). Different electron energies (different flight times) map to different photon energies. By

this a spectrum of the input pulse can be measured by recording the flight time of the particles that can be then converted to energy knowing the geometry of the spectrometer and applied electric fields. This however does not give any time, or phase information of the pulse. To retrieve these two quantities, the effect of the overlapping THz field on the emitted electrons is exploited. A diagram of this can be seen in Figure 2.19.

2.8.1 THz Streaking

THz streaking is based on the interaction of an overlapping THz field with photo electrons released from a gas target. This interaction can be mapped such that the pulse duration and spectra of the incident ionising pulse can be retrieved.

Electrons are released from matter in a process called photo-ionisation, or the photoelectric effect. First proposed by Planck (1900) and Einstein (1905) then proved experimentally by Millikan (1914) the theory states that light carries discrete packets of energy, photons, with an energy $h\nu$, where h is the Planck constant and ν is the photon frequency [99–101]. Considering that in matter, each electron is bound to its atom by energy W, defined as the binding energy of electrons in an atom. To release an electron bound in the atom, the energy of the photon needs to be higher than this binding energy giving the relation:

$$K_{\max} = h\nu - W, \tag{2.62}$$

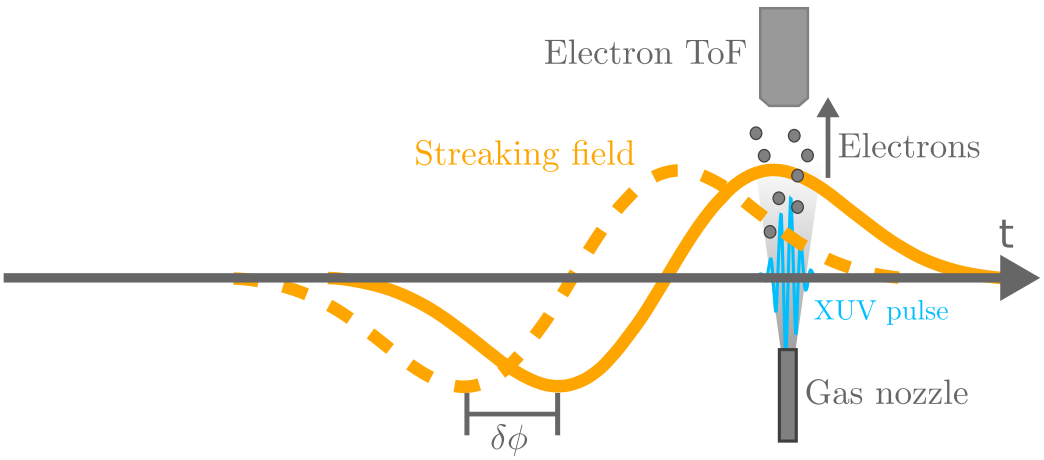

Figure 2.19: Diagram of typical THz streaking setup. Seen in solid and dashed orange are two streaking fields displaced in phase by $\delta\phi$. Here the XUV (blue) acts as the ionising pulse releasing electrons from a gas target, which are then detected by a ToF spectrometer.

where $K_{\max}$ is the maximum kinetic energy of the released electron[15]. Considering a photon pulse with a bandwidth $\Delta\nu$, this can be then mapped to a bandwidth of emitted electron kinetic energies, defined ΔK. By exploiting these differing kinetic energies using a **T**ime **o**f **F**light spectrometer (ToF), a spectrum of the photon pulse can be obtained.

2.8.2 Light-field Streaking

THz streaking is based on the principle of streak cameras, where a photon pulse hits a target acting as a photo-cathode. The electrons produced form a photoelectron wave packet, which is a replica of the incident photon pulse [102]. By combining photoionisation this with a time-varying electric field the electrons are transversely deflected, which maps the temporal structure of the photon pulse onto the electron wave packet. This can be then measured with detectors such as ToF spectrometers to obtain the temporal information of the photon pulse. Limitations to the resolution of such measurements come in the form of space charge effects between individual electrons or the initial spread of the electron momenta. To overcome this limit, the time-varying electric field is replaced with an overlapping, longer wavelength, photon pulse, typically in the THz frequency range, hence the name THz streaking. Depending on the moment of release, electrons experience the overlapping THz field at differing phases, imparting differing energy changes upon these electrons. A visualisation of this energy or momentum change can be seen in Figure 2.20.

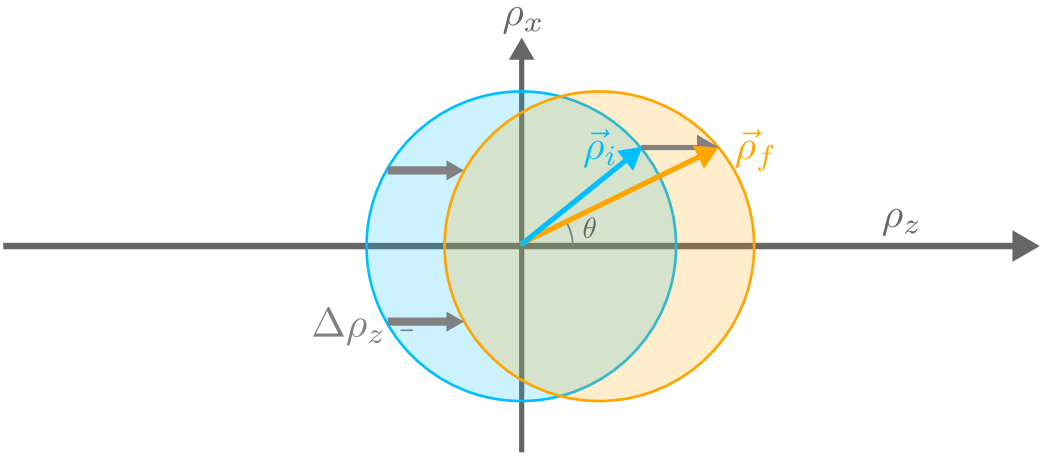

Figure 2.20: Visualisation of the momenta shift electrons gain when in a streaking field. The blue circle represents the initial momenta ρ_{i}, which when under the effect of the external streaking field gain momentum $\Delta\rho_{\mathrm{z}}$ to reach final momenta ρ_{f}.

[15]Nonlinear light-matter interactions and correlation effects inside matter were omitted here.

2.8.3 Classical Picture

An electron that is released with energy K_0 at time t in a linearly polarised electric field E_{streak} where

$$E_{\text{streak}}(t) = E_0(t)\cos(\omega_s t + \phi), \tag{2.63}$$

and ω_s is the frequency of the streaking field. The change in electron momentum due to this linear field is

$$\Delta p(t) = e\int_t^\infty E_{\text{streak}}(t')\mathrm{d}t' = eA_s(t), \tag{2.64}$$

with A_s defined as the vector potential of the streaking field and e is the charge of an electron. The electron has an initial momentum, p_0 when it is released from the cathode. Aggregated with the change in momentum induced by the linear field, the total momentum of the electron at time t is

$$p(t) = p_0 + \Delta p(t), \tag{2.65}$$

giving a final kinetic energy of

$$\begin{aligned} K_{\text{final}} =& \frac{|p(t)|^2}{2m_e} \\ =& K_0 + 2U_p\cos(2\theta)\sin^2(\phi_t), \\ & \pm\cos(\theta)\sin(\phi_i)\sqrt{(1-\frac{2U_p}{K_0}\sin^2(\theta)\sin^2(\phi_t))(8K_0U_p)}, \end{aligned} \tag{2.66}$$

where U_p is the ponderomotive energy, $U_p = e^2E_0^2/4m_e{\omega_s}^2$, m_e is the mass of an electron, ϕ_t is the phase of the streaking field at time t and θ is the direction of propagation of the electron with respect to the polarisation of the streaking field. Thus the final electron kinetic energy is direction dependent for a linearly polarised field. For cases where θ is 90° or 0°, perpendicular or parallel, the final kinetic energy can be written

$$\begin{aligned} K_{\text{final},\parallel} &= K_0 - 2U_p\sin^2(\phi_t) \pm \sin(\phi_t)\sqrt{8K_0U_p}, \\ K_{\text{final},\perp} &= K_0 - 2U_p\sin^2(\phi_t). \end{aligned} \tag{2.67}$$

Electrons released perpendicular to the THz field polarisation will have reduced kinetic energies, whereas electrons released parallel will either increase or decrease in energy depending on the phase of the field at the point of release. In the case where $U_p \ll K_0$ the parallel kinetic energy can be assumed to be

$$K_{\text{final},\parallel} = K_0 \pm \sin(\phi_t)\sqrt{8K_0U_p}. \tag{2.68}$$

For cases where ϕ_t is small (in the small angle approximation) the added kinetic energy can be mapped to the phase of the THz field. Allowing temporal information of the ionising pulse to be retrieved from the released electrons.

2.8.4 Quantum Mechanical Picture

To understand exactly how the ionising XUV pulse affects the photoelectron spectrum the electrons need to be treated as a wave packet. Defining the electrons quantum mechanical wave packet as $|\psi(t)\rangle$ the **T**ime **D**ependent **S**chrödinger **E**quation (TDSE) reads

$$i\frac{\mathrm{d}}{\mathrm{d}t}|\psi(t)\rangle = \hat{H}(t)|\psi(t)\rangle. \tag{2.69}$$

Using the dipole approximation [103], the Hamiltonian can be written as

$$\hat{H}(t) = \frac{1}{2}(\hat{\rho} + A(t)_s)^2 + V_{\text{eff}}(r) + E_{\text{ionising}}(t)\dot{r}, \tag{2.70}$$

with V_{eff} as the effective potential caused by the remaining ion and bound electrons. This approximation is called the "single-active-electron approximation", and is used as solving the full TDSE numerically is complex. Two helpful approximations can be made, these being:

Approximation 1: Ionisation without the streaking field present

Without additional energy introduced by the streaking field the photo electron wave packet replicates the spectral structure of the ionising pulse. The pulse spectra can be retrieved from the photo electron spectra when the transition dipole matrix element $\mathbf{d}_p$ is known, with this the transition amplitude a_p is

$$a_p = \langle\rho|\psi(t)\rangle = -i\int_{-\infty}^{\infty} \mathbf{d}_p\mathbf{E}_{\text{ionising}} \exp(\frac{i}{2}(\rho^2 + 2I_p))\mathrm{d}t, \tag{2.71}$$

where a_p is the population of the final continuum state $|\rho\rangle$.

Approximation 2: Ionisation with the streaking field present

For the case where the emitted electron is in the presence of a streaking field, the transition amplitude can be written as

$$a_{\mathrm{p}} = -i \int_{-\infty}^{\infty} \mathbf{d}_{\mathrm{p(t)}} \mathbf{E}_{\mathrm{ionising}}(t-\tau) \exp(\frac{i}{2}(2I_{\mathrm{p}}t - \int_{t}^{\infty} \rho^2(t')\mathrm{d}t'))\mathrm{d}t, \tag{2.72}$$

where τ is the time delay between the ionising pulse and streaking field and the momentum of the free electrons in the streaking field is $\rho = \rho_0 + A(t_{\mathrm{i}}) - A(t)$. Here we use the strong-field approximation implying that the effect of the ionic potential on the electron motion after ionisation is negligible. Allowing the previous equation to be written

$$a_{\mathrm{p}} = -i \int_{-\infty}^{\infty} \mathbf{d}_{\mathrm{p(t)}} \mathbf{E}_{\mathrm{ionising}} \exp(\frac{i}{2}(\rho^2 + 2I_{\mathrm{p}} + 2\phi_{\mathrm{V}}(t)))\mathrm{d}t, \tag{2.73}$$

with ϕ_{V} as the Volkov phase

$$\phi_{\mathrm{V}} = -\int_{-t}^{\infty} (\rho A(t') + A^2(t')/2)\mathrm{d}t'. \tag{2.74}$$

The photoelectron spectrum for a delay τ between the ionising and streaking field is

$$I(\rho, \tau) = |a_{\mathrm{p}}(\tau)|^2. \tag{2.75}$$

From Equation 2.73 it is clear that the modulated spectrum of the photoelectrons released into the streaking field depends on the time delay τ between the field and the ionising pulse.

2.8.5 Reconstruction of Linearly Chirped Pulses

To reconstruct a linear chirp present in an XUV pulse is difficult, but possible using some approximations. For example it is assumed that the pulse is Gaussian in time and there is only second-order dispersion present (linear chirp). A representation of this process can be seen in Figure 2.21. It is also assumed the streaking field, E_{streak} is linearly polarised and that the ponderomotive energy $U_{\mathrm{p}} \ll K$. Then in the general case the phase modulation can be written as

$$\begin{aligned} \phi(t) = &-\int_{t}^{\infty} U_{\mathrm{p}}(t)\mathrm{d}t + \\ &\frac{\sqrt{8KU_{\mathrm{p}}(t)}}{\omega_{\mathrm{streak}}} \cos(\theta)\cos(\omega_{\mathrm{streak}}t) - \\ &\frac{U_{\mathrm{p}}(t)}{2\omega_{\mathrm{streak}}} \sin(2\omega_{\mathrm{streak}}t). \end{aligned} \tag{2.76}$$

By only considering electrons with a momentum parallel to the polarisation of the streaking field ($\theta = 0$), and only considering the dominant terms in the expression this can be reduced to

$$\phi(t) = \frac{\sqrt{8KU_{\mathrm{p}}(t)}}{\omega_{\mathrm{streak}}} \cos(\omega_{\mathrm{streak}} t), \tag{2.77}$$

which, remembering Equation 2.63, can be inserted into Equation 2.75 by using Equation 2.73. Obtaining

$$I(\rho, \tau) \propto \exp\left(\frac{-a(\omega - \omega_0)^2}{2(a^2 + (\varphi \pm s/2)^2}\right), \tag{2.78}$$

where $a = 1/4\tau^2_{\mathrm{ionising}}$, φ is the linear chirp and s is the streaking speed defined as

$$s = \frac{\partial \delta W}{\partial t} = \pm\sqrt{8U_{\mathrm{p}}(0)\omega_0}\,\omega_{streak}. \tag{2.79}$$

From the above the width of the measured spectrum can be obtained as

$$\sigma_{\mathrm{s}} = \sqrt{\sigma_{\mathrm{ionising}} + \tau_{\mathrm{ionising}}(s^2 \pm 4\varphi s)}. \tag{2.80}$$

Deconvoluting the measured spectra then allows the pulse duration of the measured spectrum, the two deconvolutions being

$$\sigma_{\mathrm{s}_+,\mathrm{s}_-} = \sqrt{\sigma^2_{\mathrm{s}_+,\mathrm{s}_-} - \sigma^2_{\mathrm{ionising}}}, \tag{2.81}$$

with s_+ and s_- referring to the two different signs of the vector potential. For electrons measured on a positive slope of the vector potential A the spectrum is broadened, whereas for those on a negative slope the spectrum is narrowed. This can be seen visually in Figure 2.21. Solving Equations 2.80 and 2.81 for the ionising pulse duration gives

$$\tau_{\mathrm{ionising}} = \frac{1}{\sqrt{2}s}\sqrt{\sigma^2_{\mathrm{s}_+} + \sigma^2_{\mathrm{s}_-}}, \tag{2.82}$$

meaning the linear chirp rate can be retrieved as

$$c = \frac{\sigma^2_{\mathrm{s}_+} - \sigma^2_{\mathrm{s}_-}}{8s\tau^2_{\mathrm{ionising}}}. \tag{2.83}$$

Within this framework, for a linearly chirped ionising XUV pulse, full pulse properties can be retrieved, allowing for full pulse reconstruction in time, spectrum and phase when both σ_{s_+} and σ_{s_-} are measured simultaneously.

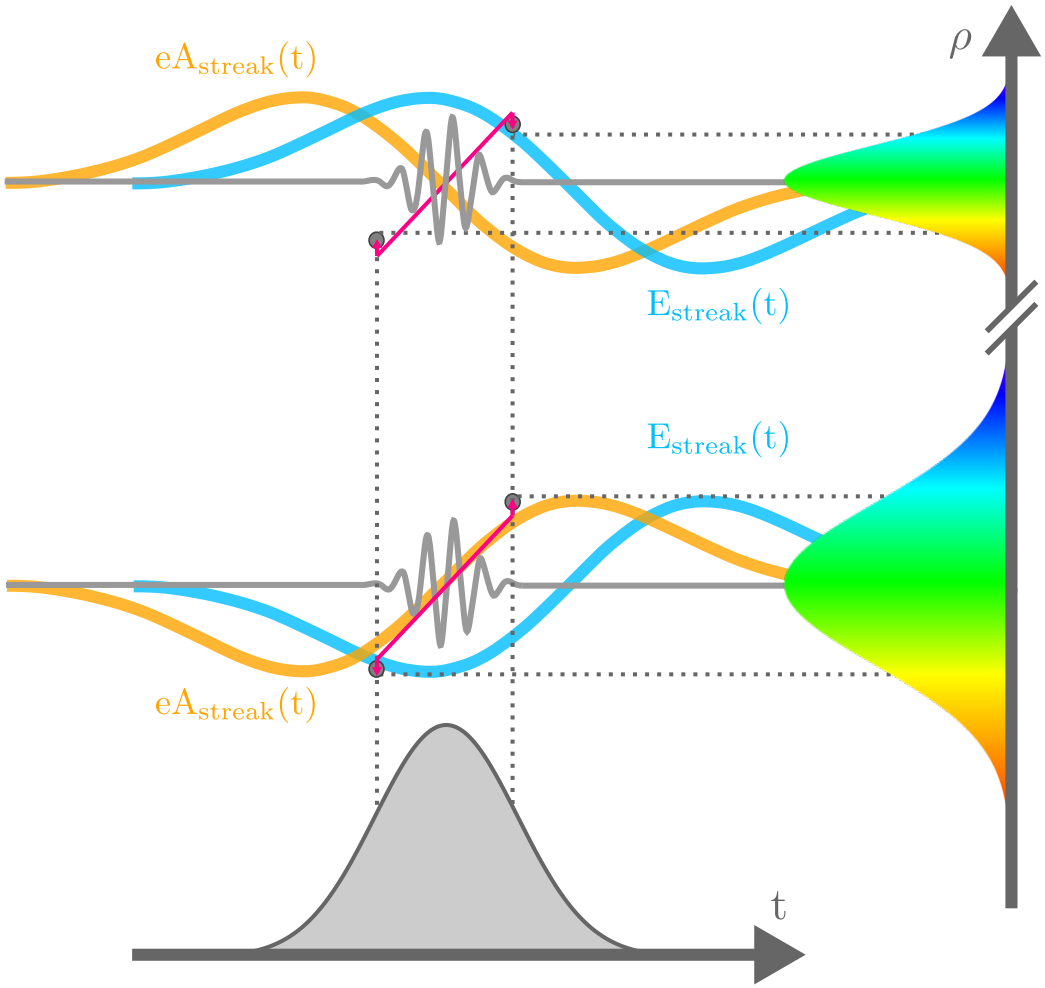

Figure 2.21: Visualisation of narrowing and broadening of the measured electron spectra for a linearly chirped XUV pulse (grey). At the falling edge of the vector potential the electron spectrum is narrowed, since higher energy electrons, which come first are slowed down and electrons with lower energy are accelerated narrowing the spectrum (top). At a rising edge higher-energy electrons coming first are sped up, and lower-energy electrons that come later are slowed down broadening the spectrum (bottom).

Chapter 3

Design

3.1 Overview

In this section the design of the various setups used in this work will be discussed. Specifications of important optical elements and methodologies will be covered. Diagrams of custom setups used are provided. An overview of the experimental setup in schematic chart form can be seen in Figure 3.1. More detailed information on most steps illustrated will be given throughout the chapter.

3.2 Pulse Shaper

As discussed in the introduction, the principle idea of this work is to show the transfer of a typical 4-f line pulse shaper design from transmissive optics to one working under grazing incidence in an all reflective setup, with the eventual aim of enabling operation in the XUV and soft x-ray regimes. The device utilised in this work consists of the principle five 4-f shaper elements, plus an additional two optional focusing mirrors placed at either end of the setup. These are designed to both allow a higher transmission in an XUV operation of the device (but decrease the transmission in the DUV operation). This is discussed further in subsection 3.2.1. As such the outermost focusing mirrors are replaced by plane mirrors for this work. The shaping elements are contained within five modular vacuum chambers, designed such that each chamber contains one of the five primary shaping optics. The vacuum chambers are mounted to a single support frame in order to minimise relative positional change between the optical components due to vibrations. To assist this minimisation the shaper support frame rests on passive damping elements. Each chamber is capable of translating along the beam propagation direction with bellows connecting it to its neighbours, allowing the distance between each optic to be coarsely adjusted to match the

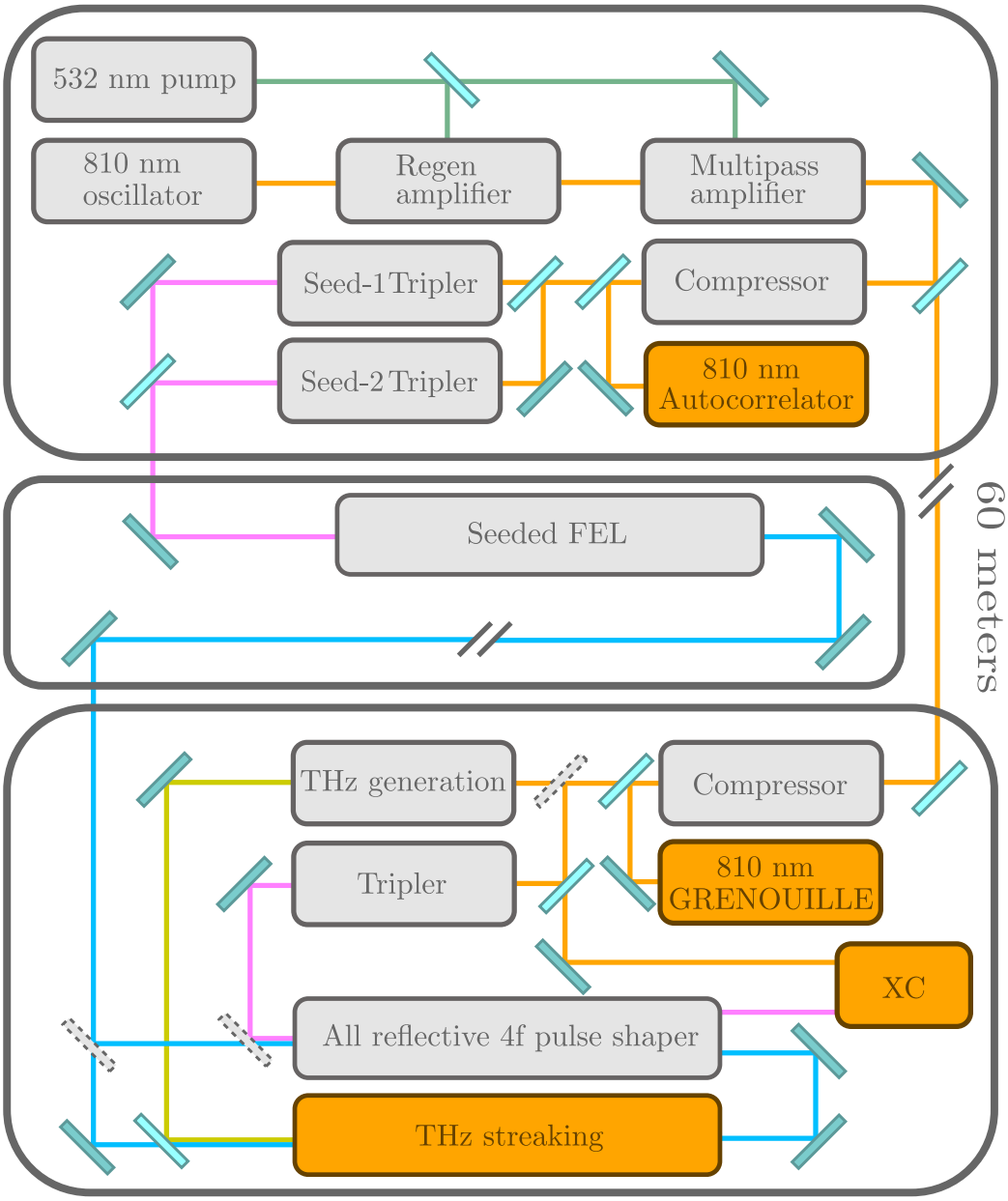

Figure 3.1: Flow chart detailing various steps in the experimental setup. Detailed in each dark grey box are the parts in differing labs or experimental areas. Light grey boxes indicate transformations on beam properties. Orange boxes represent characterisation devices. A 60 m vacuum beam pipe is present between the source generation and the experimental hutch. Differing wavelength lasers are depicted in differing colours. Green: 532 nm. Orange: 810 nm. Violet: 266 nm. Light blue: XUV. Light yellow: THz radiation.

focal length *f*. The device is equipped with Ce:YAG screens to allow for diagnostics and alignment to be performed on the XUV beam during XUV operation. The Ce:YAG screens fluoresce at 530 nm. Magnetically levitated turbopumps are connected to the two largest chambers at the extremities of the device, allowing vacuum conditions to be reached and maintained for the XUV operation. The turbopumps are insulated from the vibrations of the pre-vacuum scroll pump using soft-plastic connection pipes and also reduce vibrations as there is no mechanical connection between the rotor and the vacuum chamber (a difference to normal turbopumps, which contain ball bearings). Within this work only the DUV beam was used, such that no vacuum operation was required. A CAD diagram of the shaping setup can be seen in Figure 3.2. Each optic is equipped with various translation and rotation stages, each with in-vacuum picomotors to minutely control the beam propagation through the device. A summary of the 34 total translations and rotations for each optic in the modular shaper setup can be seen in Figure 3.3. The large number of degrees of freedom enable the necessary fine-tuning of such a complex device, even if that comes at the cost of added complexity during the commissioning. Given the space constraints in the experimental hutch of the X-Seed project the optical layout has been optimised for spectral resolution and overall transmission.

3.2.1 Gratings and Focusing Optics

All focusing mirrors used in the shaper consist of cylindrical polished silicon substrates Pilz-Optics with 0.5 nm **R**oot **M**ean **S**quare (RMS) surface roughness and maximum radius of curvature errors at 1.5%. Each pair of identical mirrors (FM_1/FM_4 and FM_2/FM_3) are cut from the same polished piece of silicon, meaning they have an identical radius of curvature, which was also precisely measured before delivery. This means not only is the curvature very well known, but even more importantly, that it is identical for the mirror pairs. These mirrors give good reflectivity in the DUV range under grazing incidence. The two central focusing mirrors (FM_2 and FM_3) have a focal length of 330 mm, focusing along the direction of dispersion of the beam as it traverses the shaper. The focal length of these two optics define f for the shaper and dictate the required grating dispersion. The two optional outer focusing mirrors (FM_1 and FM_4) have a focal length of 810 mm and focus orthogonal to the direction of dispersion of the beam as it traverses the shaper. The two outer focusing mirrors are designed such that the focus is reached in the Fourier plane. These mirrors reduce the size of the beam footprint on the mask, reducing the phase mask dimensions which in turn relaxes the slope error requirements. Primarily of importance when operating the device in the XUV configuration, these mirrors are replaced by flat UV enhanced aluminium mirrors, which increases overall transmission for the DUV.

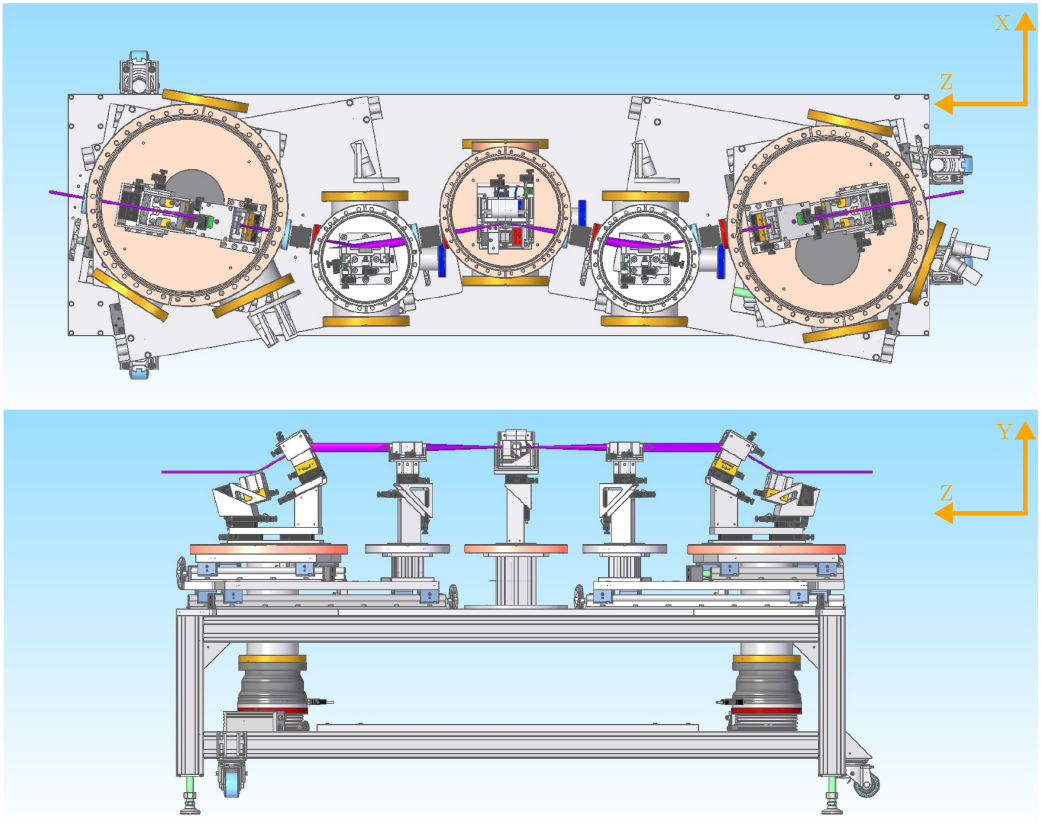

Figure 3.2: Detailed top and side view of the experimental all reflective shaper used in this work. Shown are the optical axes (orange), with the beam travelling from right to left. Visible in grey and yellow on the diagram are the various motors and stages used to align the beam, highlighting the mechanical complexity of the device. A rough idea of how the device focuses the beam can be seen from the size of the purple beam in the figure. Figure adapted from [45].

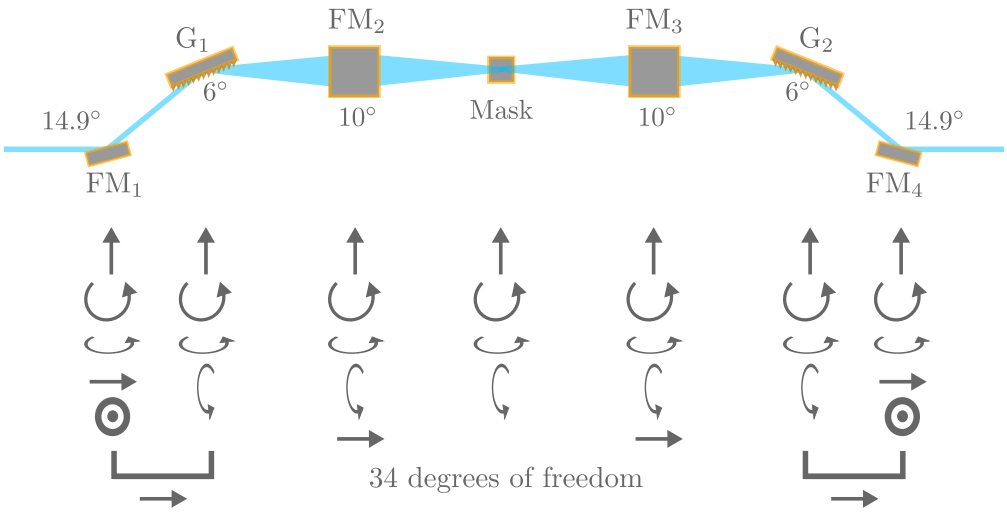

Figure 3.3: Simplified diagram of the experimental setup. Key components, i.e. the gratings G_1 and G_2, focusing mirrors FM_1, FM_2, FM_3 and FM_4, and the shaping mask are highlighted. The specific grazing angles of incidence in the setup are 14.9° for FM_1 and FM_4, 6° for G_1 and G_2, 10° for FM_2, FM_3 and the mask. The surface normals of FM_2 and FM_3 are pointing into the plane of this figure. Degrees of motorised freedom available for each optic in the shaper setup are shown below each optic.

As the slope error is a larger consideration the shorter the wavelength, it does not effect the DUV operation significantly. For operation in the XUV spectral range an identical set of focusing mirrors with a 45 nm-thick amorphous carbon coating can be installed (coating provided by Incoatec). The carbon coating provides optimal reflectivity in the XUV. Reflectivity curves for XUV wavelengths at the grazing angles used in this work can be found in [45]. Due to the shallow angles of incidence for each optic the beam footprint is large. As such the input beam diameter is limited by the current geometry and optic dimensions to a maximum of 5 mm, however more ideally to 2 mm. For potential use down to a central soft x-ray wavelength of 4 nm the focusing optics can be coated with nickel to provide optimal reflectivity[1]. However high mirror transmission is not achievable below an operational wavelength of 15 nm at 14.8° grazing incidence. Shallower angles and different coatings are necessary in order to achieve good transmission. Nickel reflectivity is high down to about 3 nm at 5°. This would require new focusing optics in place of FM_2 and FM_3, each with a focal length of 990 mm increasing the total length of the shaper to 4.7 m. This is possible due to the modular nature of the device, and is currently limited only by lab space.

[1] In the so-called water window.

The gratings are produced by Richardson Gratings and are made of BK-7 glass coated with aluminium and a layer of magnesium fluoride to protect from oxidisation. They are blazed at 10.4°. With 300 l/mm and a dispersion of 3.8 nm/mm they are optimised to diffract the majority of the DUV light into the first order. By observing the grating equation

$$d(\sin\theta_i - \sin\theta_d) = m\lambda, \tag{3.1}$$

it is clear that the n$^{\text{th}}$ harmonic of the seed laser will diffract with maximum transmission at the n$^{\text{th}}$ order due to this grating blaze angle, i.e. propagating the same beam path. This also gives the possibility of multi-color experiments using the shaper at seeded FEL facilities.

3.2.2 Lamellar Mirror Mask

To perform initial pulse shaping experiments with the device, a lamellar mirror amplitude mask was chosen. It consists of a polished silicon substrate, micromachined to provide 5 mm long reflective strips of 100 µm width separated by 150 µm gaps. Placed in the Fourier plane of the shaper this would generate a double pulse in time domain by introducing a periodic amplitude modulation along the spectrum in the Fourier plane. A diagram of the lamellar mirror mask and its effect upon the spectrum can be seen in Figure 3.4. The relative CEP between the two generated pulses depends on which parts of the spectrum are modulated. The time delay between these two pulses is dependent on the size of the structures in the modulated spectrum, which is in turn dependent on the

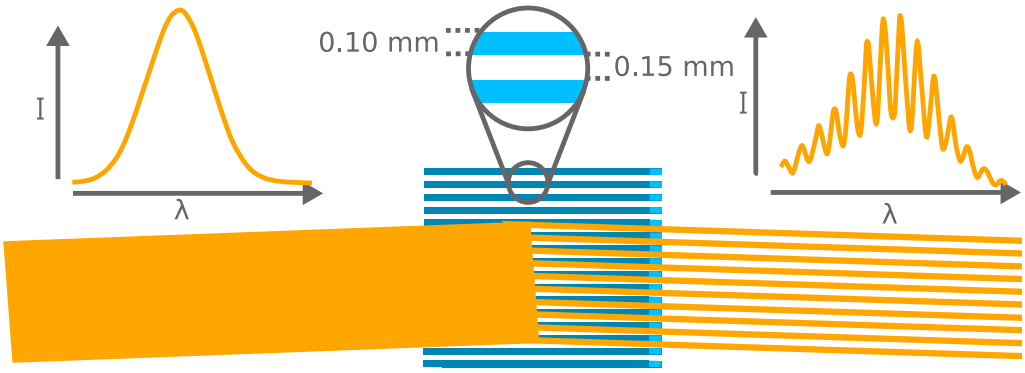

Figure 3.4: Diagram of the lamellar mirror mask. With a spectrally dispersed beam (spectrum top left) incident on it. Shown is how selected parts of the beam reflect, modulating the spectra (spectrum top right). The spectra are both measured data, fitted with a spline.

dispersion/mm of the beam as it reaches the lamellar mask, and the size of the reflective stripes. Within the current configuration, the theoretical time delay between the pulses should be on the order of 600 fs [45]. To control the relative spectral phase between the two pulses, the lamellar mirror can be shifted transversely in the dispersion direction, changing the modulation on the spectrum. The lamellar mirror mask was machined using a diamond rotary saw by the group of Prof. Kip from the Helmut Schmidt University in Hamburg.

The mechanical polishing procedure used to produce surfaces with roughness below the nm level creates a permanent bend in the 1 mm-thick substrate of the top mirror. Surface flatness and roughness for each optic needs to be below $\lambda/8$ for interferometric phase experiments to be performed. Due to the current limits in optics quality and actuator accuracy pulse shaping below 4 nm isn't possible with current technology. The current version of the lamellar mirror has sufficient surface flatness to measure fringe-resolved interferometric autocorrelation

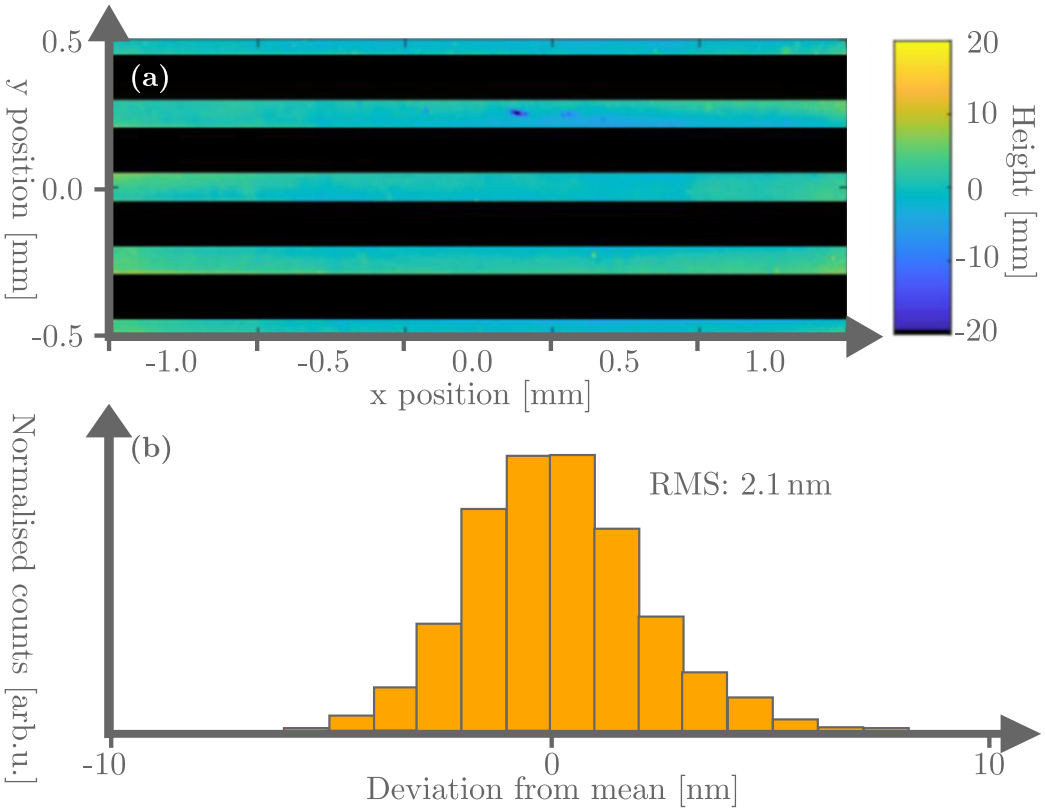

Figure 3.5: Height map of the lamellar mirror mask used in the shaper. In (a) one can see the colour coded height-map retrieved by white light interferometry. In (b) one can see the histogram of deviations from the mean height of the lamellar mirror. The RMS deviation from a flat surface is 2.1 nm.

traces down to a central wavelength of 4.5 nm [104]. A white light interferometry setup can be used to monitor the position of the reflective elements of the shaping mask on a shot-to-shot basis in real time, if required. A white light scan of the mask was performed to check the surface flatness and the results of this can be seen in Figure 3.5. For details of the white light interferometry setup used see [105].

Complex Shaping Masks

Due to the modular nature of the shaper, and the ease of alternating optics, the lamellar mirror mask can easily be replaced by some other shaping mask. Such as the **M**icro **M**achined **D**eformable **M**irror (MMDM) or **M**icro **M**irror **A**rray (MMA) masks. An example of two complex mask designs can be seen in Figure 3.6. These two designs are capable of shaping the phase of an input pulse at will. For initial characterisation of the pulse shaper a flat silicon mirror was utilised, performing no active change on the spectral amplitude or phase.

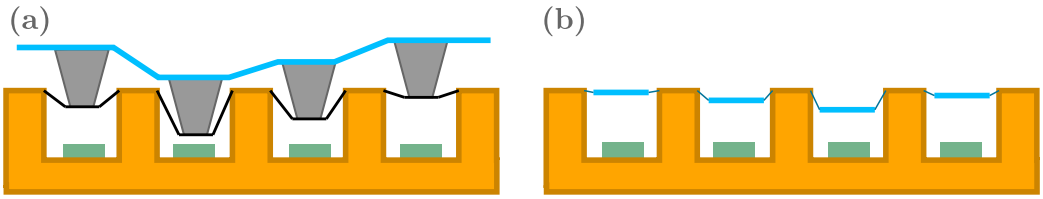

Figure 3.6: Two example complex mask designs. (a) is a micro machined deformable mirror. Where a mirror surface (blue) is deformed by electrostatic actuators (green) allowing custom mirror surfaces to perform easy phase shaping on an input pulse. (b) is a micro mirror array where individual mirror pixels are controlled by electrostatic actuators.

Table 3.1: Shaper performance parameters

Parameter	Value
Input beam diameter (Δx_{in})	5 mm
Spatial frequency separation (Δx_0)	1.93 µm
Grating period (d)	3.33 µm
α	9.25×10^{-18} ms
Spectral resolution ($\delta\omega$)	216 GHz
Temporal shaping window (T)	12.8 ps
Shaping speed (v)	0.39 mm/ps

3.2.3 Spectral Resolution

The pulse shaping capabilities of the shaper are determined by the spectral dispersion of the gratings, the focal length of $FM_{2/3}$ and the subsequent spectral width of the "monochromatic" lines in the Fourier plane. The dispersion determines how many pixels, or reflective stripes, of the mask are illuminated within the spectral bandwidth of the pulse and can therefore be used for shaping. This spectral line width determines the separation between frequency components, whose spectral phases can be tailored independently. The focus width of the monochromatic beams is affected by the following:

- Gaussian waist size ω_{y}. The Gaussian waist size is dependent on focal length f and wavelength λ.
- Geometrical optics effects blurring the image in the dispersion direction.
- Surface quality of the optical elements. Poor surface flatness, slope error, surface roughness and damage on optics can decrease spectral resolution.
- Spatial chirp[2] and pulse-front tilt[3] in the DUV.

Focus size and separation of spectrally resolved lines (as compared to the smallest element in the phase mask) is the limiting factor of the spectral resolution of the pulse shaper. Some properties of the shaper using a DUV beam can be seen in Table 3.1. These properties are retrieved using Equations 2.50-2.56.

[2]Spatial chirp is where a beam has its different spectral components separated in space transverse to the direction of propagation.

[3]Pulse-front tilt is where the arrival time of an ultrashort pulse varies across the beam profile.

3.2.4 Spatial Diagnostics for Beam Positioning

Eight vacuum compatible screens are present in the pulse shaper setup. One before each optical element and one at the exit. The screens are covered with unpolished 0.2 mm-thick Ce:YAG crystals, which fluoresce around 540/550 nm. These are attached to vacuum compatible manual translation stages to allow insertion and removal of the screens during operation. To detect fluorescence or scattered light at low intensities acA1920-40gm CCD cameras from Basler with CFFL F1.4 f25 mm lenses from Edmund optics are used. The specifications of cameras and lenses are listed in Table 3.2. This camera and lens combination allows for a spatial resolution of $\sim$ 0.23-0.92 mm, which gives sufficiently high alignment precision and detects fluorescence even at rather low photon numbers. These diagnostics are critical for operation under vacuum conditions when working with XUV beams. [4]

Table 3.2: Shaper diagnostic specifications

Component	Property	Specification
ACEa 1920g48	Pixel size	5.86 × 5.86 µm
	Resolution	1920 × 1200
	Maximum FPS	42
	Quantum efficiency	70%
	Dark noise	$6.7e^{-}$
CFFL F1.4 f25 mm	Focal length	25 mm
	Magnification at 100 mm	0.0025×
	Magnification at 400 mm	0.00625×

3.3 DUV Source

3.3.1 Generation and Properties of 810 nm Pulses

The fundamental 810 nm laser used in this experiment is generated by a mixture of regenerative and multi-pass amplification using **Ti**tanium **Sa**pphire (Ti:Sa) crystals as gain media. An 810 nm mode-locked seed is first generated by a commercial Venteon oscillator. This is positively temporally chirped and sent into a customised HIDRA Ti:Sa amplifier by Coherent. Firstly a regenerative amplifier is pumped by part of a 10 Hz 532 nm pulse generated by a commercial Innolas

[4] For operation under air during commissioning with DUV pulses one can additionally use standard laser alignment cards.

Spitlight 600 laser. This amplified 810 nm pulse is further sent into a Ti:Sa multi-pass amplifier setup, pumped by the remaining part of the 532 nm Innolas beam, traversing four passes through the gain medium before exiting the amplification setup. The repetition rate of the whole setup is limited by the 10 Hz 532 nm pump laser. After amplification the 810 nm has roughly 50 ± 1.5 mJ pulse energy at 10 Hz and a 64 picosecond long pulse duration. The amplified output pulse is then split into two, one part being sent to generate 266 nm photons via frequency up-conversion used for seeding the FLASH FEL and the other to the experimental hutch for use in THz generation and pulse shaping. The latter also makes use of 266 nm pulses generated in the direct vicinity of the pulse shaper setup. Of interest to this work is predominantly the beam that travels to the experimental hutch.

3.3.2 Pulse Compression

After exiting the amplification setup the picosecond 810 nm pulse travels 60 meters through vacuum tubing from the lab where it is generated to the experimental hutch. This beam transport utilises a motorised beam stabilisation setup with a reference 810 nm **C**ontinuous **W**ave (CW) alignment laser, which is polarised orthogonally to the amplified 810 nm pulse, to ensure minimal pointing jitter. After entering the lab, the pulse is sent directly to a polarised grating compressor. Before the compressor is a half wave-plate, allowing the energy of the out-coming compressed pulse to be tuned as required. The compressor utilises a single-grating setup equipped with a retro-reflector on a delay stage. The delay stage allows variation of the path length difference between the bluest and reddest parts of the input pulse spectrum, allowing for variable pulse compression by introducing linear chirp if desired. For use in the pulse shaping setup the 810 nm pulse is compressed near to its Fourier limit of roughly 50 fs. For work with THz streaking it is compressed to 800 fs to prevent laser induced damage in the THz generation crystal (by introducing large linear chirp). The compressor has a maximum efficiency of roughly 25%.

3.3.3 Third-harmonic Generation (THG) at 266 nm

After compression the 810 nm pulse is sent to a third-harmonic up-conversion setup, known as a tripler. The tripler unit used in this work consists of four elements, specifications of which can be seen in Table 3.3. Here the specifics behind third-harmonic generation from a single fundamental field frequency ω using a setup of two nonlinear crystals, one delay plate and one half wave-plate is briefly given (the third-harmonic here being defined as $\omega_3 = 3\,\omega_1$). A representation of this setup using a 810 nm fundamental can be seen in Figure 3.7. All pulses

in the figure are assumed to be spatially overlapped and travelling collinear. The five steps outlined in the figure are

- **Step 1**: the fundamental 810 nm field (orange) with frequency ω_1 is incident on a BBO crystal. Using Type I phase matching it generates a second-harmonic at 400 nm wavelength and with frequency $\omega_2 = 2\omega_1$ (blue), with a polarisation orthogonal to that of the fundamental. The second-harmonic pulse is delayed with respect to the fundamental by a time dt due to the different refractive index of the crystal material for the two frequencies ($n(\omega_1) < n(\omega_2)$).

- **Step 2**: a birefringent delay plate with a refractive index $n(\omega_1) > n(\omega_2)$ for the respective polarisation of the fundamental and second-harmonic is introduced, which compensates for the delay that arose during collinear propagation of the fundamental and second-harmonic through the BBO crystal and makes the fundamental and second-harmonic pulses overlap in time.

- **Step 3**: the second harmonic polarisation is rotated with a half wave-plate to match that of the fundamental.

- **Step 4**: the fundamental and second-harmonic pulses are combined in another BBO crystal to generate the third-harmonic pulses at 266 nm (purple), where $\omega_3 = \omega_1 + \omega_2 = 3\omega_1$.

- **Step 5**: the three output fields emerge delayed with respect to each other because of the different refractive index of the BBO present for each individual frequency, as in step 1.

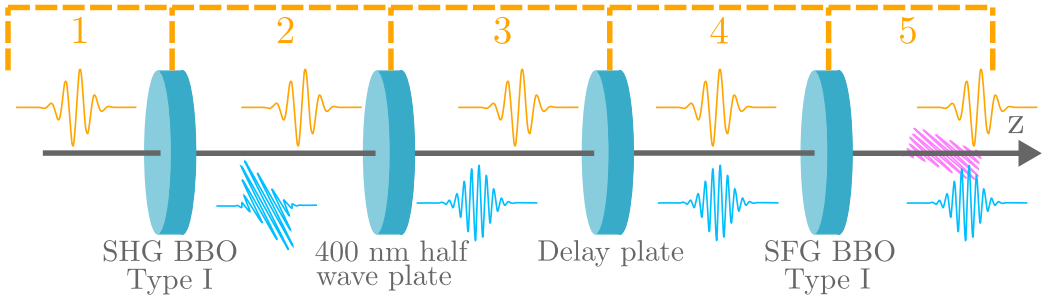

Figure 3.7: Representation of a third-harmonic generation setup using two nonlinear crystals, a delay plate and a half wave-plate. For details see subsection 3.3.3.

Table 3.3: Tripler optic specifications

Tripler component	Thickness [mm]
Type 1 SHG BBO crystal 400-800 nm	0.2
Calcite delay plate	1.7
Zero order wave-plate, λ/2@800+λ@400 nm	1.88
Type 1 SHG BBO crystal 400-800/266 nm	0.05

The two nonlinear BBO crystals utilise type I phase matching, (both input frequencies having the same polarisation). This tripler set is a standard commercial kit bought from EKSMA optics, model number FK-800-050-10. Each optic has a diameter of 10 mm. The thin crystals in the kit are optimised to produce short pulse duration output pulses, as well as maximise phase matching across the bandwidth of the input pulse. This is achieved by having thin crystals, but with the trade-off of lower conversion efficiency. Each optic within the tripler is held within a kinematic rotation mount allowing angle tuning in both ϕ and θ to achieve optimal phase matching and conversion efficiency for each optic in the series[5]. The achieved conversion efficiency from 810 nm to 266 nm was on the order of 4.5%, compared to the 5-6% stated by the company specifications. Thus giving a good, if not optimal, conversion. The maximum achieved energy in the DUV was roughly 150 μJ, this was limited in practicality to 50 μJ due to the risk of optic damage caused by the focused DUV beam in the focal plane of the shaper above 50 μJ input energy[6]. This pulse energy can therefore be seen as a soft energy limit for the shaper in the current configuration, without using optics with higher damage thresholds.

[5]Here ϕ refers to the rotation of the crystal around the direction of propagation of the beam, and θ refers to rotation of the angle between the crystal axis and the beam propagation direction.

[6]Input to the entrance of the shaper.

3.4 XUV Source

In this section the XUV source used for the THz-streaking experiments will be described. Along with typical pulse properties.

3.4.1 Seeded FLASH

The coherent XUV radiation is generated via seeding the FLASH-1 modulators with the 266 nm laser pulses, generated as described in subsection 3.3.3, using a HGHG scheme. FLASH is an XUV and soft x-ray FEL facility located at DESY in Hamburg. FLASH is comprised of a single LINAC (linear accelerator) that accelerates electrons for two SASE FELs, FLASH-1 and FLASH-2 and a seeded FEL project titled X-Seed. FLASH-1 features fixed-gap undulators and provides SASE pulses between 51 nm and 4.2 nm to users in the FLASH-1 experimental hall. FLASH-2 is comprised of variable-gap undulators, allowing its output wavelength to be tuned without changing the electron energy and independently from FLASH-1. FLASH-2 is currently operated as a SASE FEL, providing light between 90 nm and 4 nm for users in the FLASH-2 experimental hall. An HGHG seeding scheme was used to generate the 7^{th} harmonic of the seed laser (38.1 nm). The XUV pulse is sent through a transport beamline to the experimental hutch, where a switching mirror allows the beam to be switched between the THz streaking and the pulse shaping setups at will. The coherent 38.1 nm XUV radiation generated this way has average pulse energies on the order of 35.1 ± 10.4 μJ with a spectral bandwidth of $0.45 \pm 0.15\%$ [106].

3.4.2 Seeded FLASH Properties

While the temporal information of XUV pulses needs to be measured with advanced techniques such as THz streaking, the spectrum of the pulse can be easily retrieved using a simple diffraction grating. As the properties of the XUV pulse are linked to the electron bunch properties it is also possible to extract some information from the XUV pulse from measuring the electron bunch.

Differences between a seeded and SASE FEL spectrum can be seen in Figure 3.8. In Figure 3.8(a) a single-shot SASE XUV (38.1 nm) pulse spectrum is shown. It is apparent that the spectrum is composed of many individual frequency modes, each incoherent from the rest. In Figure 3.8(b) a clean single-spike seeded FEL spectrum can be is displayed. This figure highlights some of the difference in spectral quality between SASE and seeded FEL pulses in terms of longitudinal coherence. Both SASE and seeded FEL radiation have high spatial coherence [107]. By changing the gap of the modulator during operation it is possible to

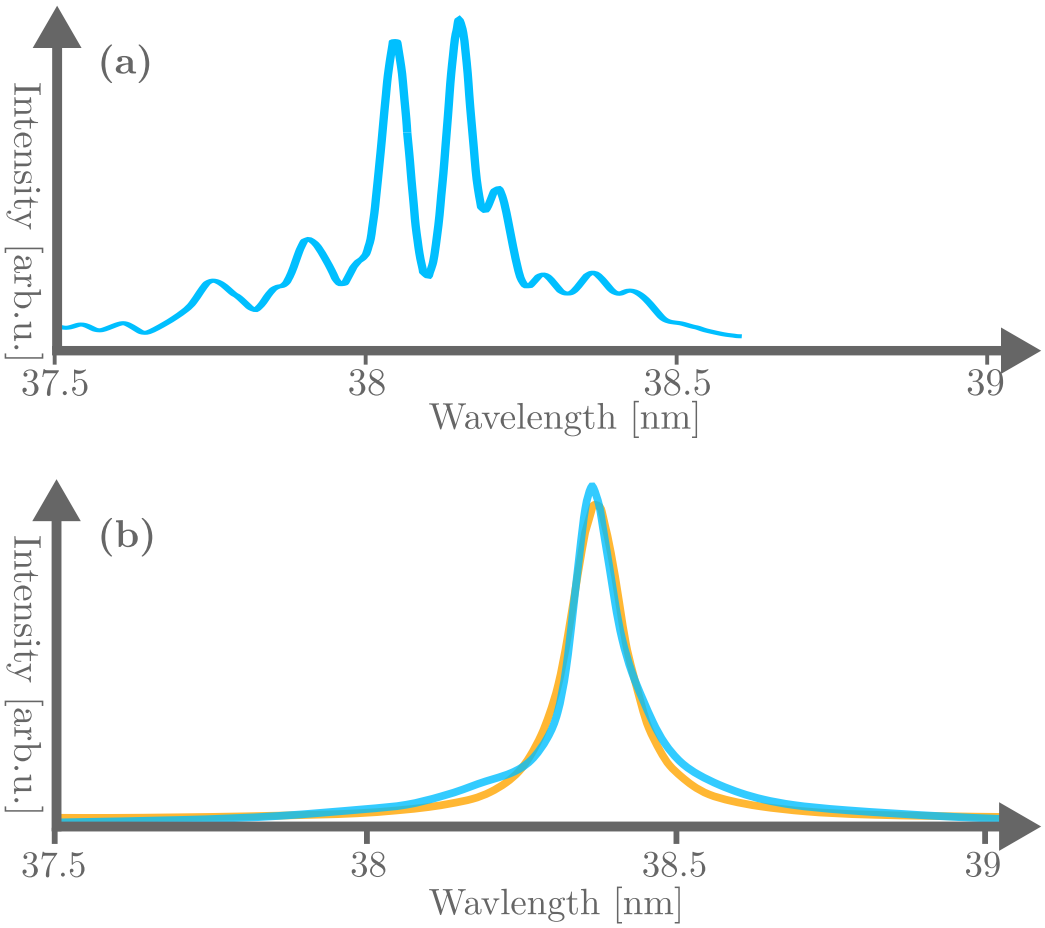

Figure 3.8: (a) SASE FEL spectrum generated at 38.1 nm. Figure adapted from [45]. (b) seeded FLASH HGHG FEL spectra at the 7th harmonic of the seed laser (38.1 nm). The average spectrum (blue) is compared to a Lorentzian fit (orange). Figure adapted from [106]. All intensities are arbitrary.

switch between all harmonics of the DUV seed on-the-fly during seeded FEL operation.

3.4.3 Timing and Synchronisation

The Ti:Sa oscillator, which generates the 810 nm fundamental, is synchronized by a phase-locking loop-control system to the FLASH **M**aster **O**scillator (MO). The MO provides lower harmonics of the fundamental frequency of the accelerating cavity field inside the FLASH accelerators. The fundamental frequency is 1.3 GHz and sub-harmonics generated by the master oscillator are 108 MHz, 81 MHz, 27 MHz and 9 MHz. All frequencies are phase-locked to the fundamental. The Ti:Sa oscillator is locked to the 108 MHz harmonic of the MO by the phase-locking loop. This ensures that the timing of the oscillator is easily mapped to that of the electron bunches in FLASH allowing minimal relative timing jitter.

Synchronisation by Optical Cross-correlation

To keep the optical seed pulse synchronised to the electron pulse in the FEL beamline an **O**ptical **Cross**-**C**orrelator (OXC) is utilised. The OXC generates the SFG signals between the 810 nm Venteon oscillator pulse and a 1550 nm pulse generated from the MO. Looking at the signal strength of the SFG gives insight into the relative temporal overlap of the two pulses, and therefore the synchronisation between them. More details about the OXC used can be found in [108].

3.5 Optical Characterisation Methods

Ultrashort pulse characterisation is not trivial. Measuring femtosecond pulse durations is beyond the scope of modern electronics such as oscilloscopes, and further beyond any conventional mechanical timing technique. To that extent ultrafast pulses are typically measured against themselves, or similar pulses, taking advantage of nonlinear interactions to produce the measurable signal. Two primary methods are used in this work to characterise optical pulses and are described in subsection 3.5.1 and subsection 3.5.2. Other characterisation methods are briefly discussed in subsection 3.5.3.

3.5.1 Cross-correlation FROG

To characterise the DUV pulse used in this work a custom cross-correlation FROG (X-FROG) was utilised. For the beam geometry of the cross-correlator there are two primary choices available.

- Collinear geometry.
- Non-collinear geometry.

The cross-correlator used to characterise the DUV pulse was designed in a non-collinear geometry. The difference between them being that in the collinear setup, the pump and idler beams, in this case the 266 nm and 810 nm, are incident on a nonlinear medium spatially overlapped, and with the direction of propagation of being exactly the same. The result is that the signal pulse (405 nm) generated will also propagate in the same direction, creating three overlapping pulses as output. Whereas in the non-collinear setup the pump and idler beams are still spatially overlapped within the nonlinear medium, but with an angle between the directions of propagation, such that the incoming and out coming pump and signal beams are spatially separated. Due to this slight angle between the beams, and due to conservation of k-vectors in the incoming photons, the resultant idler beam is emitted at a third angle, spatially separated from both the pump and signal beams.

Both collinear and non-collinear geometries have benefits and limitations. In a non-collinear setup the clear benefit is that the resultant beams are all spatially separated. This allows easier detection of the idler when both spatial and temporal overlap have been achieved. This provides intrinsic background reduction as compared to the collinear method, where all three beams are spatially overlapped and either need to be further separated (using filters or dichroic mirrors) or be measured taking the background into account.

However for alignment purposes in a collinear setup it is far easier to achieve spatial overlap, especially for small beam sizes. In a non-collinear setup the phase matching is also more of a concern, with desired phase matching conditions drifting further from the optimum value as the angle between the beams increases. This results in non-collinear setups typically having a small, order of a few degrees, difference in direction of propagation of the two input beams.

It is also possible in the non-collinear setup to measure the temporal pulse duration of the pulse from the width of the signal measured. This scheme sketched in Figure 3.9 will be used for optimisation of the tripler output discussed in section subsection 4.3.1.

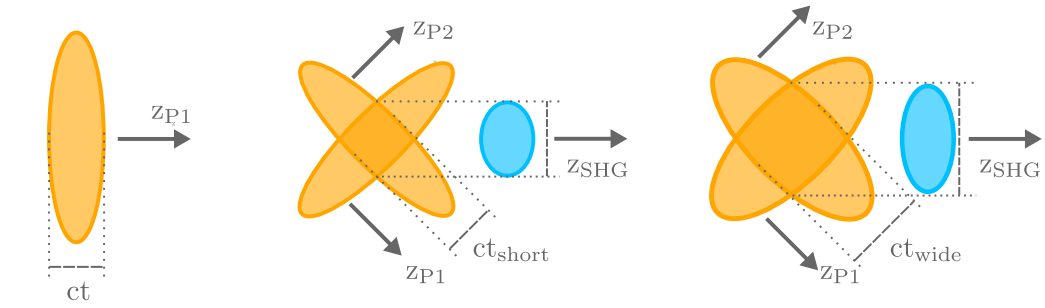

Figure 3.9: Representation of a single-shot autocorrelator. First, a single pulse travelling along z is shown, with physical length ct where t is the pulse duration. Then, two short overlapping identical pulses are shown travelling in differing directions z_{P1} and z_{P2}, with the overlap region generating the second-harmonic autocorrelation signal. The sketch repeated in the final image for two longer pulses. It is visible in the diagram how the physical size of the pulse profile of the generated signal changes as the pulses become temporally longer, i.e. how beam profile size can be linked to pulse duration in a single shot autocorrelator.

It follows that the output idler (810 nm), pump (266 nm) and signal (405 nm) pulses would be spatially separated. It has the benefit of significantly reducing the noise in the recorded 405 nm signal as a function delay between pump and reference (gate) pulses.[7]. The layout of the cross-correlator was developed by the designer of the pulse shaper, Leslie Lazzarino, together with Bastian Manschwetus and Xeumei Cheng from the DESY laser group (FS-LA). It was then updated and further developed to an X-FROG by the author of this thesis.

A schematic representation of the cross-correlator can be seen in Figure 3.10. It is designed such that the DUV, and NIR fundamental enter the device in parallel, then split using a 266/810 nm **R**eflective/**T**ransmissive (R/T) dichroic mirror[8] such that each input wavelength can be individually aligned and sent to the DFG BBO. The NIR path contains a motorised delay stage with a 2.5 cm travel range topped with a retro-reflector, allowing a 5 cm optical path (length) difference scan (166 picoseconds temporal scan range). The actuator used is the TRA25CC from Newport, connected to a SMC100CC control box also by Newport. The actuator allows a 0.2 µm step size, which paired with the retro-reflector allows steps of 0.4 µm (or 1.3 fs assuming the refractive index of air as unity). The DUV path has a manual 2.5 cm translation stage topped with a retro-reflector, allowing manual

[7]Which is useful due to the low DUV transmission of the shaper mapping to low conversion efficiency in the cross-correlator DFG.

[8]Here the dichroic mirror reflects the 266 nm pulse and transmits the 810 nm pulse.

adjustment to be easily performed if needed. The NIR and DUV beams are incident on the DFG BBO at a small angle of 3 degrees between them, such that the 405 nm signal would be generated to the side of the DUV away from the NIR. The 405 nm pulse spectrum is then recorded by a spectrometer. In the course of the experiment, spectra are measured as a function of the relative delay between the NIR and DUV, and as such produces a spectrogram. The spectrometer consists of a blazed 400 nm grating set to diffract the first order into a CCD camera. The

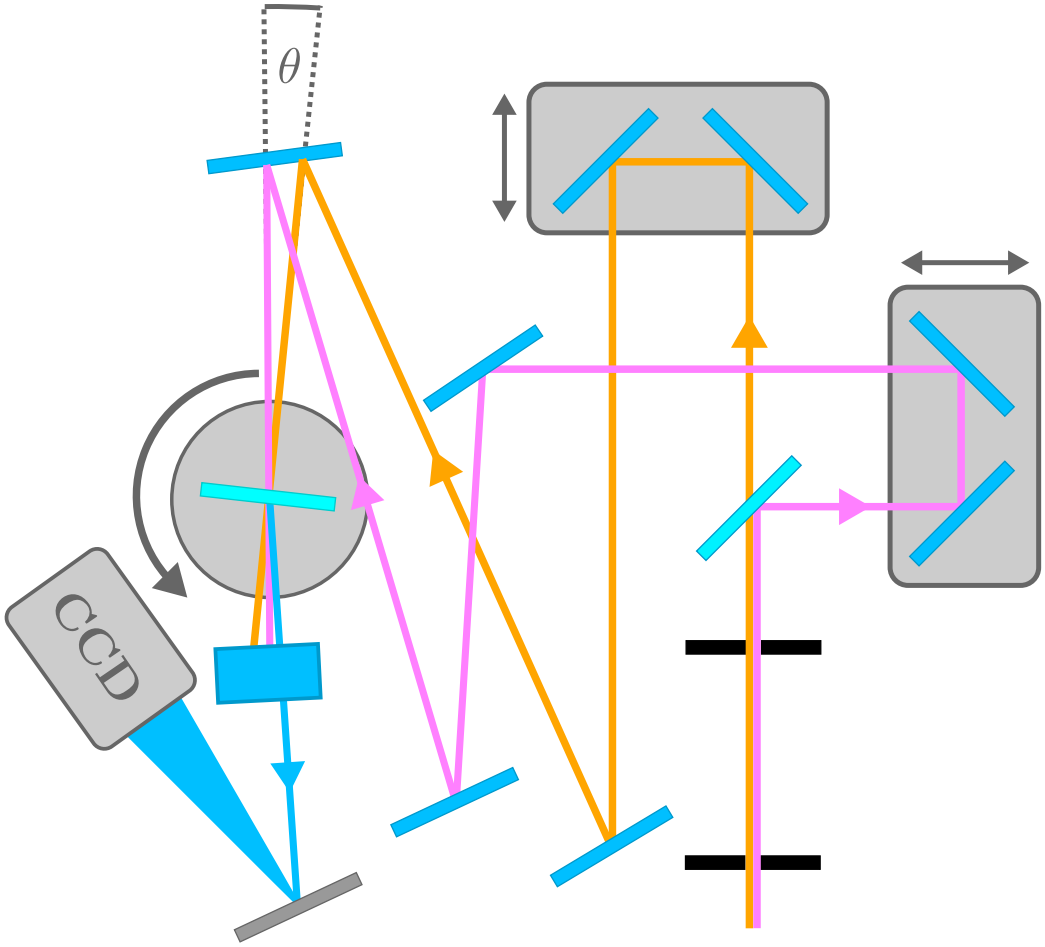

Figure 3.10: X-FROG experimental setup. The 810 nm (NIR - orange) and 266 nm (DUV - purple) come in collinear, are separated by a dichroic mirror and sent along variable motorised beam paths to overlap in a nonlinear BBO crystal mounted on a rotation stage. The beams overlap at a small angle θ such that the 405 nm (blue) signal generated propagates at an angle to the pump and idler beams, allowing the signal to be spatially separated from the incoming beams. The 405 nm signal is passed through a 400 nm filter before hitting a grating and finally the spectrum is recorded on a CCD.

camera was calibrated using a strong 405 nm signal measured by a commercial spectrometer as a reference. The blazed DUV grating and CCD combination was developed as the commercial spectrometer available was not able to measure the weak 405 nm signals generated by the DUV/NIR DFG after the shaper.

To retrieve the DUV pulse duration from the measured 400 nm pulse duration, the following relation is used.

$$\Delta t_{\mathrm{DUV}} = \sqrt{\Delta t_{400}^2 - \Delta t_{810}^2}, \tag{3.2}$$

where Δt_{DUV}, Δt_{405} and Δt_{810} are the DUV, 405 nm and 810 nm pulse durations, respectively. The pulses here are assumed to be Gaussian in time.

3.5.2 GRENOUILLE

The **GR**ating **E**liminated **N**o-nonsense **O**bservation of **U**ltrafast **I**ncident **L**aser **L**ight **E**-fields or GRENOUILLE also developed by Trebino *et al.* [109] works under the same fundamental principle as the FROG method, however with a simplified optical setup. The GRENOUILLE provides full pulse information, as well as information on the spatial chirp and pulse front tilt, making it in some ways a superior alternative to a FROG. The GRENOUILLE however relies on SHG so is unsuited for short wavelength measurements. A diagram of the basics of a GRENOUILLE setup can be seen in Figure 3.11. The GRENOUILLE works by using a Fresnel biprism to split one incoming pulse into two and refracting them such that they combine within a thick BBO which further acts to spatially disperse the spectrum of the SHG generated. This is then recorded and calibrated with a camera. The camera calibration is needed to figure out the wavelength spacing per pixel, which is dependent on the geometry of the setup. Including the camera this setup can be built with four optics.

3.5.3 Alternative Pulse Characterisation Methods

Other notable pulse characterisation methods that are not used in this work but that are worth mentioning for completeness are **S**pectral **P**hase **I**nterferometry for **D**irect **E**lectric-field **R**econstruction (SPIDER) [110] and **T**ransient **G**rating FROG (TG-FROG) [111].

SPIDER

In a SPIDER setup the pulse is first split into two identical copies, which are delayed so that there is no temporal overlap between them. Another part of the input pulse is then strongly temporally broadened by chirping it. The long

chirped pulse and the two delayed input pulses are then combined in a nonlinear crystal, where SFG occurs. The two signal pulses overlap with different temporal portions of the chirped pulse so that there is also a spectral shear between the two up-converted pulses, as the chirped pulse has a time-frequency dependence. The frequency spectrum of the SFG signal reveals the temporally resolved group delay. From the group delay, it is easy to retrieve the frequency-dependent spectral phase, so that complete pulse characterisation can be achieved. Compared to FROG retrieval algorithms, the algorithm used to retrieve pulse information in a SPIDER setup works much faster. Thus, it allows for application in fast feedback systems if using the pulse characterisation for pulse shape control.

TG-FROG

TG-FROG utilises a third-order nonlinear interaction to measure pulse properties. It requires an input pulse to be split into three. Two of the pulses are spatially and temporally overlapped in a nonlinear medium, producing a refractive-index grating. The third pulse is variably delayed and overlapped in the nonlinear medium and is diffracted by the induced grating to produce the signal pulse. The advantage of this setup is that only one input frequency is required, because the signal pulse is of the same frequency as the input. This method is highly sensitive and background free. However the alignment of this device can be difficult due to the three beam setup. It also relies on a third-order nonlinear interaction meaning a large input intensity is optimal.

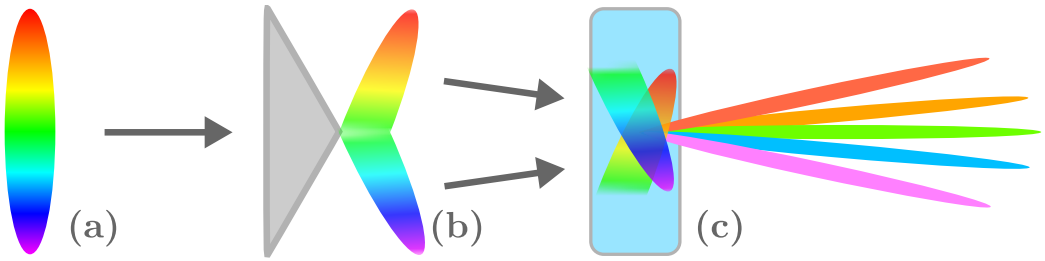

Figure 3.11: Diagram of a GRENOUILLE setup. In (*a*) a single input pulse comes in, the pulse is represented as having spatial chirp to illustrate how spatial chirp can be measured. In (*b*) the pulse is split into two and refracted such that the split pair combines inside the nonlinear crystal (*c*). The thick crystal acts as a nonlinear medium, generating SHG from the pulse-pair and also acts as a spectrometer, spectrally dispersing the SHG to be measured by a camera. Visible in (*c*) is the differing overlapping frequencies indicating that a spatially chirped beam will generate a differing signal to that of a non spatially chirped beam.

3.6 XUV Characterisation - THz Streaking

The THz streaking setup utilises part of the 810 nm fundamental compressed to 800 fs to generate THz radiation at 0.5 ± 0.1 THz. A maximum THz field strength of 80 ± 10 kV/cm in the focus could be achieved by means of optical rectification in a nonlinear Lithium-Niobate crystal ($LiNbO_3$) using 1.5 mJ of the fundamental pump pulse. The beam profile of the fundamental pulse is cylindrical. It is firstly reduced in size using a spherical and a then a cylindrical Galileo telescope (ratios 1:4 and 1:2) before passing the grating, which induces pulse front tilt. After the LiNbO3-crystal a gold coated parabolic mirror (f = 150 mm) is used to collimate the THz pulse. The THz transport beamline consists of gold and silver coated mirrors and the path length is minimised to 0.6 m to reduce absorption via air. A plastic lens (Zeonex 480R, f = 75 mm) with a 2 mm diameter hole focuses the THz pulse into the THz streaking chamber with a spot size of 1.5 mm and 2.2 mm (FWHM). The THz pulse has a duration of 1200 fs and a pulse energy of 0.42 µJ. Considering energy losses due to Fresnel reflection, THz absorption by water in air and clipping in the vacuum entrance window, the conversion efficiency is roughly 0.05%. The THz streaking chamber is under high vacuum and connected to the FLASH beamline. The chamber contains three ToF spectrometers, a gas jet and an alignment crystal. One of the ToFs is used to record σ_{s_+} and one to record σ_{s_-}, the third ToF is used to measured the unstreaked XUV spectrum outside of the interaction region[9]. The remaining part of the 810 nm fundamental is used to generate a 266 nm pulse (via the same method described in subsection 3.3.3 and using the setup detailed there) which seeds the FLASH FEL to produce a seeded XUV pulse.

After generation, the THz and seeded XUV pulses are overlapped both spatially and temporally on the gas target. This is done by delaying the NIR pulse with a temporal delay line before the THz has been generated. The target is ionised by the XUV pulse creating photoelectrons, which are subsequently streaked by the THz pulse. The streaked photoelectrons are measured by one or more of the three ToFs providing detailed information on the temporal structure of the XUV pulse as discussed in section 2.8. Ideally more than one ToF is used, so as to be able to retrieve spectral phase (chirp) information of the pulse by measuring σ_{s_+} and σ_{s_-} simultaneously. A diagram of the overall setup, including the FEL can be seen in Figure 3.12.

[9] See section 2.8 and subsection 4.7.1 for more details.

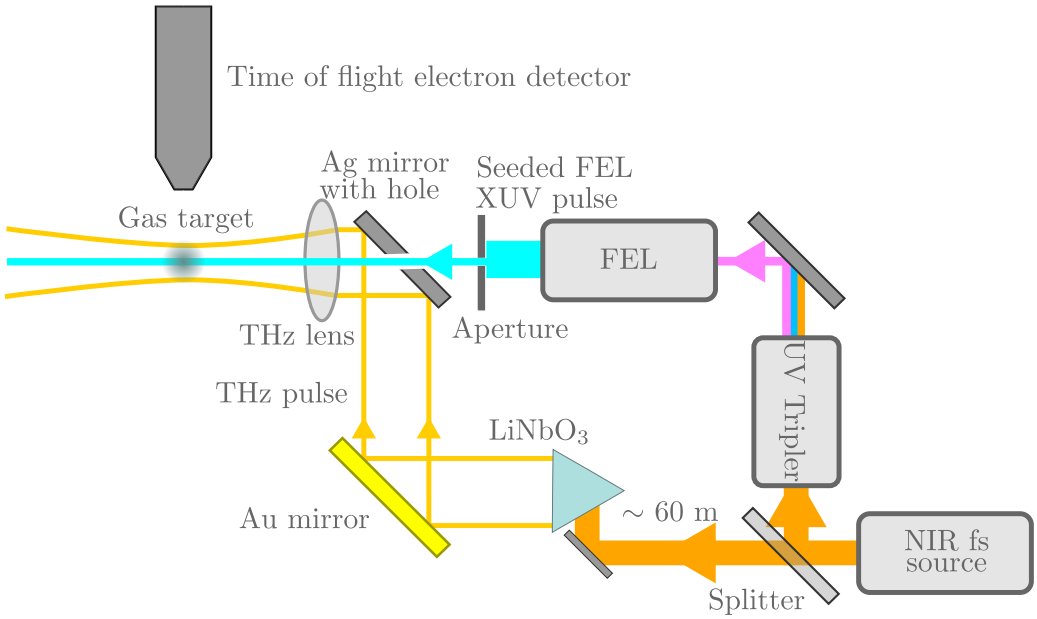

Figure 3.12: THz setup in the experimental hutch connected to FLASH. The 810 nm pulse is used to both seed the FEL and to generate the THz radiation. This provides stable relative timing between the two. The THz and seeded FEL beam are focused onto a gas target, releasing electrons, which are then detected by the ToF spectrometer. Figure adapted from [112].

THz streaking, when used with multiple time-of-flight detectors, can directly resolve the spectral chirp of an XUV pulse, including the sign. This setup is also capable of measuring the pulse in a parasitic way both before or behind an experiment, allowing simultaneous experiments and pulse diagnostics to be performed on a shot-to-shot basis. The THz streaking field and seeded FEL pulse are also intrinsically synchronised because they start from the same seed source. From [112] the jitter between THz and seeded FEL pulse has been measured at 17 fs rms, this jitter being attributed to length fluctuations along the two about 60 m long optical beam paths of the seed pulse and the NIR pulse generating the THz radiation.

Electron time-of-flight spectrometers (ToFs) measure the time-of-flight of photoelectrons and Auger electrons. In a field-free ToF spectrometer the arrival time of electrons at the detector is equal to L/v, where v represents the velocity of the electrons and L the distance between the interaction region and the detector. For a fixed length L the electrons velocity and kinetic energy can be derived from the measured arrival time as the time-of-flight of these electrons is dependent on momentum. By taking into account the ionisation potential of

the target atom the photon energy is derived. Time zero of the ToF spectra is given by the detection of stray light originating from the ionising photon source. For a more detailed discussion on ToF operation and requirements, the reader is referred to literature [113–116].

Chapter 4

Results

4.1 Overview

In this section the results of pulse shaping at 266 nm will be explored. Firstly the conversion and generation of the 266 nm DUV from the 810 nm fundamental will be discussed, which will be followed by transmission efficiencies through the shaper for different phase mask configurations. The central topic is the full characterisation of a phase-locked DUV double pulse generated in the all-reflective shaping setup working under grazing incidence. The resulting waveforms for different shaping mask configurations will be shown, with spectrogram, spectrum and phase for each case presented. Open-loop relative-phase control of the DUV pulse pair with fixed temporal separation will be discussed in detail. The second part focuses on the generation and characterisation of the DUV pulses used for seeding the FEL FLASH. The spectrum of the XUV pulse (7^{th} harmonic) generated from 266 nm seeding will be shown. THz streaking used to retrieve the temporal pulse properties of this harmonic was performed and the results are given. Initial experiments towards pulse shaping of the seeded XUV via chirping the DUV seed will be discussed and results shown. This type of "a-priori" pulse shaping by manipulation of the long-wavelength seed time-frequency spectrum has been pioneered at FERMI [117].

4.2 Characterisation of the 810 nm Fundamental

The compressed 810 nm beam going into the tripler has a beam diameter of 5 mm, covering the central two thirds of the BBO crystal diameter, so as to allow maximum THG conversion efficiency within the active area while avoiding clipping. The output DUV beam is then sent through an iris, to allow only a 3 mm perfectly circular beam profile propagating into the shaper. This gives the upper bound of the beam size of XUV sources attached to the shaper, as well as allowing easy observation of deformation induced by the optics as the beam propagates through the shaper. When measuring the output DUV pulse properties the entire 5 mm beam is let through the shaper to avoid effects due to clipping via the iris. The pulse properties of the 810 nm fundamental were measured using a commercial GRENOUILLE from SWAMP optics, model number 8-50-USB. The pulse duration was measured at 50 ± 5 fs and bandwidth at 20 ± 2.8 nm with a retrieved FROG G-Error of 0.1421 and cross checked by using the cross-correlator described in subsection 3.5.1 as an autocorrelator. This was done by replacing the 266/800 nm R/T dichroic mirror with a 50:50 800 nm beamsplitter and replacing the DFG BBO (cut at 44.3°) with a SHG BBO (cut at 29.2°). The 405 nm SFG signal pulse duration was then measured by temporally scanning one delay line of the correlator and the pulse duration of the 810 nm retrieved by calculating the following equation

$$\tau_{405}^2 = 2\tau_{810}^2, \tag{4.1}$$

with τ_{405} as the pulse duration of the 405 nm signal and τ_{810} as that of the fundamental 810 nm. Retrieved GRENOUILLE spectrograms, spectra and phase can be seen in Figure 4.1, retrieved using the inbuilt software included with the device.

From Figure 4.1 it is clear that the pulse has some cubic phase, observable in the phase in Figure 4.1(c) and in the presence of a small temporal pre- and post-pulse seen in Figure 4.1(b), meaning the pulse is not perfectly compressed. However within the center of the spectrum the phase is relatively flat. Cubic phase is introduced by the grating compressor [118]. The cubic phase only affects the outer parts of the spectrum as shown in Figure 4.1(b). The temporal phase seems to be relatively quadratic, as apparent in Figure 4.1(b). As such the 810 nm is not ideal, but still sufficiently short and intense for the work performed.

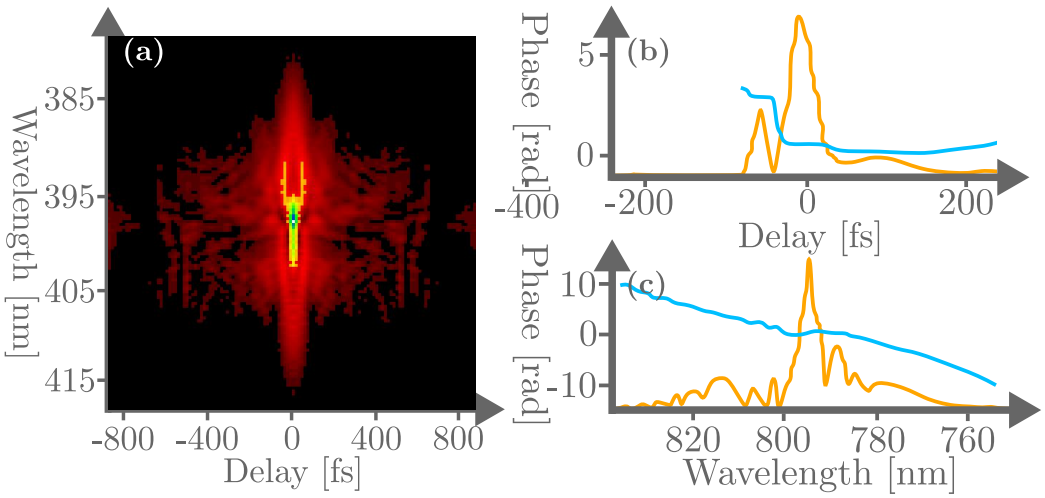

Figure 4.1: Retrieved spectrogram (a), temporal structure (orange) and phase (blue) (b) and spectral structure (orange) and phase (blue) (c) for the 810 nm fundamental pulse obtained from the commercial FROG software that comes packaged with the 8-50-USB GRENOUILLE from Swamp Optics. The intensities in orange are arbitrary and linear and need no scale.

4.3 Third Harmonic Generation

Optics for THG

To convert from the 810 nm fundamental to the 266 nm used in the shaper a commercial tripler kit from EKSMA Optics was utilised. Type 1 phase matching was employed for both the 810-405 nm and 810/405-266 nm conversion processes. The kit specifications are listed in Table 4.1. The tripler was optimised by first optimising second harmonic (405 nm) conversion efficiency using only the first BBO. Afterwards the remaining optics were installed and optimised for DUV conversion efficiency.

Table 4.1: Tripler optic specifications.

Tripler component	Thickness [mm]
Type 1 SHG BBO crystal 400-800 nm	0.2
Calcite delay plate	1.7
Zero-order wave-plate, λ/2@800+λ@400 nm	1.88
Type 1 SHG BBO crystal 400-800/266 nm	0.05

Before frequency up-conversion the 810 nm was compressed from a few picoseconds down to 50 fs using the grating compressor outlined in subsection 3.3.2. The efficiency of this conversion was a maximum of 25%, giving a maximum compressed pulse energy of 7.5 mJ from the 30 mJ input. The achieved conversion from the fundamental (810 nm) to the third-harmonic (266 nm) was on the order of 4%, giving up to 200 µJ of DUV light. However, only 50 µJ of the DUV was used at most, because larger pulse energies caused damage to the shaping mask due to large peak intensities caused by tight focusing in the FP of the shaper. The energies of both the fundamental and DUV pulses were measured using high energy pyroelectric sensors from Ophir Optics, model PE50-DIF-C, along with a Vega power meter by the same company. For low energies the PE10-C sensor from Ophir was used due to increased sensitivity.

4.3.1 DUV Pulse Optimisation

To enable the highest resolution between tailored temporal structures generated by modulating the DUV spectrum, the DUV pulse needed to be as short in time as possible. To that end the 810 nm compressor was utilised to attempt to pre-chirp the 810 nm pulse entering the tripler so as to see any effect on the DUV output pulse duration. The results of the chirp scan can be seen in Figure 4.2.

The results here were measured using the relation of the beam profile size of the 405 nm signal to pulse duration. Using the non-colinear cross correlator setup the width of the 405 nm signal was measured at each step of the compressor delay position. Then by using the known 810 nm pulse and the measured signal profile width, a relative pulse duration scale for the 266 nm was able to be retrieved. At this point no absolute value for the pulse duration of the 266 nm was obtained, but the applied procedure served the primary goal of optimisation. The quantitative analysis is performed by means of FWHM Gaussian fits compared to the GRENOUILLE retrieved 810 nm pulse duration, as discussed in subsection 3.5.1 and diagrammatically shown in Figure 3.9. The benefit here is that it allows data to be taken quickly and with relative ease with no complicated temporal scanning or calibration needed. From these measurements shown in Figure 4.2(a) and (b) it is apparent that the shortest DUV pulse is generated when the 810 nm is also temporally shortest.

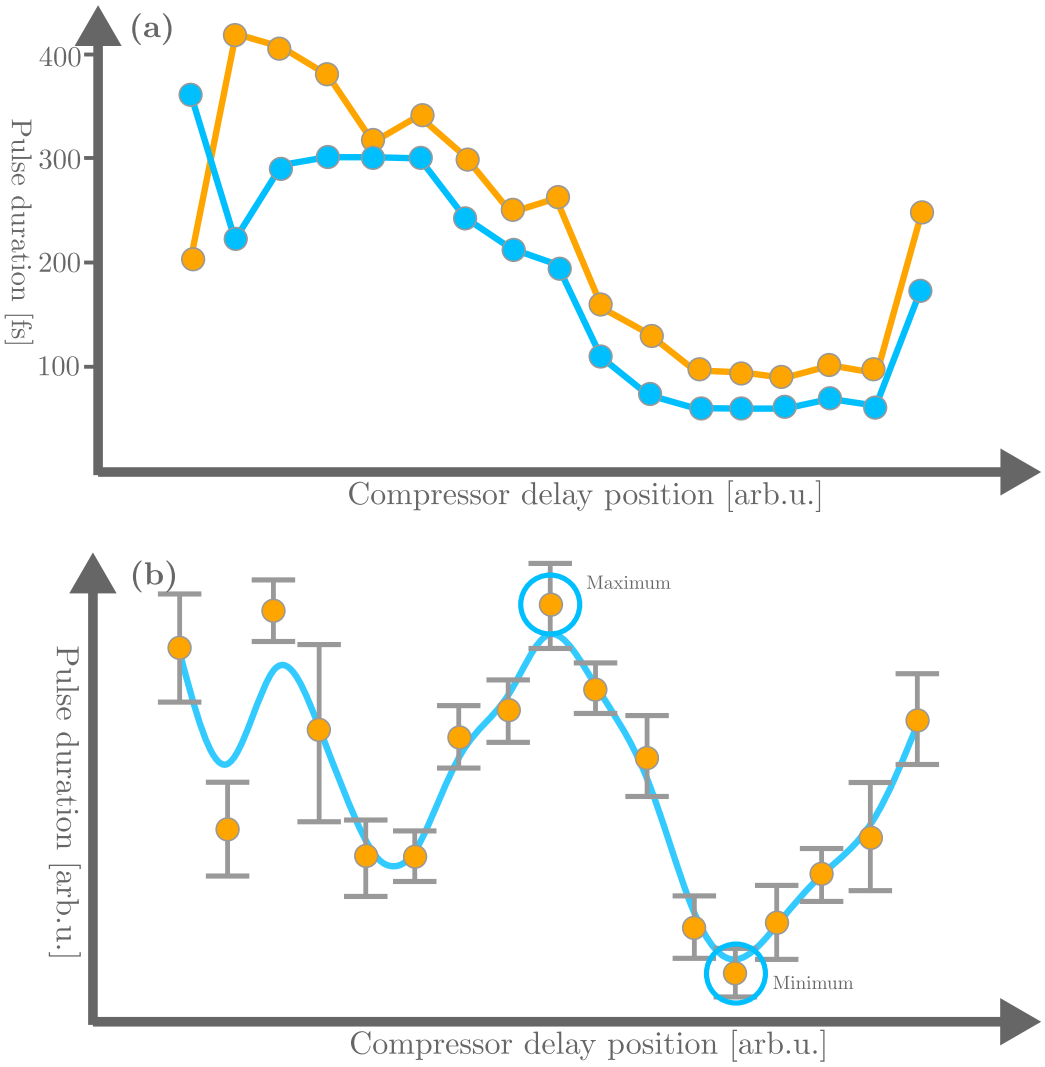

Figure 4.2: (a) 810 nm pulse duration as measured by the GRENOUILLE for various positions of the linear delay stage in the compressor. In orange is the temporal FWHM pulse duration as measured from the retrieved spectrogram, in blue is the autocorrelation FWHM pulse duration. (b) the 266 nm pulse duration as measured via cross-correlation with the 810 nm at the same compressor positions as (a). The methodology is discussed in the text. In the graph the shortest DUV pulse duration is roughly a factor of 4 shorter than that of the longest DUV pulse duration measured (maximum and minimum points labeled on graph in blue circles.)

4.3.2 Spatial Chirp and Pulse-front Tilt

To account for potential pulse-front tilt the spatial chirp of the DUV pulse generated from the tripler was measured. From equation 19 in [119] it is apparent that spatial chirp and pulse front tilt are linked, so by characterising the spatial chirp of the pulse one is able to ascertain if there is also pulse front-tilt present. The equation reads

$$p = p_{\mathrm{AD}} + p_{\mathrm{SC+TC}}, \tag{4.2}$$

where p is the pulse front tilt, p_{AD} the angular dispersion of the pulse and $p_{\mathrm{SC+TC}}$ is the spatial and temporal chirp[12]. The measured pulse front tilt of the 810 nm by the commercial GRENOUILLE is shown in Figure 4.3 for different settings of the pulse compressor. The minimum pulse front tilt appears to be at the same position as the shortest temporal 266 nm pulse duration identified in Figure 4.2(b). The pulse front tilt here measured for the minimum DUV pulse duration is roughly 2 fs/mm, which over a 3 mm beam diameter is roughly 6 fs. This value is small and would not negatively influence any of the shaping capabilities of the pulse shaper.

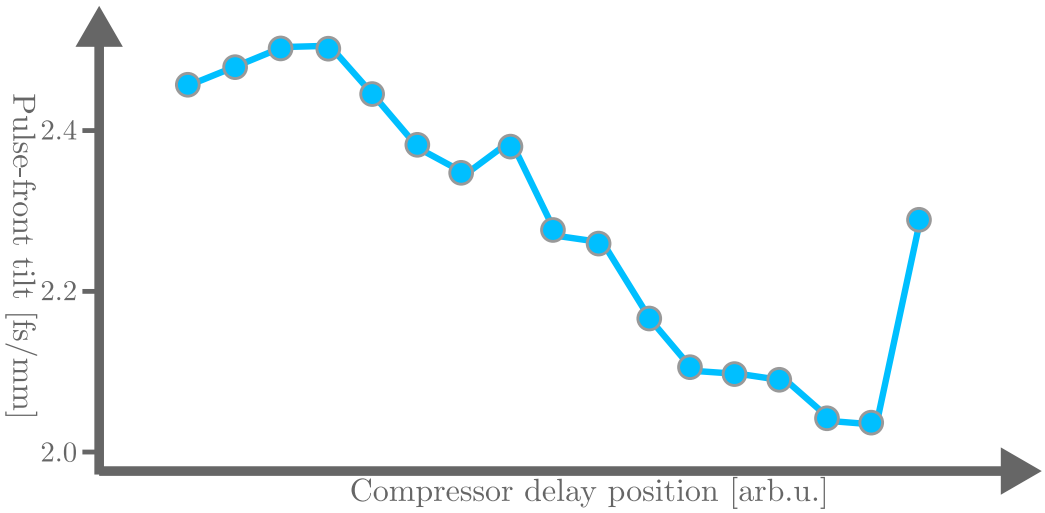

Figure 4.3: 810 nm pulse front tilt after the compressor. Measured using a GRENOUILLE. With the same compressor scale as that in Figure 4.2.

[1]The angular dispersion is defined as the difference in the angles of deviation of two outer colours of the spectrum of the pulse, with units of radians/mm.

[2]The spatial chirp is where different frequency components are separated in space transverse to the propagation direction of the pulse, the units are nm/mm.

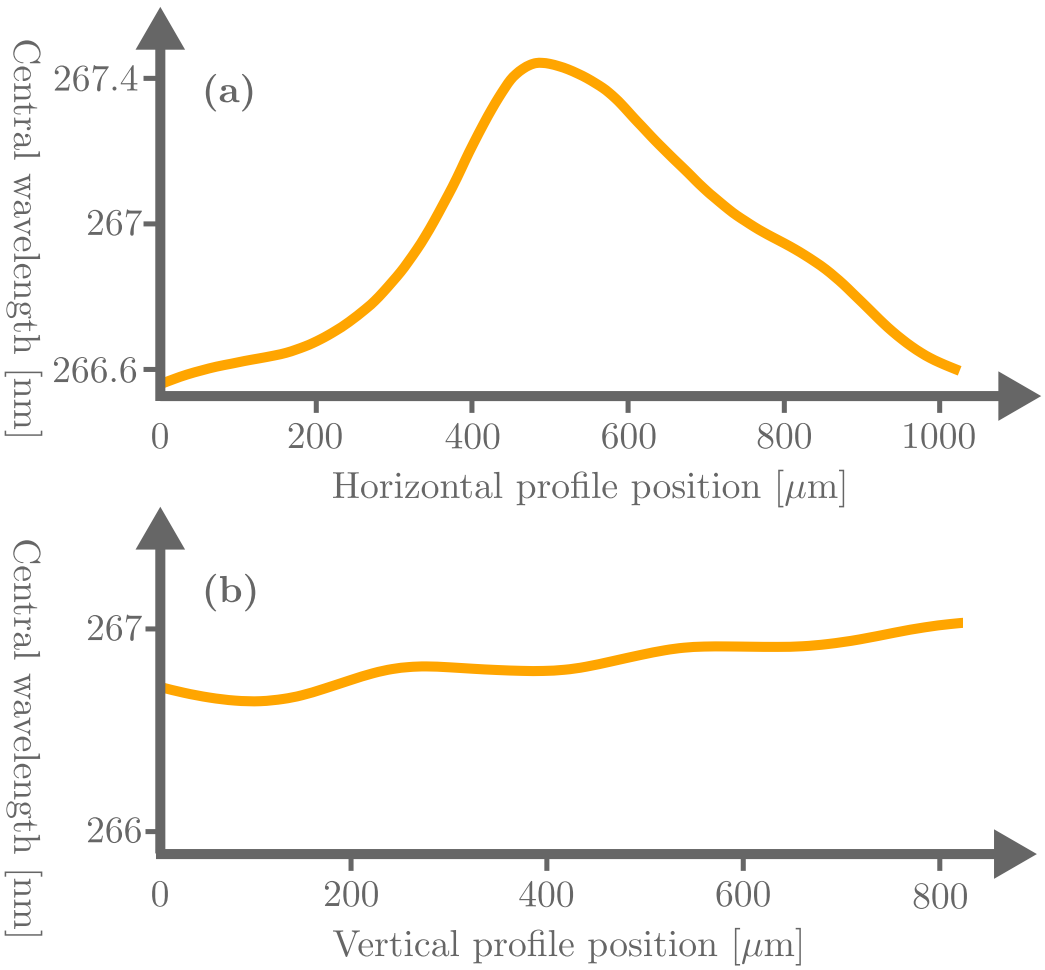

Figure 4.4: Spatial chirp of the DUV after the tripler. In (a) the horizontal profile is recorded and in (b) the vertical profile. It is apparent there is little linear spatial chirp in the vertical direction and some quadratic chirp present in the horizontal.

To measure the spatial chirp an iris, a fiber spectrometer and a translation stage were employed. The iris cuts all but a small section of the spatial beam profile allowing the fiber spectrometer to measure only a small isolated spatial section of the profile. The spectra from each section can be compared this way to see if the spectrum changes across the beam profile. The iris connected to the fiber input was translated both horizontally and vertically across the middle of the beam profile. The center-of-mass wavelength measured[3] for each position was analysed. The result is shown in Figure 4.4 for horizontal and vertical translations. These measurements compliment each other as from Equation 4.2 it is clear that the pulse front tilt and spatial chirp are linked and typically both are present simultaneously.

4.4 Transmission Efficiency

The transmission efficiency of the shaper in the DUV spectral range is 0.26% with the lamellar mirror and 0.61% with a plane mirror installed, respectively. The efficiency is counted as the ratio of the pulse energy measured at the entrance of the device as compared to that at the output. Losses are caused by the mirrors and gratings placed in-between. The relative efficiency per optic can be seen in Table 4.2 and the cumulative transmission over the shaper is given in Table 4.3 for both a flat mirror and the lamellar mirror mask. It is important to first characterise the shaper setup using a flat mirror leaving the time-frequency spectrum of the pulse unchanged. It allows observation of what effect the shaper optics may have on an input pulse when no active shaping has been performed. Ideally, a perfectly aligned device in 4f geometry acts as a zero-dispersion compressor and therefore will induce no changes to the pulse.

Table 4.2: Transmission efficiencies of shaper optics in the DUV.

Shaper optic	Transmission efficiency [%]
FM_1/FM_4	50
FM_2/FM_3	87.5
G_1/G_2	20
Plane mirror	34
Lamellar mirror	80
Total transmission with plane mirror	0.61
Total transmission with lamellar mirror	0.26

[3]Retrieved by a Gaussian fit.

Table 4.3: Cumulative transmission efficiency of shaper optics in the DUV.

Shaper optic	Cumulative transmission efficiency [%]
FM_1	50
G_1	10
FM_2	8.8
Plane mirror/Lamellar mirror	7/3
FM_3	6.1/2.6
G_2	1.2/0.5
FM_4	0.61/0.26

4.5 DUV Pulse Shaping

To completely characterise the shaper performance, both the input and output pulse properties were measured and compared for different settings. Ideally a 4-f pulse shaper will produce no chirping or other transformations when a plane mirror is placed in the Fourier plane. Thus, this setting served as a reference and was studied in detail in the beginning before the more complex periodic amplitude mask (lamellar mirror) was inserted.

4.5.1 Periodic Spectral Amplitude Modulation

The lamellar mirror mask performs a periodic amplitude modulation on the DUV spectrum in the FP of the shaper. To understand the process mathematically we follow Wollenhaupt *et al.* 2006 [120]. Starting with an unmodulated electric field $E^+(t) = [E^-(t)]^*$ we get

$$E^+(t) = \varepsilon^+_{\text{in}}(t)e^{i\omega_0 t}, \tag{4.3}$$

where ω_0 is the carrier frequency and $\varepsilon^+_{\text{in}}(t)$ is the complex electric field envelope. In the frequency domain (remembering the Fourier transform from Equation 4.3) we can define a phase function

$$\varphi(\omega) = A\sin[(\omega - \omega_{\text{ref}})T + \phi], \tag{4.4}$$

where A is the amplitude of the phase modulation function, T is the frequency of the sinusoidal modulation and ϕ is an absolute phase offset. This term modulates the spectrum $\tilde{E}^+_{\text{in}}(\omega)$ so that

$$\tilde{E}^+_{\text{out}}(\omega) = \tilde{E}^+_{\text{in}}(\omega)e^{iA\sin[(\omega-\omega_{\text{ref}})T+\phi]}. \tag{4.5}$$

Then using the Jacobi-Anger identity

$$e^{iA\sin(a)} = \sum_{n=-\infty}^{\infty} J_{\mathrm{n}}(A)e^{ina}, \tag{4.6}$$

where J_n is a Bessel function of the first kind and order n and a is a dummy variable. By defining $\Delta\omega_{\mathrm{mod}} = \omega_0 - \omega_{\mathrm{ref}}$, where ω_{ref} is the reference frequency of the phase modulation function, we can rewrite Equation 4.5 as

$$E^{+}_{\mathrm{out}} = e^{i\omega_0 t} \sum_{n=-\infty}^{\infty} J_n(A)\varepsilon^{+}_{\mathrm{in}}(t+nt)e^{in(\Delta\omega_{\mathrm{mod}}T+\phi)}. \tag{4.7}$$

From Equation 4.7 it can be seen that a sinusoidal phase modulation in the frequency domain produces a pulse train, with temporal separation between the pulses determined by the parameter T and well-defined relative optical phases. Assuming the duration of the pulses is not so broad as to overlap the temporal separation between them, each generated sub-pulse will be a scaled replica[4] of the initial pulse. The phase difference $\Delta\chi$ between a pre- and post-pulse is determined by $\Delta\chi = \Delta\omega_{\mathrm{mod}}T + \phi$.

4.5.2 Spectrograms, Spectra and Phases

To gather the spectrogram data the X-FROG setup for DUV pulse characterisation was used. The retrieval algorithm applied to the recorded X-FROG data is the basic FROG algorithm discussed in detail in [121, 122]. The reference 810 nm pulse was temporally delayed with respect to the 266 nm pulse. The step size was 4 µm ($\sim$ 13 fs)[5].

In Figure 4.6 the measured and retrieved DUV spectra are compared for each of the three scenarios investigated, i.e. (a) input pulse, (b) unshaped and (c) shaped output pulse. The overall agreement is reasonable. A closer look at the key parameter describing the modulated spectral amplitude of the retrieved shaped pulse, which is the spacing between two neighbouring peaks, gives a separation of 0.449 ± 0.027 nm. This nicely compares to the measured spectral separation of 0.444 ± 0.003 nm. Taking this modulation into account, the theoretical temporal separation between subsequent pulses should be on the order of

[4]Here "scaled replica" means an identical copy of the original pulse, simply with a scaled intensity, usually some fraction of the original.

[5]Due to slight misalignment of the retro-reflector used to scan the path length difference a small pointing shift of the 810 nm beam. Which considering the XC geometry resulted in a linear 0.044 nm shift per step on the spectrometer CCD. This was accounted for in the data analysis and X-FROG calibration, respectively.

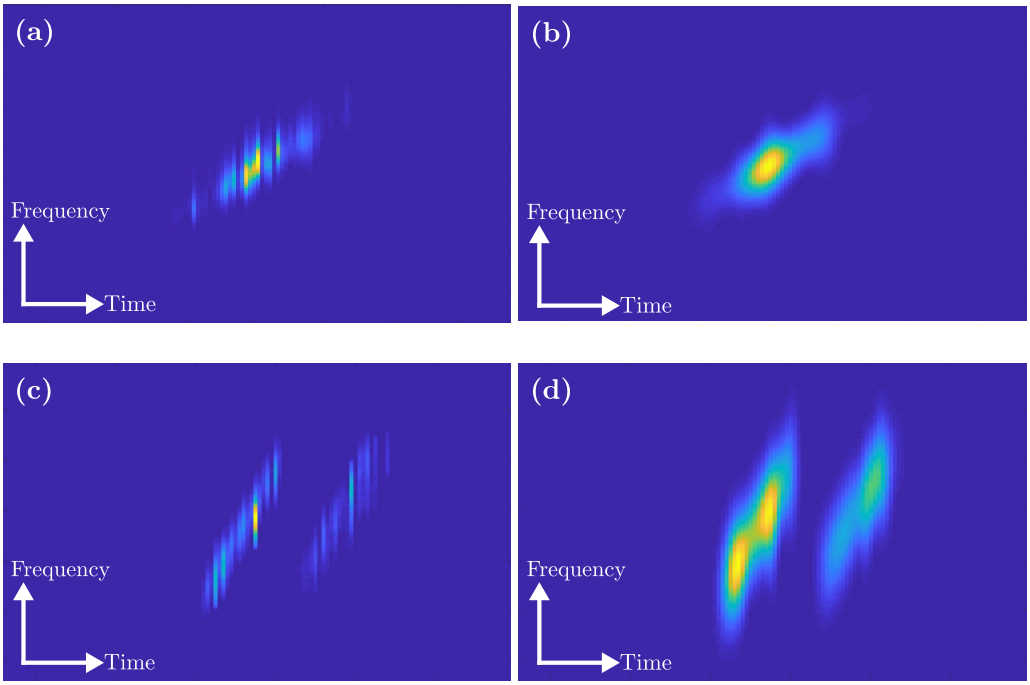

Figure 4.5: Measured raw spectrograms (a), (c) before the shaper and after the shaper, respectively. Retrieved spectrograms (b), (d) before the shaper and after the shaper, respectively, with amplitude shaping using the basic FROG retrieval algorithm [121, 122] recorded using the X-FROG technique. The uncalibrated pixel-by-pixel data are shown. The data shown in (a) is of the UV pulse as measured before the shaper. The data shown in (c) is of the UV pulse as measured after the shaper with spectral amplitude modulation. Each time-step is the result of 200 averaged shots of the 405 nm signal.

600 ± 36 fs, which is in good agreement with the measured value of 630 ± 24 fs [44].

In Figure 4.7(a-f) the retrieved spectrograms, spectra and phases are displayed for the DUV pulse for the three different experimental scenarios. The unshaped pulse characterised in front of the shaper setup is shown in Figure 4.7(a) for the spectrogram with a FROG G-Error of 0.025 and Figure 4.7(b) for the spectra and phase. The femtosecond pulse after the shaper with no active amplitude transformation performed, i.e. with a plane mirror positioned in the Fourier plane is shown in Figure 4.7(c) for the spectrogram with a FROG G-Error of 0.027 and Figure 4.7(d) for the spectra and phase. The effect of the lamellar mirror amplitude mask performing the shaping transformation is demonstrated in Figure 4.7(e) for the spectrogram with a FROG G-Error of 0.027 and Figure 4.7(f) for the spectra and phase. A clear positive linear chirp is observable in all spectrograms (a, c, e), characterised by the retrieved quadratic spectral phases for each pulse (b, d, f). This chirp is inherited from the frequency up-conversion process generating the 266 nm pulses from the 810 nm fundamental. It is apparent from the retrieved data describing the unshaped pulses, that the shaper introduces a little positive chirp. In Figure 4.7(c) and Figure 4.7(d) a double temporal feature is apparent in the pulse, this may stem from an unbalanced grating causing an additional modulation overtone upon the spectral amplitude. This assumption is supported by the appearance of the same structure also in Figure 4.7(e) and 4.7(f) indicating that this structure is independent of the amplitude mask. It is suspected to be due to slight misalignment of the gratings within the shaper, keeping in mind the high sensitivity of the many optics to position and orientation [45]. However, and this is important, the targeted amplitude-shaped 266 nm pulse characterised in Figure 4.7(e) and Figure 4.7(f) shows a clear modulation in the retrieved spectral phase, with the same modulation period as present in the pulse wavelength spectrum. For easy viewing a summary of the FWHM pulse properties of each of the shaped and unshaped pulses can be seen in Table 4.4.

Table 4.4: Temporal and spectral pulse properties

Pulse	Pulse duration [fs]	Bandwidth [nm]
Input pulse (unshaped)	110 ± 13	2.80 ± 0.2
Output pulse (unshaped)	145 ± 3.3	2.74 ± 0.08
Shaped pre-pulse	169 ± 3.0	3.01 ± 0.5
Shaped post-pulse	169 ± 3.0	3.01 ± 0.5

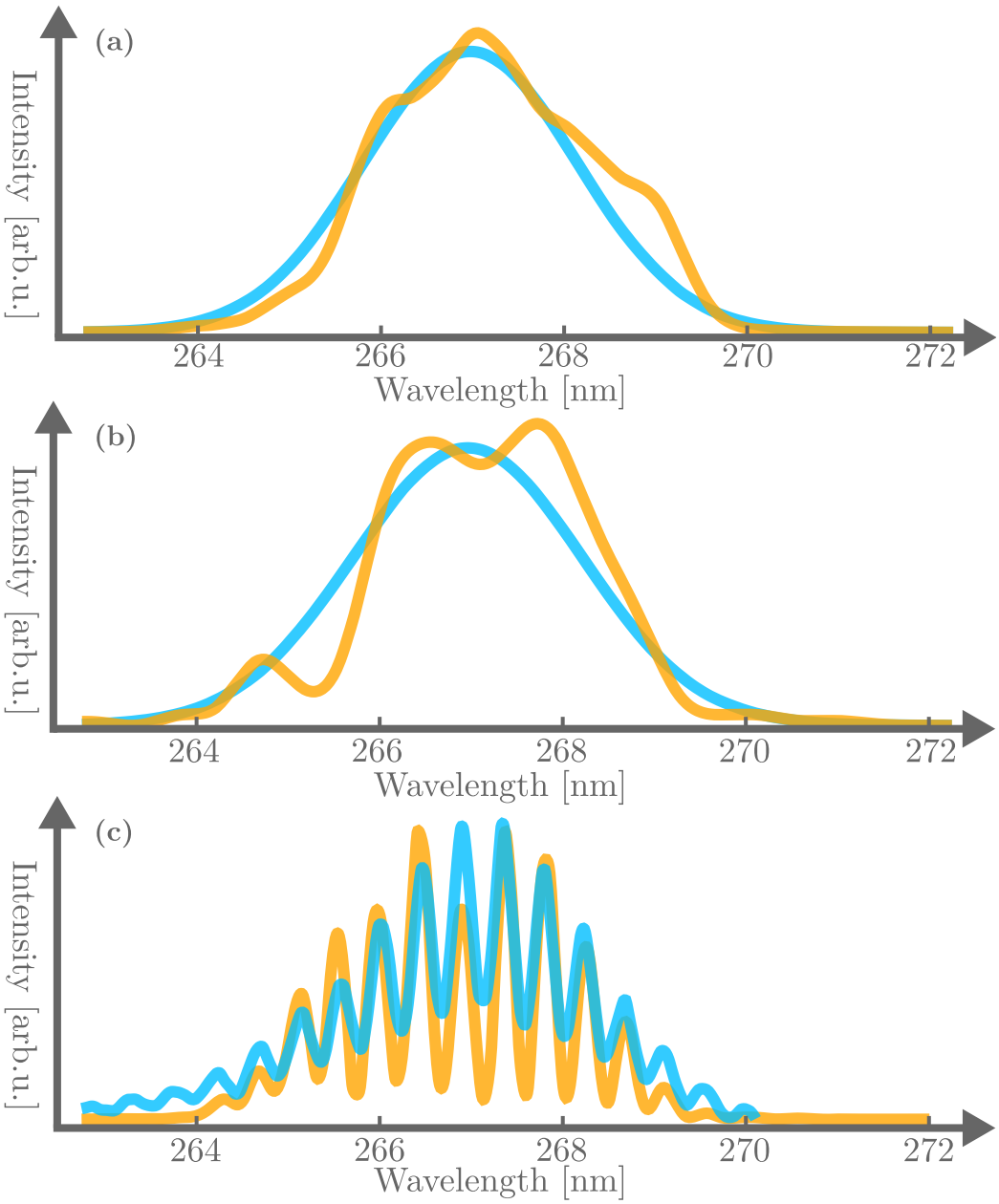

Figure 4.6: Measured (blue) and retrieved (orange) spectra (a) before the shaper, (b) after the shaper with a flat mirror mask and (c) after the shaper with the lamellar mirror mask. The measured data is the result of 300 averaged and normalised shots.

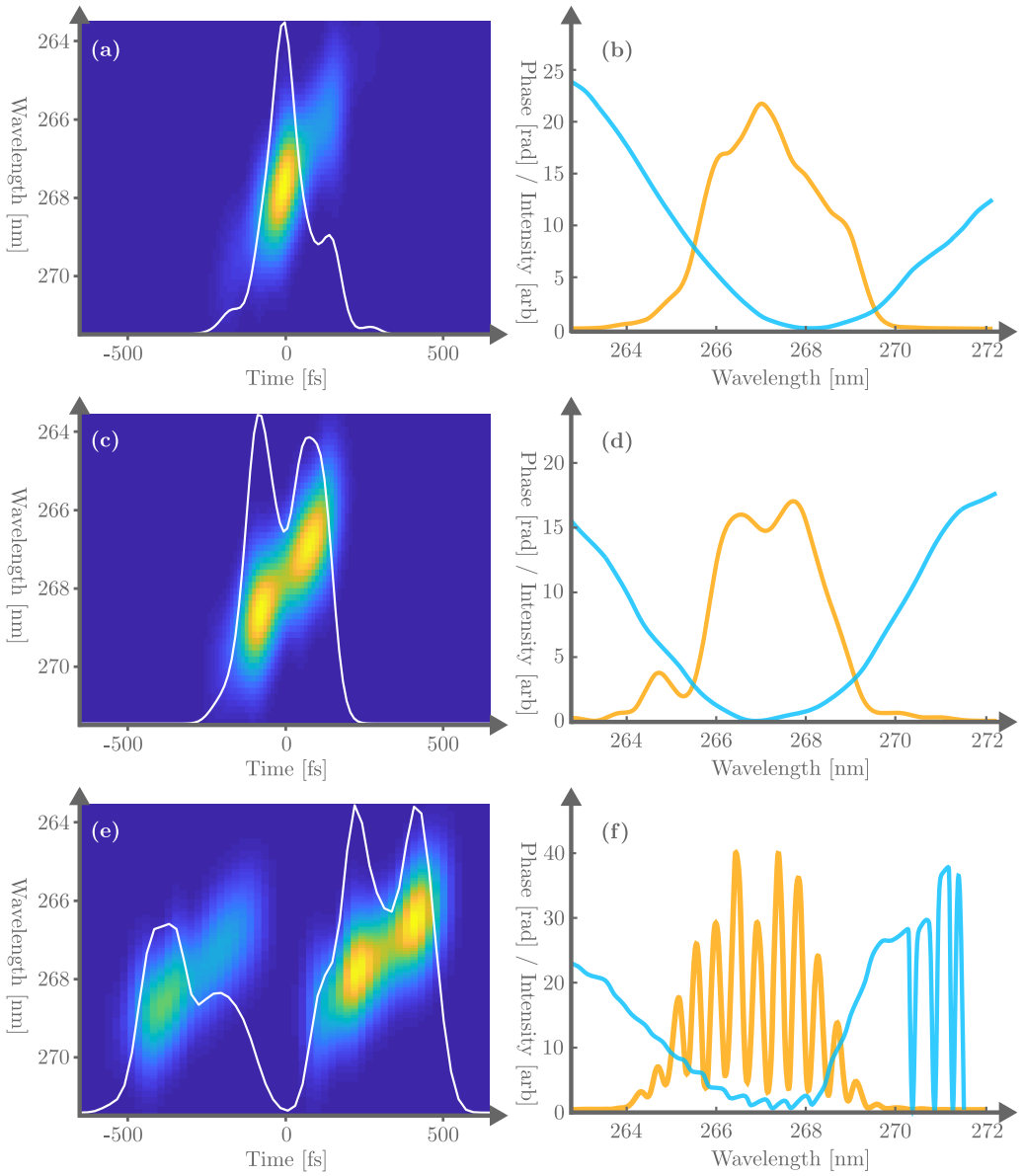

Figure 4.7: Spectrograms, spectrum (orange) and spectral phase (blue) for the DUV pulse, retrieved by means of frequency-resolved optical gating measured before the shaper (a, b), after the shaper with a plane mirror as phase mask (c, d) and after the shaper using a lamellar-mirror amplitude mask (e, f). Clearly visible in each figure is a positive linear chirp, that translates from before the shaper to behind the device with both a flat mirror and lamellar mirror assembly installed in the Fourier plane of the shaper. The electric field envelope is displayed on each spectrogram as a white line. The double pulse in (e) is separated in time domain at 630 ± 24 fs. Each time step in the data was measured as the average of 200 shots for the raw data.

4.5.3 Simulation of a Shaped Double Pulse

To reproduce the experimental data a simulation using the FROG code from SWAMP optics was performed. Both a single and double pulse were simulated and can be seen in Figure 4.8. The pulses are assumed the be perfectly Gaussian. The properties of the simulated single pulse are 150 fs FWHM pulse duration and -0.000175 fs^{-2} linear chirp. The reference pulse used to retrieved the spectrogram was a Fourier-limited 50 fs pulse at a central wavelength of 810 nm. The spectrogram and electric field of the single pulse can is shown in Figure 4.8(a) and the spectrum and phase in 4.8(b). The properties of the simulated double pulse are 150 fs FWHM pulse duration and -0.000175 fs^{-2} linear chirp for both the pre- and post-pulse. The separation between the pulses was set at 600 fs. The relative strength of the pre-pulse was set to 1.5$\times$ that of the post-pulse. The reference pulse used to retrieved the spectrogram was again an 810 nm Fourier-limited 50 fs pulse. The spectrogram and electric field of the double pulse can be seen in Figure 4.8(c) and the spectrum and phase in 4.8(d). The overall agreement between simulation and experimental data is good.

4.5.4 Open-loop Control

After generating a phase-locked DUV double pulse the next step is to demonstrate coherent control capabilities of the pulse shaping device [76]. For an amplitude mask that periodically modulates the pulse spectrum, such control can be achieved by translating the lamellar mirror assembly along the dispersion plane of the input beam in the Fourier plane. Shifting the selection of reflected spectra segments will cause the center-of-mass wavelengths of the pre- and post-pulse to oscillate within the spectral bandwidth of the input pulse, as depicted visually in Figure 4.9. To observe the spectral effect of the lamellar mirror mask as it moved laterally in the Fourier plane, a spectrogram of transmitted wavelength vs. motor position was taken. This can be seen in Figure 4.10 and shows that the amplitude modulation of the spectrum can be controlled precisely[6]. Upon recollimation of the modulated pulse spectrum, when propagating through the symmetric second half of the shaper, a phase-locked double pulse is generated in time domain. The center-of-mass wavelength of the pre- and post-pulse oscillates with a π phase difference as a function of the amplitude mask position. The theory behind this oscillation can be found in Wollenhaupt *et al.* Eq. 6 [120]. In turn, the relative phases between the formed pre- and post-pulses can be controlled by means of a

[6]Comparing Figure 4.6 and Figure 4.10 it is apparent that the spectral widths of the modulated spectra do not match. This is due to the data in Figure 4.10 being taken prior to that of Figure 4.6 while a different tripler with thicker crystals was used. The thicker crystals limited phase matching and provided a narrower spectral bandwidth for the generated DUV pulses.

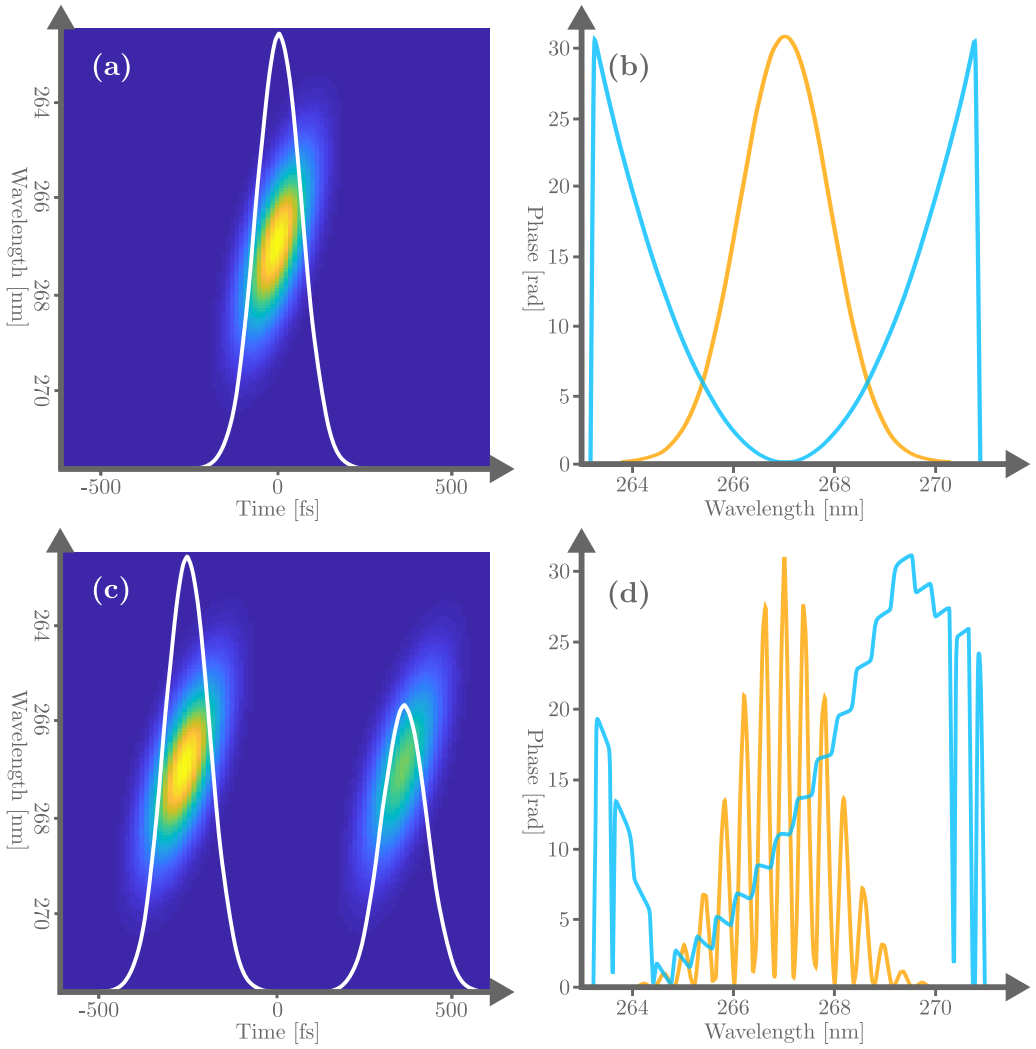

Figure 4.8: Simulated DUV pulse before the shaper (a, b) with spectrogram, electric envelope (white), spectrum (orange) and phase (blue). Simulated amplitude shaped pulse after the shaper (c, d) with the same colour scheme. Simulations were made with the same FROG software used for the retrieval of the experimental data but with computer generated inputs.

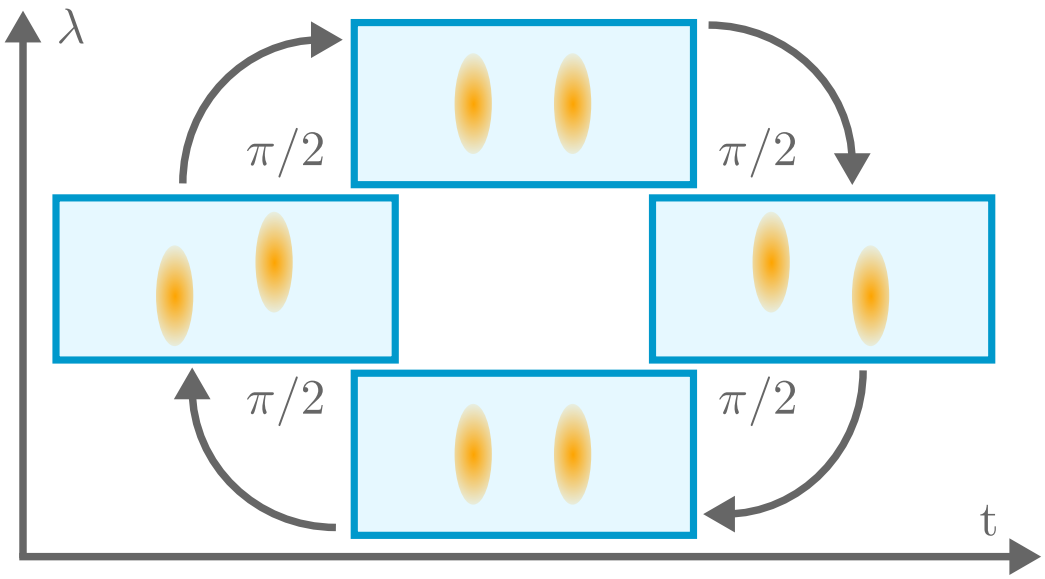

Figure 4.9: Stylised representation of the center-of-mass wavelength oscillations of the pre- and post-pulse as the amplitude modulation mask moves over the spectra for a 2π range (being equivalent to the lamellar mirror assembly period of 0.25 mm for lateral movement) in steps of $\pi/2$.

specific lamellar mirror assembly position [59]. The relative phase values repeat over a 2π period, which corresponds to the spatial mask period of 0.25 mm in the Fourier plane of the shaper. It is important to note that the temporal separation between the pre- and post-pulse stays constant in this "open-loop" control protocol [21]. The results of scanning the lamellar mirror mask in steps of $\sim \pi/2$ can be seen in Figure 4.11. The plotted points are the center-of-mass wavelength for the pre- and post-pulse at each step, with error bars in grey. The sinusoidal fit of the points is given in blue. The center-of-mass wavelengths oscillate with a relative phase difference of $\pi/2$ as expected. The data was retrieved from the reconstructed X-FROG pulse, with each step being the average of 200 shots.

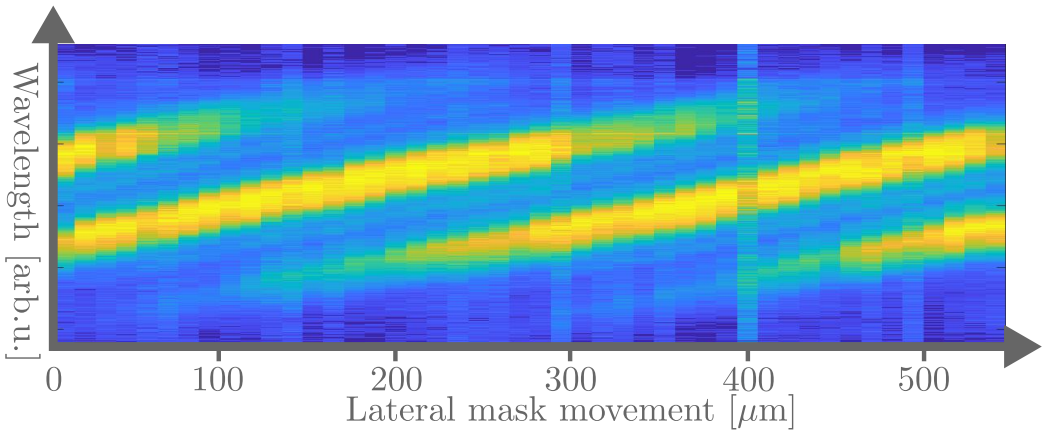

Figure 4.10: DUV spectrum recorded as function of lamellar mirror mask position. Mask movement is along the direction of dispersion of the DUV in the Fourier plane. The spectrum is narrower than that in Figure 4.7(f) as the THG BBO used here to generate the DUV was much thicker, reducing the spectral bandwidth via reduced phase matching.

4.5.5 Towards Closed-loop Control

The first step towards closed-loop shaping control will be to replace the lamellar mirror mask with a multi-mirror-array in the Fourier plane. Our group currently has access to one such array. The specifications of which are listed in Table 4.5.

Property	Specification
Pixelated mirror size	45×45 µm
Mirror separation	5 µm
Dimensions	192×128 Pixels
Surface material	Aluminium

Table 4.5: Micro-mirror-arrays (MMA) specifications

After MMA installation and alignment, the next step will be to develop custom control software, which is coupled with the pulse diagnostics at the end of the shaper. Allowing feedback from pulse characterisation to be applied to the MMA control software. This in turn would, after an initial commissioning phase, allow our software to generate bespoke output pulses shaped in both phase and amplitude on command.

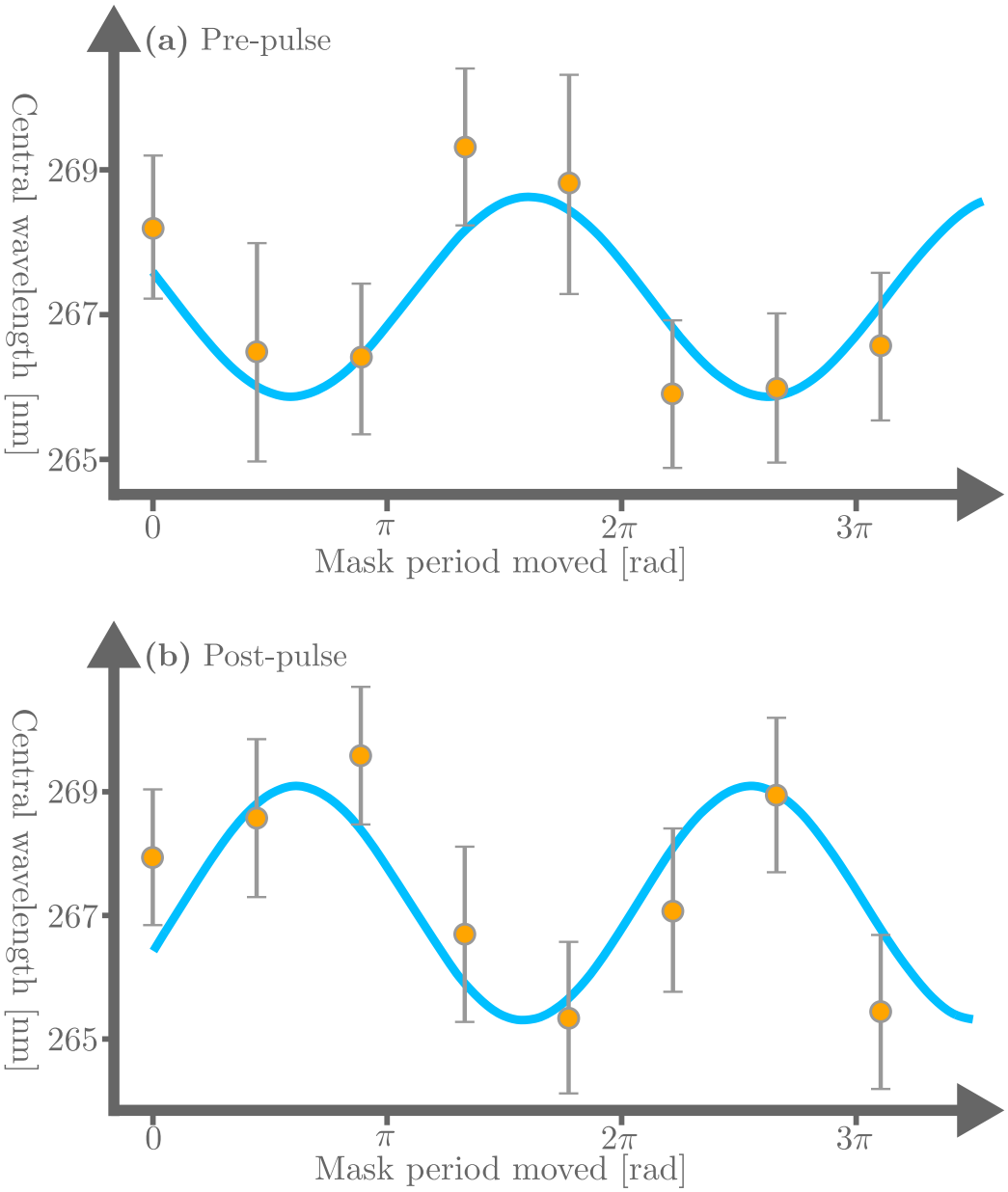

Figure 4.11: Retrieved center-of-mass wavelength oscillations for the pre- (a) and post-pulse (b) as a function of amplitude mask position in the Fourier plane as the amplitude modulation mask moves over the spectra for a 4π range (2π being equivalent to the lamellar mirror assembly period of 250 µm for lateral movement) in steps of $\pi/2$. Data points shown in orange, error bars in grey and fit in blue.

4.6 XUV Pulse Generation from Seeded FLASH

The XUV pulses used in this work were generated by seeding the FLASH FEL with seed pulses centered at 266 ± 1.7 nm with $\sim 350 \pm 35$ µJ pulse energy and pulse durations between 130-400 fs[7]. The DUV pulses are generated by two separate seeds, either of which can be used to seed the FEL for HGHG operation independently (see Figure 3.1 for reference). When the seed pulse is both longitudinally and transversely overlapped with the compressed electron bunch in the modulators of FLASH the seed modulates the energy distribution of the electron bunch. The transverse overlap is achieved by means of fluorescence detection from removable Ce:YAG screens placed before and after each modulator. The fluorescence indicates where the transverse positions of these beams are, allowing overlap to be obtained using motorised mirrors for the laser beam, or magnets for the electron beam. The longitudinal overlap is coarsely achieved by use of a photo-multiplier tube looking at fluorescence from both the electron beam and laser beam. This method allows overlap to within 50 ps to be obtained. Precise longitudinal overlap is achieved by slowly scanning the relative time delay of the laser with respect to the electron bunch while looking at the pulse energy measured with a **M**icro**C**hannel **P**late (MCP) detector. When longitudinal overlap is reached (assuming correct transverse overlap) the laser pulse will begin seeding the electron bunch, and the MCP reading will show a sharp peak. To test that what is viewed is seeded radiation and not SASE both the seed laser beam and the electron beam are individually turned off to view the effect on the signal. The electron bunch parameters are 650 MeV beam energy, a charge of 0.4 nC and a peak current of 450 A. The electron beam is linearly chirped within the laser-electron bunch overlap region. The space-charge distribution of the electrons within the bunch for various points in the HGHG setup can be seen in Figure 4.12. One can look at the longitudinal phase space of the electron beam after sending it through a rapid transversely deflecting structure and see the energy modulation by eye. An example of a modulated vs. an unmodulated electron bunch measured by means of this rapid transverse deflection system after the seeding radiator section in FLASH is displayed in Figure 4.13 [123], with the difference between the two bunches magnified.

The DUV pulse energy used for HGHG seeding is on the order of 300 µJ in the focus at the center of the modulator. Typical shot-to-shot spectra for HGHG XUV pulses can be seen in Figure 4.14 for the 7^{th} harmonic of the seed laser. FLASH can produce seeded pulses at the 7^{th} harmonic of the 266 nm seed laser

[7] The pulse duration changes between individual experiments due to variations in the fundamental between successive beamtimes, as well as laser-induced damage on optics and on the non-linear up-conversion crystals during operation at high-average power levels close to damage thresholds to achieve sufficient seed power.

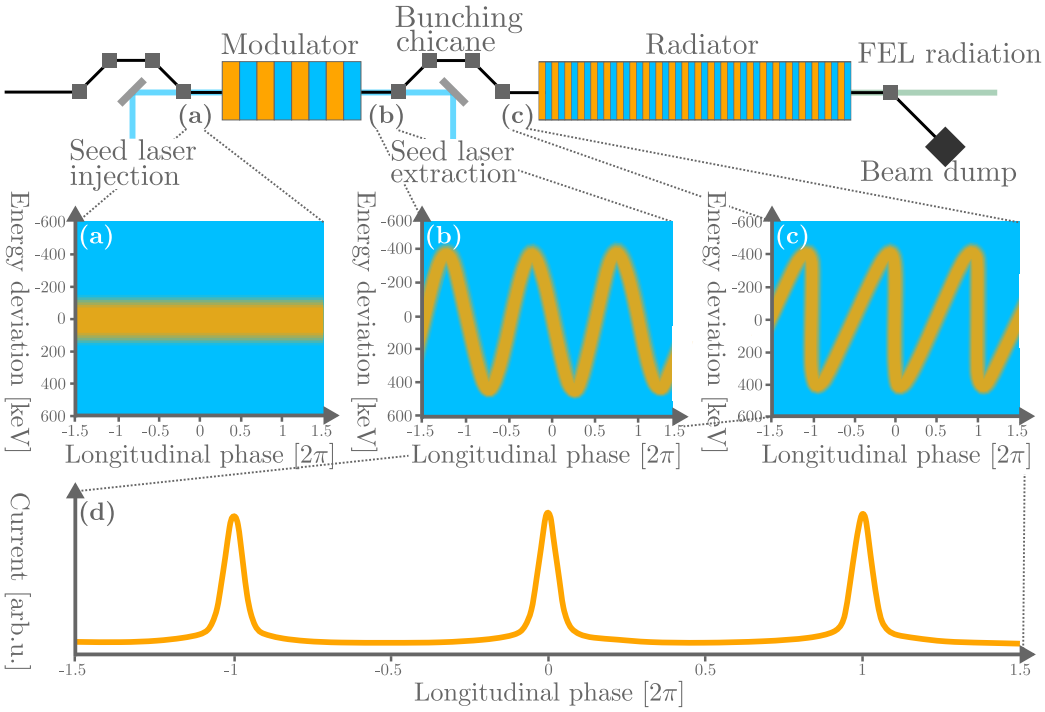

Figure 4.12: HGHG diagram from Figure 2.10(a) with the longitudinal phase space distribution of the electrons at three points (a), (b) and (c) in the setup highlighted. The longitudinal phase π represents one seed wavelength. The graph of the electron density at location (c) is shown in (d), where it can be seen that a large fraction of the electrons is confined within distances smaller than the seed wavelength, thus having a higher harmonic content. Figure adapted from [124].

with pulse energies of up to 75 µJ [125] and pulse durations between 58 $\pm$7.5 fs [112] and 350 $\pm$ 35 fs (see subsection 4.7.1). In Figure 4.15 a previous THz streaking measurement done by Azima *et al.* in 2017 [112] is seen. Figure 4.15(a) shows a typical THz streaking spectrogram used to retrieve the pulse duration. Figure 4.15(b) shows a histogram with various pulse durations retrieved by individual THz streaking scans. In Figure 4.15(a) the labels R_0, R_+ and R_- denote regions of similar kinematics. At R_0 the XUV and THz pulses are not longitudinally overlapped and photo-electron spectra are not yet streaked. This therefore represents the unperturbed spectrum of the ionised 3p-argon valence electrons. In this R_0 region it is possible to study the shot-to-shot spectral variation of the pure seeded FEL pulse. Region R_+ ranges from 0.3 - 0.6 ps and region R_- ranges from 0.9 - 1.2 ps. In this R_+ region the slope of the energy gain curve is positive and in the R_- region it is negative. In both cases the slope is approximately constant. In the two inflexion points σ_+ and σ_- of the energy gain curve the slope has an extremum providing highest streaking strength. A linear fit of the streaking trace

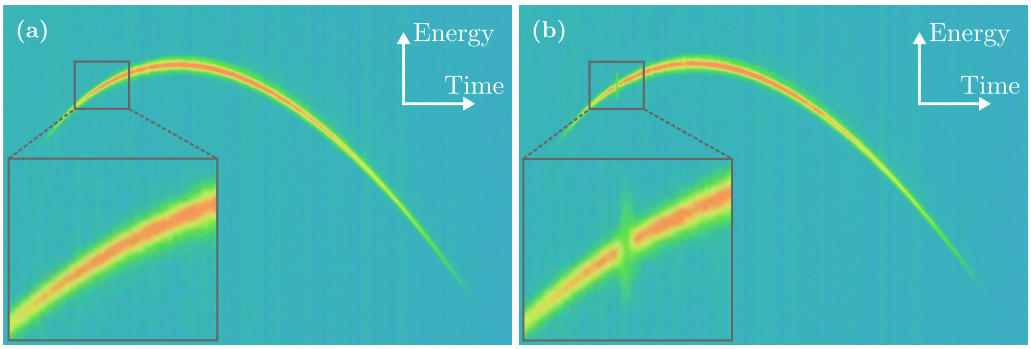

Figure 4.13: Measured data from an unmodulated (a) vs modulated (b) electron bunch in the July FLASH seeding shift 2021. In (b) a clear energy modulation is visible, highlighted via magnification. The same spot is magnified in (a) to view the difference. The electron bunch here is measured after the radiator shown in Figure 4.12. The DUV seed here is 200 fs long.

at these two points reveals streaking speeds s_+ and s_- with $+16.8$ meV/fs and -23.0 meV/fs respectively. It is possible to extract the pulse duration from the spectral broadenings $\sigma_{+,-}$ at both streaking points $R_{+,-}$ by deconvoluting them with the unstreaked photo-electron spectrum σ_0 (see equations 2.82 and 2.83 for reference). The streaking speed within this region can be approximated as linear, allowing the deconvoluted photo-electron spectrum to be linearly mapped to time by dividing by the streaking speed, which is defined as the gradient at $\sigma_{+/-}$. This process can be seen diagrammatically in Figure 4.16. Assumptions here are that the spectrum and temporal profile of the measured pulse are Gaussian. The response of the streaking to the XUV pulse energy is linear, allowing low XUV pulse energies down to pJ to be measured with relative ease.

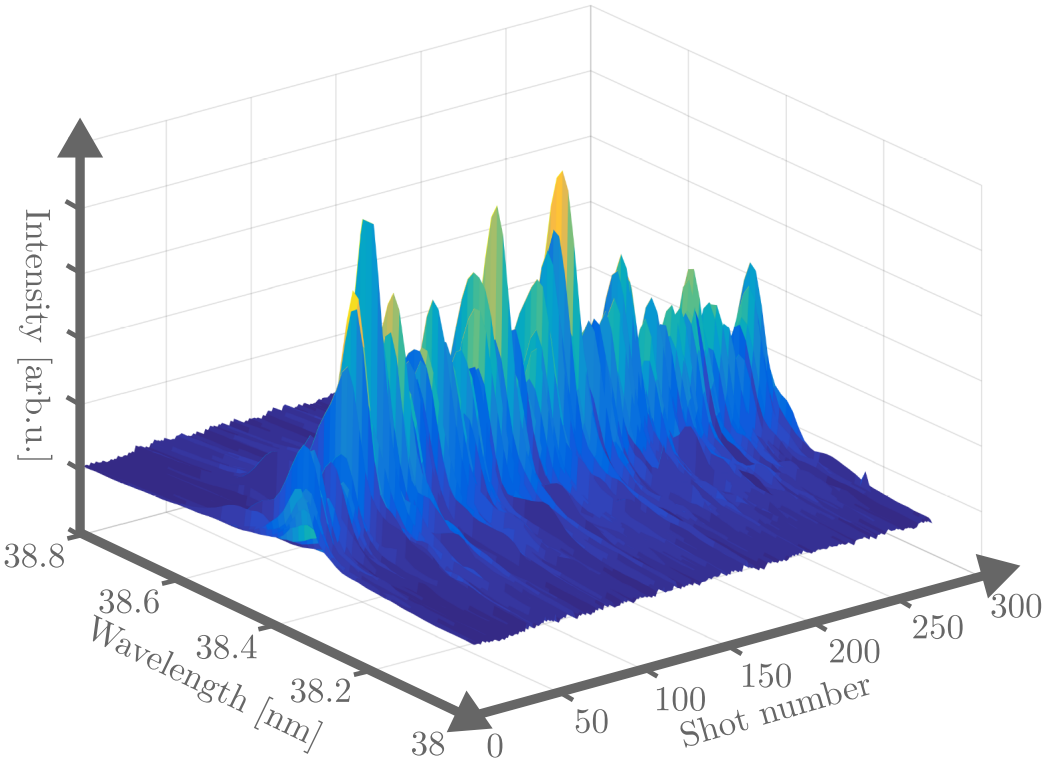

Figure 4.14: Typical spectra of 300 consecutive HGHG FEL pulses from FLASH operating at the 7th harmonic of the 266 nm seed laser. The shot-to-shot spectral stability is present in the central wavelength and in the spectral bandwidth of subsequent pulses. The individual spectra are approximately Gaussian. Figure adapted from [45].

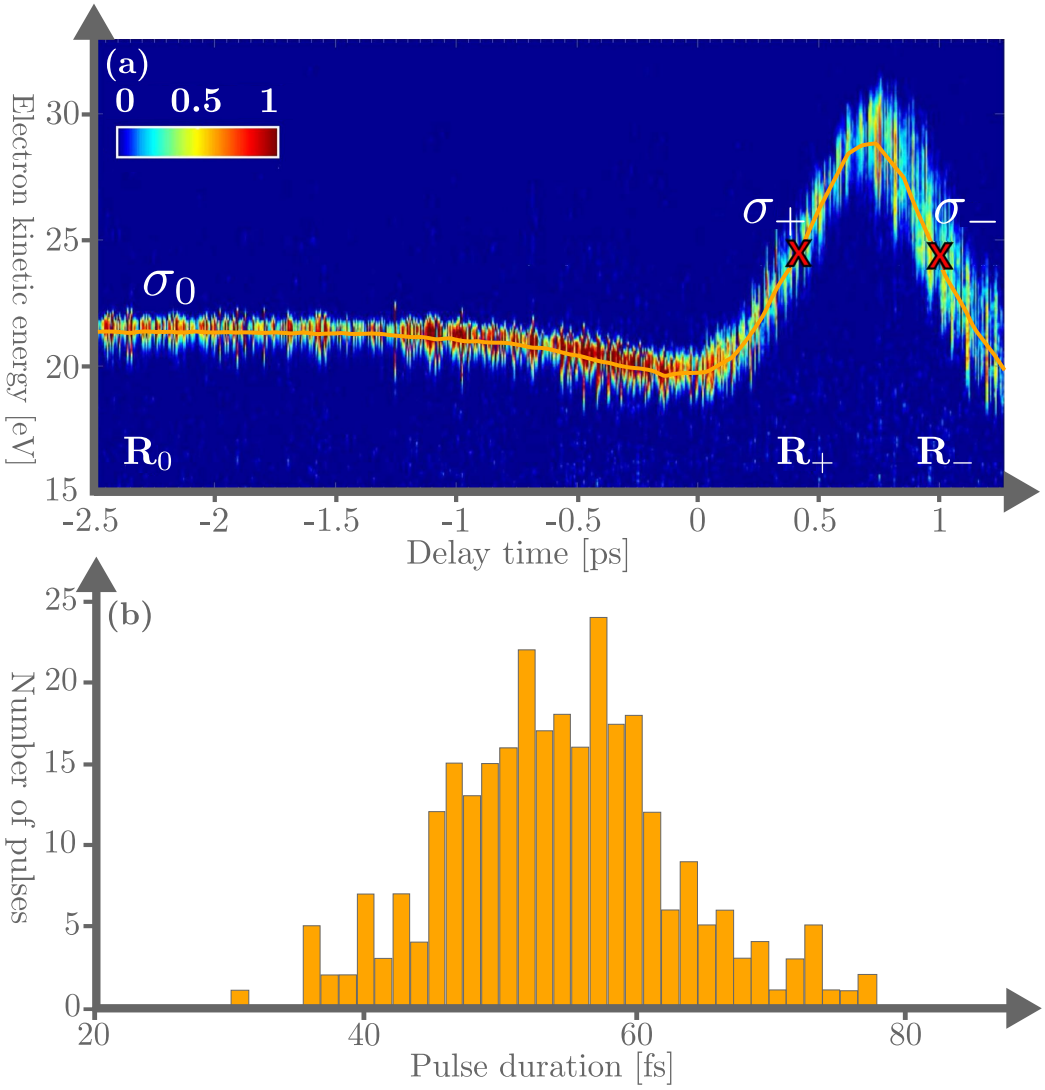

Figure 4.15: (a) THz streaking measurement of 38.4 nm seeded FEL XUV pulse produced by FLASH. The 266 nm seed has a pulse duration of 130 fs. From this data, one can retrieve a pulse duration histogram (b) by using the gradient of the THz streaking spectrogram at the characteristic points labeled σ_+ and σ_- shown and the photo-electron spectrum at these points (in which the value σ_s from Equation 2.80 can be obtained). Details are given in the main text. From the histogram an average pulse duration of 54 ± 8 fs is obtained. Figures adapted from [112].

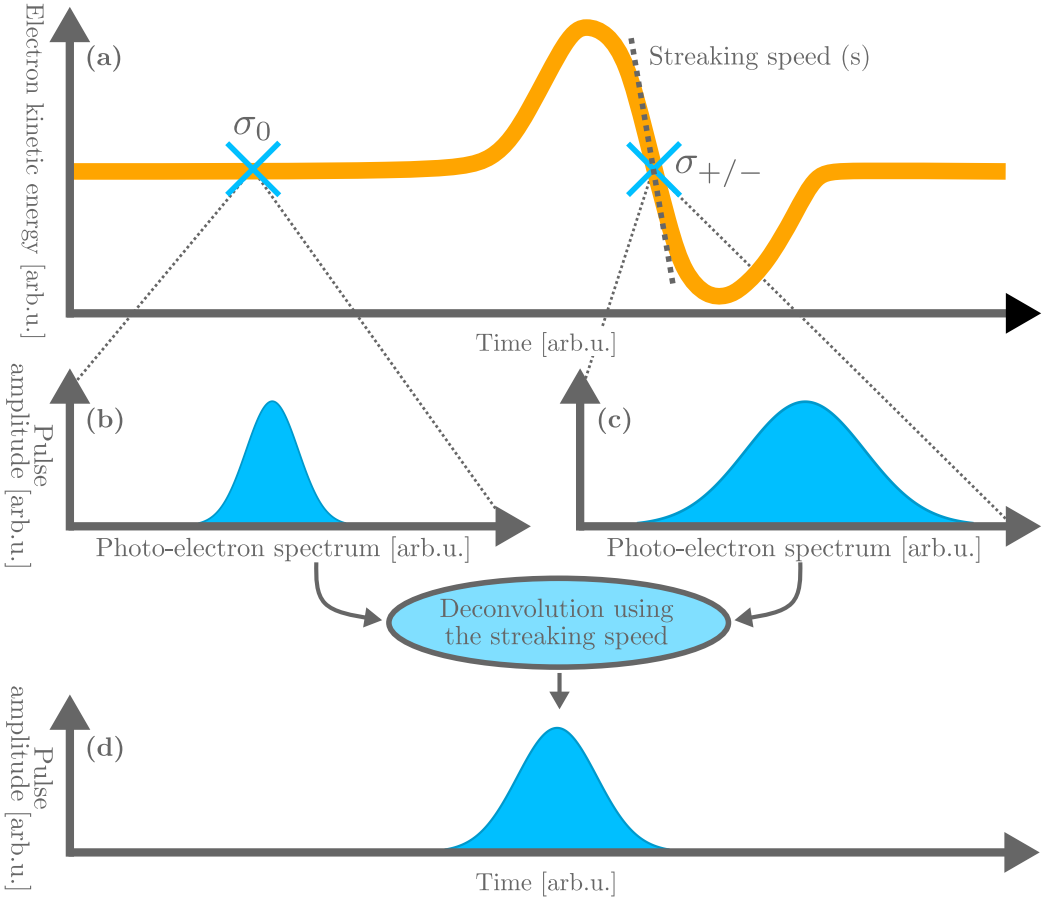

Figure 4.16: Stylised diagram of temporal pulse retrieval via THz streaking. In (a) a streaked pulse can be seen in orange, with the points σ_0 and $\sigma_{+/-}$ highlighted with blue crosses. The streaking speed is given by the gradient of the dotted grey line through $\sigma_{+/-}$. In (b) the unstreaked photo-electron spectrum from σ_0 is displayed and in (c) the streaked photo-electron spectrum from $\sigma_{+/-}$. Deconvoluting the two spectra and dividing by the streaking speed gives the temporal pulse profile information, as seen in (d). More details are given in section 2.8 and in the text.

4.7 XUV Pulse Shaping

Initial pulse shaping experiments in the XUV were performed by tailoring the properties of the DUV seed beam. The induced changes would then map in a particular way to the output XUV harmonic in the seeded FEL process. Within this chapter results showing the effect of introducing a positive chirp upon the DUV seed pulse and its impact upon the XUV FEL pulse will be discussed.

4.7.1 Chirping the Seed Laser Pulses

The DUV beam used to seed FLASH was chirped by introducing multiples of 1 mm thick UV fused silica plates into the DUV beamline to achieve positive GDD. For 266 nm pulses the added GVD for fused silica is 197.53 fs^2/mm. The DUV pulses used for this experiment were created using the Seed-1 and Seed-2 tripler units constructed in the same way within the X-Seed laser hutch[8]. The identical tripler optics specifications are listed in Table 4.6. Using the Seed-1 tripler the pulse duration of the DUV was measured as a function of the width of fused silica that was introduced in the DUV beamline in preparation of the beamtime at FLASH. The results can be seen in Figure 4.17[9]. The pulse duration was measured five times for each point using the single-shot cross-correlation method described in subsection 3.5.1. The pulse duration is roughly 240 fs with no added GDD showing that there is already a significant amount of chirp introduced in the frequency up-conversion process. The pulse duration increases as more fused silica is added. This shows that the initial DUV pulse is already positively chirped[10].

Table 4.6: Tripler optics specifications for DUV seed.

Tripler component	Thickness [mm]
Type 1 SHG BBO crystal 400-800 nm	0.2
α-BBO delay plate	1.00
Zero order wave-plate, λ/2@800+λ@400 nm	1.00
Type 1 SHG BBO crystal 400-800/266 nm	0.3

[8] The two seeds mentioned here can both be used to generate single-stage HGHG in FLASH. As such it is possible to switch between them in different experimental campaigns.

[9] The gain in pulse duration here was small due to the long initial DUV pulse duration and so the evolution of the graph appears linear.

[10] The Fourier limit of the DUV pulse is ~33 fs, so a negatively chirped pulse would reduce with added GVD from an initial 240 fs pulse duration.

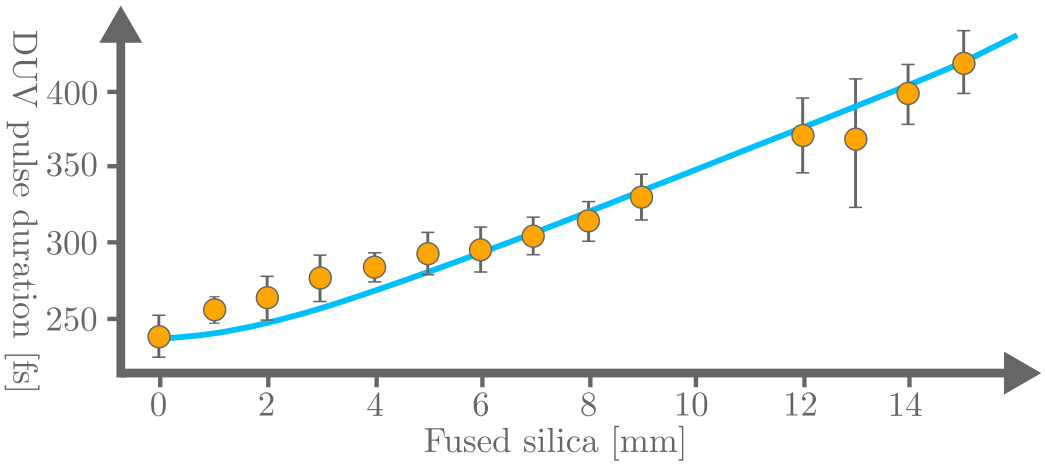

Figure 4.17: DUV pulse duration recorded from single-shot cross-correlation for various thicknesses of UV fused silica placed in the DUV beampath (orange) and theoretical pulse duration for each added amount of GDD (blue). The theoretical pulse duration increase was calculated assuming a 266 nm pulse with a 2.8 nm bandwidth giving a Fourier-limited pulse duration of ~ 33 fs. The agreement between theory and experiment is good.

4.7.2 Chirping the Seeded XUV Pulses

To measure the XUV pulse duration the THz streaking setup described in section 3.6 was used. The streaking was performed using the 7^{th} harmonic of the 266 nm DUV seed generated from the Seed-2 tripler modulating the electron bunch. Unfortunately, during the beamtime the Seed-1 laser was not available. The pulse duration of the DUV was measured as 350 ± 35 fs, which is significantly larger than the characterised seed pulses in the preparatory works. However, the experiment to control the chirp of the seeded XUV pulse was performed by measuring the XUV pulse duration for differing amounts of fused silica placed into the DUV beam path, i.e. by chirping the seed. After each insertion the longitudinal overlap between DUV and electron pulse had to be re-found and readjusted for successful seeding once more.

Four different widths of fused silica were investigated. The results of the individual streaking scans can be seen in Figure 4.18(a) for 0, 1, 3 and 5 mm of inserted fused silica into the seed beam. The DUV seed pulse duration measurement can be seen in Figure 4.18(b). The XUV pulse duration was measured as $\sim 350 \pm 40$ fs for each scan, derived from the FWHM of the THz streaking trace retrieved from σ_-, which was measured at the point R$_-$. Unfortunately, no observable effect was present upon the resulting XUV pulse as a result of inserting the fused silica. The long 266 nm seed pulse duration was taken as the cause of the lack of visible change in the XUV pulse duration. This is likely due to mini-

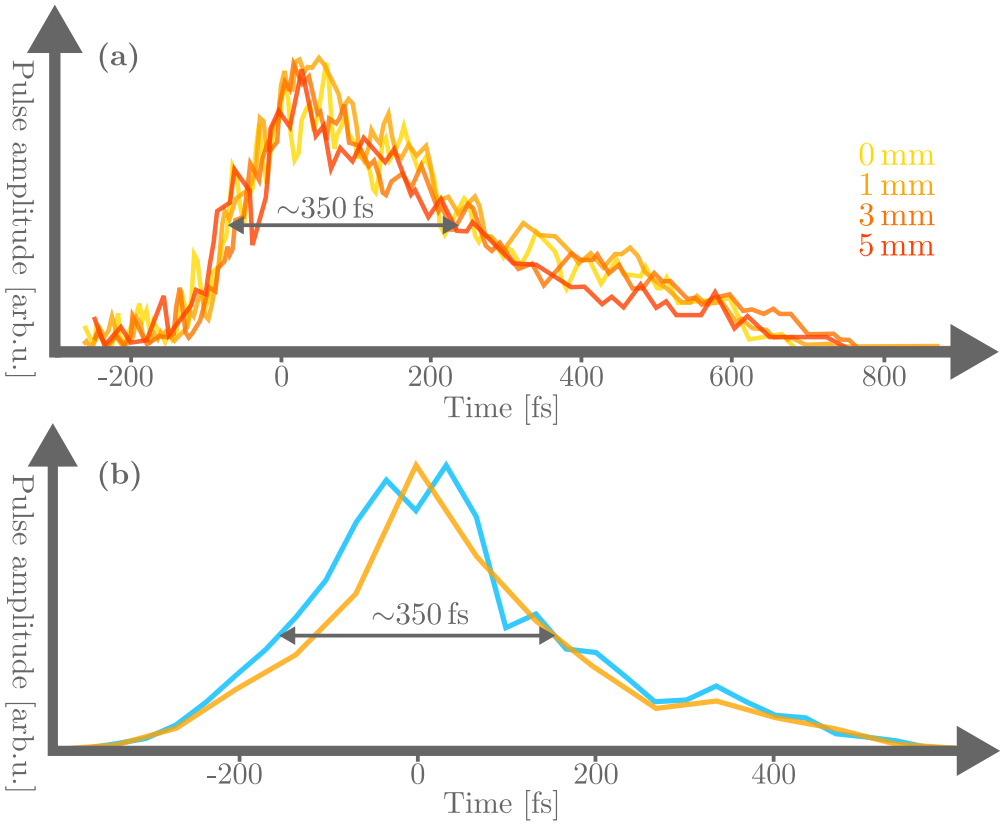

Figure 4.18: (a) THz-streaking retrieved pulse durations from the ToF spectrometer for 0 mm, 1 mm, 3 mm and 5 mm fused silica plates placed in DUV seed beam (colour key in figure). The pulse durations plotted in (a) are retrieved from the deconvoluted spectral broadening at point σ_-, as described in the text. No significant pulse duration change is present due to large initial seed pulse duration ($\sim$ 350 fs). (b) Normalised DUV pulse duration as measured from single-shot (orange) and temporal scan (blue) for the DUV pulse used for FEL seeding. The single-shot scan was measured using a setup similar to that described in subsection 3.5.1 and the temporal scan was retrieved by means of scanning a retro-reflecting delay using an actuator.

mal increase in the seed pulse duration from adding small widths of fused silica and thus small added GDD[11].

Further plans for THz streaking revolve around shortening the DUV seed pulse duration in order to shorten the XUV pulse duration. A shorter DUV seed would also experience a longer pulse duration increase per millimeter of added GDD. This would allow clearer observation of the effect of chirping the DUV seed upon the XUV pulse. Experimentation with harmonics other than the 7^{th} is also being considered.

4.8 Future Plans for X-Seed

Upgrades to the seeding scheme at FLASH are currently in process. Aiming to allow more stable operation of HGHG seeding and pave the way for future experiments with EEHG seeing at FLASH. This would provide more brilliant XUV pulses with shorter pulse durations. Currently the seeding at FLASH is performed with two 266 nm seeds, Seed-1 and Seed-2, both currently with roughly 200 fs pulse durations[12]. In the facility upgrade these lasers will be replaced by one seed wavelength-centered at 343 nm with a 500 fs pulse duration and another seed tunable between 294-317 nm at a pulse duration of 50 fs. On top of this, the modulators (with 200 mm period length) used for seeding will be replaced by new ones with a period of 90 mm. The effective length of the modulator will also be increased from 1.2 m to 2.5 m. Finally the radiators (with a period of 31.1 mm) will also be replaced by new helical ones with a period of 33 mm. The radiators will also increase their effective length from 10 m to 27 m. Using these new seeds, new modulators and radiators, alongside various upgrades to diagnostics in the FLASH tunnel, will allow easier and more consistent operation of seeding at FLASH.

[11]It is noted and reiterated that the pulse duration measurements in Figure 4.17 made use of Seed-1 whereas the THz streaking experiment for the results in Figure 4.18 were performed using Seed-2. The two different seeds have different pulse durations.

[12]Changes have been made to the general laser setup in the seeding laser hutch since the experiments detailed in subsection 4.7.1 such that the pules duration of both seeds is different.

Chapter 5

Conclusion and Outlook

The results presented in this work show the following:

- First operation of an all-reflective pulse shaper in the DUV with full characterisation of spectral-amplitude-shaped pulses flanked by simulated shaped DUV pulses for comparison. Alongside this, quantitative measurements of the DUV shaper transmission have been presented.
- Full control over the relative carrier-envelope phases of the pre- and post-pulse in an open-loop control scheme displayed over a 4π range.
- Characterisation of seeded XUV pulses and comparison to SASE pulses with differences highlighted.
- Current progress made towards shaping seeded FEL pulses by chirping the DUV seed with characterisation of the resulting seeded XUV pulses using the method of THz streaking.
- Steps towards future XUV shaping schemes by using the all-reflective pulse shaper after the seeded FEL, as well as descriptions of the diagnostics used to characterise them.

The key result of the present PhD project is the the demonstration and full characterisation of an open-loop shaping control protocol realised in the DUV spectral range. The spectrograms, spectra and phases of both shaped and unshaped pulses have been shown, which were recorded before and after the shaper for comparison. Full characterisation of the 810 nm reference pulse retrieved by GRENOUILLE has also been presented. Next steps in the development of the pulse shaper would be to replace the current lamellar mirror mask with a complex shaping mask such as a micro-machined-deformable mirror or micro-mirror array to allow for both amplitude and phase shaping capabilities to be explored.

Further, closed-loop control systems with shot-to-shot diagnostics and feedback will be developed, allowing for full arbitrary control over the phase and amplitude of the DUV pulse. After this has been achieved and full closed-loop operation demonstrated, the pulse shaper will shift to XUV operation. Again, initially open-loop amplitude shaping and control over the XUV pulse will be the primary goal, followed by a similar closed-loop system that is currently planned for the DUV operation. Full control over the phase and amplitude of XUV pulses would open up many interesting avenues of study. To achieve this custom focusing optics coated with amorphous carbon will be required to be designed and manufactured to allow efficient operation in the XUV regime as well as custom XUV gratings, as XUV reflectivities even under grazing incidence are rather low.

Simultaneous seeded FEL and SASE operation in two different beamlines has also been shown, which allows for more efficient use of beamtime for FEL research and development projects. Work towards shaping the seeded XUV pulses by means of first tailoring the DUV seed has been shown. Positive chirp was added to the DUV pulse used to generate the seeded FEL at the 7^{th} harmonic and the resulting XUV pulses were characterised by THz streaking. Due to the already relatively long DUV seed pulse the recorded THz pulses were unable to show any significant change as a result of adding additional group-delay dispersion to the seed. This work will be continued utilising temporally shorter DUV seed pulses to begin with.

Acknowledgements

Firstly I would like to thank my supervisor, Tim Laarmann for helping guide me through the PhD process, and especially for enduring my sense of humour over the last four years.

As well I would like to thank my colleagues Andreas Przystawik, Mahesh Namboodiri, Slawomir Skruszewicz, Sergey Usenko, David Schwickert, Malte Sumfleth, Cheng Luo, Dian Diaman, Fabian Pannek and Georgia Paraskaki for spending the time proofreading my work.

Finally I would also like to thank Pragya Chopra and Gayatri Batra for being my workout and jogging buddies as well as Benjamin Arenas for helping provide me with copious amounts of ingestible ethanol during my PhD time.

Bibliography

[1] A. Einstein. “Strahlungs-Emission und-Absorption nach der Quantentheorie”. In: *Verh. Deutsch. Phys. Gesell.* 18 (1916), pp. 318–323.

[2] A. Einstein. “Zur Quantentheorie der Strahlung”. In: *Phys. Z.* 18 (1917), p. 124.

[3] T. H. Maiman. “Stimulated optical radiation in Ruby”. In: *Nature* (1960).

[4] P. T. Houldcroft. *Welding processes*. CUP Archive, 1967.

[5] P. L. Bender et al. “The Lunar Laser Ranging Experiment: Accurate ranges have given a large improvement in the lunar orbit and new selenophysical information”. In: *Science* 182.4109 (1973), pp. 229–238.

[6] A. Ashkin. “Acceleration and trapping of particles by radiation pressure”. In: *Physical review letters* 24.4 (1970), p. 156.

[7] L. E. Hargrove. “Mode locking in a synchronously modulated maser”. In: (1968). US Patent 3,412,251.

[8] K. C. Kao and G. A. Hockham. “Dielectric-fibre surface waveguides for optical frequencies”. In: *Proceedings of the Institution of Electrical Engineers*. Vol. 113. 7. IET. 1966, pp. 1151–1158.

[9] D. A. G. Deacon et al. “First operation of a free-electron laser”. In: *Physical Review Letters* 38.16 (1977), p. 892.

[10] A. Javan, W. R. Bennett Jr, and D. R. Herriott. “Population inversion and continuous optical maser oscillation in a gas discharge containing a He-Ne mixture”. In: *Physical Review Letters* 6.3 (1961), p. 106.

[11] W. B. Bridges. “Laser oscillation in singly ionized argon in the visible spectrum”. In: *Applied Physics Letters* 4.7 (1964), pp. 128–130.

[12] J. E. Geusic and G. Le Grand. “Nd3+-yag laser amplifier and oscillator”. In: (1966). US Patent 3,252,103.

[13] M. Ross. “YAG laser operation by semiconductor laser pumping”. In: *Proceedings of the IEEE* 56.2 (1968), pp. 196–197.

[14] M. Hentschel et al. “Attosecond metrology”. In: *Nature* 414.6863 (2001), pp. 509–513.

[15] M. F. Kling and M. J. J. Vrakking. “Attosecond electron dynamics”. In: *Annu. Rev. Phys. Chem.* 59 (2008), pp. 463–492.

[16] M. Nisoli et al. “Attosecond electron dynamics in molecules”. In: *Chemical Reviews* 117.16 (2017), pp. 10760–10825.

[17] A. Assion et al. “Control of chemical reactions by feedback-optimized phase-shaped femtosecond laser pulses”. In: *Science* 282.5390 (1998), pp. 919–922.

[18] W. S. Warren. “Chemistry with photons”. In: *Science* 262.5136 (1993), pp. 1008–1010.

[19] T. Laarmann et al. “Control of giant breathing motion in C 60 with temporally shaped laser pulses”. In: *Physical review letters* 98.5 (2007), p. 058302.

[20] A. Assion et al. “Coherent control by a single phase shaped femtosecond laser pulse”. In: *Chemical Physics Letters* 259.5-6 (1996), pp. 488–494.

[21] T. Laarmann et al. “Coherent control of bond breaking in amino acid complexes with tailored femtosecond pulses”. In: *The Journal of chemical physics* 127.20 (2007), p. 201101.

[22] C. P. Koch and M. Shapiro. “Coherent control of ultracold photoassociation”. In: *Chemical reviews* 112.9 (2012), pp. 4928–4948.

[23] I. I. Beterov et al. “Coherent control of mesoscopic atomic ensembles for quantum information”. In: *Laser Physics* 24.7 (2014), p. 074013.

[24] A. A. Abbott et al. “Communication through coherent control of quantum channels”. In: *Quantum* 4 (2020), p. 333.

[25] H. J. Williams et al. “Magnetic trapping and coherent control of laser-cooled molecules”. In: *Physical review letters* 120.16 (2018), p. 163201.

[26] F. Bencivenga et al. “Four-wave mixing experiments with extreme ultraviolet transient gratings”. In: *Nature* 520.7546 (2015), pp. 205–208.

[27] W. Schäfer et al. “Femtosecond coherent fields induced by many-particle correlations in transient four-wave mixing”. In: *Physical Review B* 53.24 (1996), p. 16429.

[28] F. Hu, L. Shi, and W. Min. “Biological imaging of chemical bonds by stimulated Raman scattering microscopy”. In: *Nature methods* 16.9 (2019), pp. 830–842.

[29] S. Brasselet. “Polarization-resolved nonlinear microscopy: application to structural molecular and biological imaging”. In: *Advances in Optics and Photonics* 3.3 (2011), p. 205.

[30] A. A. Michelson and E. W. Morley. “On the Relative Motion of the Earth and of the Luminiferous Ether”. In: *Sidereal Messenger, vol. 6, pp. 306-310* 6 (1887), pp. 306–310.

[31] D. Strickland and G. Mourou. “Compression of amplified chirped optical pulses”. In: *Optics communications* 55.6 (1985), pp. 447–449.

[32] R. Szipöcs et al. “Chirped multilayer coatings for broadband dispersion control in femtosecond lasers”. In: *Optics letters* 19.3 (1994), pp. 201–203.

[33] C. l. Froehly, B. Colombeau, and M. Vampouille. “II shaping and analysis of picosecond light pulses”. In: *Progress in optics* 20 (1983), pp. 63–153.

[34] A. M. Weiner. “Femtosecond pulse shaping using spatial light modulators”. In: *Review of scientific instruments* 71.5 (2000), pp. 1929–1960.

[35] M. A. Jakob et al. “Generation and characterization of tailored MIR waveforms for steering molecular dynamics”. In: *Optics express* 27.19 (2019), pp. 26979–26988.

[36] L. H. Yu. “Generation of intense uv radiation by subharmonically seeded single-pass free-electron lasers”. In: *Physical Review A* 44.8 (1991), p. 5178.

[37] P. R. Ribič et al. “Coherent soft X-ray pulses from an echo-enabled harmonic generation free-electron laser”. In: *Nature Photonics* 13.8 (2019), pp. 555–561.

[38] J. M. J. Madey. “Stimulated emission of bremsstrahlung in a periodic magnetic field”. In: *Journal of Applied Physics* 42.5 (1971), pp. 1906–1913.

[39] T. Ishikawa et al. “A compact X-ray free-electron laser emitting in the sub-ångström region”. In: *nature photonics* 6.8 (2012), pp. 540–544.

[40] J. Rossbach and Tesla Fel Study Group et al. “A VUV free electron laser at the TESLA test facility at DESY”. In: *Nuclear Instruments and Methods in Physics Research Section A: Accelerators, Spectrometers, Detectors and Associated Equipment* 375.1-3 (1996), pp. 269–273.

[41] M. E. Couprie. “New generation of light sources: Present and future”. In: *Journal of Electron Spectroscopy and Related Phenomena* 196 (2014), pp. 3–13.

[42] W. Ackermann et al. “Operation of a free-electron laser from the extreme ultraviolet to the water window”. In: *Nature photonics* 1.6 (2007), pp. 336–342.

[43] M. Kördel et al. “Laboratory water-window X-ray microscopy”. In: *Optica* 7.6 (2020), pp. 658–674.

[44] L. L. Lazzarino et al. “Shaping femtosecond laser pulses at short wavelength with grazing-incidence optics”. In: *Optics express* 27.9 (2019), pp. 13479–13491.

[45] L. L. Lazzarino. “Design and Commissioning of an XUV and Soft X-Ray FEL Pulse Shaper”. PhD thesis. Staats-und Universitätsbibliothek Hamburg Carl von Ossietzky, 2018.

[46] G. G. Paulus et al. “Measurement of the phase of few-cycle laser pulses”. In: *Physical review letters* 91.25 (2003), p. 253004.

[47] T. Brabec and F. Krausz. “Intense few-cycle laser fields: Frontiers of nonlinear optics”. In: *Reviews of Modern Physics* 72.2 (2000), p. 545.

[48] M. Wollenhaupt, A. Assion, and T. Baumert. “Femtosecond laser pulses: linear properties, manipulation, generation and measurement”. In: *Springer Handbook of Lasers and Optics* (2007), p. 937.

[49] R. W. Boyd. *Nonlinear optics*. Academic press, 2020.

[50] C. B. Schaffer, A. Brodeur, and E. Mazur. “Laser-induced breakdown and damage in bulk transparent materials induced by tightly focused femtosecond laser pulses”. In: *Measurement Science and Technology* 12.11 (2001), p. 1784.

[51] R. H. Stolen and C. Lin. “Self-phase-modulation in silica optical fibers”. In: *Physical Review A* 17.4 (1978), p. 1448.

[52] R. L. Fork et al. “Femtosecond white-light continuum pulses”. In: *Optics letters* 8.1 (1983), pp. 1–3.

[53] M. Malinauskas et al. “Ultrafast laser processing of materials: from science to industry”. In: *Light: Science & Applications* 5.8 (2016), e16133–e16133.

[54] K. Sugioka and Y. Cheng. “Ultrafast lasers—reliable tools for advanced materials processing”. In: *Light: Science & Applications* 3.4 (2014), e149–e149.

[55] T. Popmintchev et al. “Bright coherent ultrahigh harmonics in the keV X-ray regime from mid-infrared femtosecond lasers”. In: *science* 336.6086 (2012), pp. 1287–1291.

[56] X. M. Zhao et al. “Femtosecond ultraviolet laser pulse induced lightning discharges in gases”. In: *IEEE Journal of Quantum Electronics* 31.3 (1995), pp. 599–612.

[57] Y. Bellouard et al. “Fabrication of high-aspect ratio, micro-fluidic channels and tunnels using femtosecond laser pulses and chemical etching”. In: *Optics express* 12.10 (2004), pp. 2120–2129.

[58] K. Sugioka and Y. Cheng. “Femtosecond laser three-dimensional micro- and nanofabrication”. In: *Applied physics reviews* 1.4 (2014), p. 041303.

[59] T. Laarmann et al. “Femtosecond pulse shaping as analytic tool in mass spectrometry of complex polyatomic systems”. In: *Journal of Physics B: Atomic, Molecular and Optical Physics* 41.7 (2008), p. 074005.

[60] P. Maine et al. “Generation of ultrahigh peak power pulses by chirped pulse amplification”. In: *IEEE Journal of Quantum electronics* 24.2 (1988), pp. 398–403.

[61] T. Eidam et al. “Femtosecond fiber CPA system emitting 830 W average output power”. In: *Optics letters* 35.2 (2010), pp. 94–96.

[62] V. Ayvazyan et al. “Generation of GW radiation pulses from a VUV free-electron laser operating in the femtosecond regime”. In: *Physical review letters* 88.10 (2002), p. 104802.

[63] I. S. Ko et al. “Construction and commissioning of PAL-XFEL facility”. In: *Applied Sciences* 7.5 (2017), p. 479.

[64] M. Thumm. “State-of-the-art of high-power gyro-devices and free electron masers”. In: *Journal of Infrared, Millimeter, and Terahertz Waves* 41.1 (2020), pp. 1–140.

[65] E. Allaria et al. “Highly coherent and stable pulses from the FERMI seeded free-electron laser in the extreme ultraviolet”. In: *Nature Photonics* 6.10 (2012), pp. 699–704.

[66] G. Geloni, V. Kocharyan, and E. Saldin. “A novel self-seeding scheme for hard X-ray FELs”. In: *Journal of Modern Optics* 58.16 (2011), pp. 1391–1403.

[67] G. Geloni. “Self-seeded free-electron lasers”. In: *Synchrotron Light Sources and Free-Electron Lasers: Accelerator Physics, Instrumentation and Science Applications* (2020), pp. 191–223.

[68] J. Feldhaus et al. “Possible application of X-ray optical elements for reducing the spectral bandwidth of an X-ray SASE FEL”. In: *Optics Communications* 140.4-6 (1997), pp. 341–352.

[69] E. Saldin, E. V. Schneidmiller, and M. V. Yurkov. *The physics of free electron lasers*. Springer Science & Business Media, 1999.

[70] M.l Gross and S. Haroche. "Superradiance: An essay on the theory of collective spontaneous emission". In: *Physics reports* 93.5 (1982), pp. 301–396.

[71] E. L. Saldin, E. A. Schneidmiller, and M. V. Yurkov. "Statistical and coherence properties of radiation from X-ray free-electron lasers". In: *New Journal of Physics* 12.3 (2010), p. 035010.

[72] D. Gauthier et al. "Spectrotemporal shaping of seeded free-electron laser pulses". In: *Physical review letters* 115.11 (2015), p. 114801.

[73] D. Gauthier et al. "Generation of phase-locked pulses from a seeded free-electron laser". In: *Physical review letters* 116.2 (2016), p. 024801.

[74] G. De Ninno et al. "Single-shot spectro-temporal characterization of XUV pulses from a seeded free-electron laser". In: *Nature communications* 6.1 (2015), pp. 1–5.

[75] K. C. Prince et al. "Coherent control with a short-wavelength free-electron laser". In: *Nature Photonics* 10.3 (2016), pp. 176–179.

[76] A. Wituschek et al. "Tracking attosecond electronic coherences using phase-manipulated extreme ultraviolet pulses". In: *Nature communications* 11.1 (2020), pp. 1–7.

[77] O. Y. Gorobtsov et al. "Seeded X-ray free-electron laser generating radiation with laser statistical properties". In: *Nature communications* 9.1 (2018), pp. 1–6.

[78] S. Reiche et al. "Overview of seeding methods for FELs". In: *Proc. IPAC* (2013), pp. 2063–2067.

[79] D. Xiang et al. "Demonstration of the echo-enabled harmonic generation technique for short-wavelength seeded free electron lasers". In: *Physical review letters* 105.11 (2010), p. 114801.

[80] C. Lechner et al. "Status of the sFLASH Experiment". In: *Proc. 9th Int. Particle Accelerator Conf.(IPAC'18)*. 2018, pp. 1471–1473.

[81] P. Rebernik Ribič et al. "Echo-enabled harmonic generation studies for the FERMI free-electron laser". In: *Photonics*. Vol. 4. 1. Multidisciplinary Digital Publishing Institute. 2017, p. 19.

[82] P. A. Franken et al. "Generation of optical harmonics". In: *Physical Review Letters* 7.4 (1961), p. 118.

[83] P. B. Corkum. "Plasma perspective on strong field multiphoton ionization". In: *Physical review letters* 71.13 (1993), p. 1994.

[84] M. Lewenstein et al. "Theory of high-harmonic generation by low-frequency laser fields". In: *Physical Review A* 49.3 (1994), p. 2117.

[85] R. E. F. Silva et al. "Even harmonic generation in isotropic media of dissociating homonuclear molecules". In: *Scientific reports* 6.1 (2016), pp. 1–9.

[86] M. R. Shcherbakov et al. "Photon acceleration and tunable broadband harmonics generation in nonlinear time-dependent metasurfaces". In: *Nature communications* 10.1 (2019), pp. 1–9.

[87] J. Connerade. *Highly excited atoms*. 9. Cambridge University Press, 1998.

[88] P. Agostini and L. F. DiMauro. "The physics of attosecond light pulses". In: *Reports on progress in physics* 67.6 (2004), p. 813.

[89] J. Li et al. "Attosecond science based on high harmonic generation from gases and solids". In: *Nature Communications* 11.1 (2020), pp. 1–13.

[90] C. M. Heyl et al. "Introduction to macroscopic power scaling principles for high-order harmonic generation". In: *Journal of Physics B: Atomic, Molecular and Optical Physics* 50.1 (2016), p. 013001.

[91] R. Baumgartner and R. Byer. "Optical parametric amplification". In: *IEEE Journal of Quantum Electronics* 15.6 (1979), pp. 432–444.

[92] M. Bass et al. "Optical rectification". In: *Physical Review Letters* 9.11 (1962), p. 446.

[93] A. Nahata, A. S. Weling, and T. F. Heinz. "A wideband coherent terahertz spectroscopy system using optical rectification and electro-optic sampling". In: *Applied physics letters* 69.16 (1996), pp. 2321–2323.

[94] A. Monmayrant, S. Weber, and B. Chatel. "A newcomer's guide to ultrashort pulse shaping and characterization". In: *Journal of Physics B: Atomic, Molecular and Optical Physics* 43.10 (2010), p. 103001.

[95] V. R. Supradeepa et al. "New aspects of temporal dispersion in high-resolution Fourier pulse shaping: a quantitative description with virtually imaged phased array pulse shapers". In: *JOSA B* 27.9 (2010), pp. 1833–1844.

[96] D. J. Kane and R. Trebino. "Characterization of arbitrary femtosecond pulses using frequency-resolved optical gating". In: *IEEE Journal of Quantum Electronics* 29.2 (1993), pp. 571–579.

[97] R. Trebino. *Frequency-resolved optical gating: the measurement of ultrashort laser pulses*. Springer Science & Business Media, 2012.

[98] R. Trebino et al. “Measuring ultrashort laser pulses in the time-frequency domain using frequency-resolved optical gating”. In: *Review of Scientific Instruments* 68.9 (1997), pp. 3277–3295.

[99] M. K. Ernst L. Planck. “Zur Theorie des Gesetzes der Energieverteilung im Normalspectrum”. In: *Verhandl. Dtsc. Phys. Ges.* 2 (1900), p. 237.

[100] A. Einstein. “Zur Elektrodynamik bewegter Körper”. In: *Annalen der Physik* 4 (1905).

[101] R. A. Millikan. “A direct determination of ‘h’”. In: *Physical Review* 4.1 (1914), p. 73.

[102] D. J. Bradley, B. Liddy, and W. E. Sleat. “Direct linear measurement of ultrashort light pulses with a picosecond streak camera”. In: *Optics Communications* 2.8 (1971), pp. 391–395.

[103] E. M. Purcell and C. R. Pennypacker. “Scattering and absorption of light by nonspherical dielectric grains”. In: *The Astrophysical Journal* 186 (1973), pp. 705–714.

[104] S. Usenko et al. “Auger electron wave packet interferometry on extreme timescales with coherent soft X-rays”. In: *Journal of Physics B: Atomic, Molecular and Optical Physics* 53.24 (2020), p. 244008.

[105] S. Usenko et al. “Split-and-delay unit for FEL interferometry in the XUV spectral range”. In: *Applied Sciences* 7.6 (2017), p. 544.

[106] T. Plath. “Measurements and Detailed Analysis of Seeded High-Gain Free-Electron Lasers at FLASH”. PhD thesis. Staats-und Universitätsbibliothek Hamburg Carl von Ossietzky, 2017.

[107] S. Roling et al. “Temporal and spatial coherence properties of free-electron-laser pulses in the extreme ultraviolet regime”. In: *Physical Review Special Topics-Accelerators and Beams* 14.8 (2011), p. 080701.

[108] S. Schulz, V. Arsov, A. Winter, et al. “An optical cross-correlation scheme to synchronize distributed laser systems at FLASH”. In: *EPAC08, Genoa, Italy* (2008).

[109] R. Trebino et al. “Measuring ultrashort laser pulses just got a lot easier”. In: *Optics and Photonics News* 12.6 (2001), pp. 22–25.

[110] C. Iaconis and I. A. Walmsley. “Spectral phase interferometry for direct electric-field reconstruction of ultrashort optical pulses”. In: *Optics letters* 23.10 (1998), pp. 792–794.

[111] J. N. Sweetser, D. N. Fittinghoff, and R. Trebino. “Transient-grating frequency-resolved optical gating”. In: *Optics letters* 22.8 (1997), pp. 519–521.

[112] A. Azima et al. "Direct measurement of the pulse duration and frequency chirp of seeded XUV free electron laser pulses". In: *New Journal of Physics* 20.1 (2018), p. 013010.

[113] A. Kothe et al. "Time-of-flight electron spectrometer for a broad range of kinetic energies". In: *Review of Scientific Instruments* 84.2 (2013), p. 023106.

[114] P. Kruit and F. H. Read. "Magnetic field paralleliser for 2π electron-spectrometer and electron-image magnifier". In: *Journal of Physics E: Scientific Instruments* 16.4 (1983), p. 313.

[115] I. Grguraš. "Time resolved photoelectron spectroscopy for femtosecond characterization of X-ray free-electron laser pulses". PhD thesis. Universität Hamburg Hamburg, 2016.

[116] M. Ranke. "Investigation of low-energy photoelectron dynamics accelerated in terahertz light fields using a novel Velocity-Map-Imaging spectrometer". PhD thesis. Staats-und Universitätsbibliothek Hamburg Carl von Ossietzky, 2019.

[117] A. Wituschek et al. "High-gain harmonic generation with temporally overlapping seed pulses and application to ultrafast spectroscopy". In: *Optics Express* 28.20 (2020), pp. 29976–29990.

[118] A. Azima. "An electro-optical timing diagnostic for pump-probe experiments at the Free-Electron Laser in Hamburg FLASH". PhD thesis. DESY, 2009.

[119] S. Akturk et al. "Pulse-front tilt caused by spatial and temporal chirp". In: *Optics express* 12.19 (2004), pp. 4399–4410.

[120] M. Wollenhaupt et al. "Femtosecond strong-field quantum control with sinusoidally phase-modulated pulses". In: *Physical Review A* 73.6 (2006), p. 063409.

[121] K. W. DeLong and R. Trebino. "Improved ultrashort pulse-retrieval algorithm for frequency-resolved optical gating". In: *JOSA A* 11.9 (1994), pp. 2429–2437.

[122] K. W. DeLong et al. "Pulse retrieval in frequency-resolved optical gating based on the method of generalized projections". In: *Optics letters* 19.24 (1994), pp. 2152–2154.

[123] M. Hüning et al. "Observation of femtosecond bunch length using a transverse deflecting structure". In: *Proceedings of the FEL*. 2005.

[124] S. Ackermann et al. "Novel method for the generation of stable radiation from free-electron lasers at high repetition rates". In: *Physical Review Accelerators and Beams* 23.7 (2020), p. 071302.

[125] K. Hacker et al. “First Lasing of an HGHG Seeded FEL at FLASH”. In: *Proc. Intern. FEL 2015 Conf.* 2015, pp. 646–649.